A STUDY OF MAGNETO-OPTICAL AND MAGNETIC PROPERTIES OF BAND-ENGINEERED 2D DIRAC SEMIMETALS

A Dissertation

presented to

the Faculty of the Graduate School

at the University of Missouri-Columbia

In Partial Fulfillment

of the Requirements for the Degree

Doctorate of Philosophy

---

by

AMARNATH CHAKRABORTY

Prof. Giovanni Vignale, Dissertation Supervisor

DECEMBER 2025

The undersigned, appointed by the dean of the Graduate School, have examined the dissertation entitled

MAGNETO-OPTICAL AND MAGNETIC PROPERTIES OF BAND-ENGINEERED 2D DIRAC SEMIMETALS

presented by Amarnath Chakraborty,

a candidate for the degree of PhD in Physics,

and hereby certify that, in their opinion, it is worthy of acceptance.

Professor Giovanni Vignale

Professor Guang Bian

Professor Carsten Ullrich

Professor Yangchuan Xing

DEDICATION

This thesis is dedicated to my parents.

I am deeply grateful to my parents, Debnath and Mosumi Chakraborty, for their unwavering support and the value they placed on my education. Their dedication made it possible for me to pursue my aspirations, and for that, I will always be indebted. I am also profoundly thankful to my elder sister, Rwitu, and my brother-in-law, Saptarshi, whose guidance and encouragement made my journey to pursue doctorate seamless and reassuring. Their unwavering support made it possible for me to follow my aspirations.

My heartfelt appreciation goes to my fiancée, Angira, whose constant support, encouragement, and insight have been a source of strength every step of the way.

To my friends, each of you has been special in your own way, and I will always cherish the role you have played in my life.

I am also thankful to my colleagues in the department for their camaraderie, patience, and support throughout coursework and qualifiers. Their encouragement made this journey far smoother and more enjoyable.

To all who have supported and inspired me—thank you.

ACKNOWLEDGEMENTS

First and foremost, I would like to express my deepest gratitude to my advisor, Prof. Giovanni Vignale, whose guidance, patience, and invaluable insights made this work possible. His dedication and countless hours of discussions—both on the intricate details and the fundamental concepts—have been instrumental in shaping my research and academic growth.

I am also sincerely grateful to my co-supervisor, Dr. Guang Bian, for being an exceptional mentor and collaborator. His encouragement and guidance have been invaluable, and I truly appreciate his role in my academic and professional development.

Additionally I thank Prof. Carsten Ullrich, Prof. Yangchuan Xing for being members of my doctoral committee.

A special thanks to Dr. Suchi Guha, whose help as the Director of Graduate Studies was instrumental during my transition to NUS. Her assistance made it possible for me to have the incredible opportunity to work there, and for that, I am deeply appreciative.

Special thanks to Dr. Aleksandr Rodin for his insightful discussions and invaluable help, particularly with the figures in Chapter 5. His contributions and feedback greatly enriched this work.

CONTENTS

LIST OF FIGURES

NOMENCLATURE

Abbreviations

DFT	Density functional theory.
H.C.	Hermitian conjugate.
NSDS	Nonsymmorphic Dirac Semimetals.
KK	Kramers–Kronig.
MF	Mean field.
NN	Nearest neighbor(s).
MBz	Moire Brillouin Zone.
TW	Trigonal warping.
IM	Insulator–Metal.
LT	Lifshitz transition.
SOC	Spin–orbit coupling.
TBG	Twisted bilayer Graphene
TDBG	Twisted Double bilayer Graphene
VQE	Variational Quantum Eigensolver
SQD	Sample Based Quantum Diagonalization.

Physical constants

$\hbar$	Reduced Planck constant, $\hbar = 1.055 \times 10^{-34}\,\mathrm{m^2 kg\,s^{-1}}$ (SI) = $6.582 \times 10^{-16}\,\mathrm{eV\,s}$.
σ_0	Graphene universal conductivity, $\sigma_0 = e^2/(4\hbar)$.
ε_0	Vacuum permittivity, $\varepsilon_0 = 8.854 \times 10^{-12}\,\mathrm{F\,m^{-1}}$ (SI) = $1.419 \times 10^{-30}\,\mathrm{C^2\,eV^{-1}\,m^{-1}}$.
μ_0	Vacuum permeability, $\mu_0 = 4\pi \times 10^{-7}\,\mathrm{N\,A^{-2}}$ (SI).
c	Speed of light, $c = 2.998 \times 10^{8}\,\mathrm{m\,s^{-1}}$ (SI).
e	Elementary charge, $e = 1.602 \times 10^{-19}\,\mathrm{C}$ (SI).
k_B	Boltzmann constant, $k_B = 1.381 \times 10^{-23}\,\mathrm{m^2\,kg\,s^{-2}\,K^{-1}}$ (SI) = $8.617 \times 10^{-5}\,\mathrm{eV\,K^{-1}}$.
m_e	Electron rest mass, $m_e = 9.109 \times 10^{-31}\,\mathrm{kg}$.
Φ_0	Magnetic flux quantum, $\Phi_0 = h/(2e) = 2.068 \times 10^{-15}\,\mathrm{Wb}$.
α_F	Fine structure constant, $\alpha = \frac{e^2}{4\pi\varepsilon_0\hbar c} \approx 1/137.036$.

Mathematical operators

$[A, B]$	Commutator.
$\{A, B\}$	Anticommutator.
$\delta(x - a)$	Dirac delta function.
$\delta_{i,j}$	Kronecker delta.
T	Time-ordering operator.
$\Theta(x)$	Heaviside step function.
*	Complex conjugate.
$\dagger$	Hermitian conjugate (conjugate transpose).
∇	Gradient.
$\nabla\cdot$	Divergence.
$\nabla\times$	Curl.
∂_x	Partial derivative with respect to x.
$\frac{d}{dx}$	Ordinary derivative with respect to x.
Re	Real part.
Im	Imaginary part.
$\langle A \rangle$	Expectation value of A.
$\langle i \vert j \rangle$	Inner product (bra–ket notation).
$\vert i \rangle \langle j \vert$	Outer product.
$\otimes$	Tensor (Kronecker) product.
Tr	Trace.
det	Determinant.
$\equiv$	Defined as / Identically equal to.
$\approx$	Approximately equal to.
$\propto$	Proportional to.
$\mathcal{F}$	Fourier transform.
$\sum$	Summation symbol.
$\prod$	Product symbol.
$\oint$	Closed contour integral.
$\int$	Integral symbol.
$\mathcal{P}$	Cauchy principal value.

Relevant variables

E_F	Fermi level.
ω	Angular frequency.
σ_{ij}^{D}	Drude conductivity tensor.
σ_{ij}^{reg}	Regular part of the conductivity tensor.
σ_{ij}	Total conductivity tensor.
θ	Twist angle.
ε_r	Relative permittivity.
D_{ij}	Drude weight tensor.
f	Frequency.
n	Carrier density (positive for electrons, negative for holes).
T	Absolute temperature.
v_F	Fermi velocity.
V	Displacement field (interlayer potential difference).
ϕ	In-plane magnetic flux (Peierls phase).
B	Magnetic field.
Δ	Band gap.
a	Lattice constant.
γ_i	Interlayer hopping parameters.

MAGNETO-OPTICAL AND MAGNETIC PROPERTIES OF BAND-ENGINEERED 2D DIRAC SEMIMETALS

Amarnath Chakraborty

Prof. Giovanni Vignale, Thesis Supervisor

ABSTRACT

This thesis investigates the electronic and magnetic properties of *low-dimensional quantum materials* using analytical modeling, continuum theories, and numerical simulations. The study focuses on *nonsymmorphic Dirac semimetals*, *Bernal bilayer graphene*, and *twisted bilayer graphene*, exploring how lattice symmetry and external perturbations, such as magnetic fields, influence the band structure and stabilize novel quantum phases, including gapped, semi-metallic, and topological states.

The work begins by developing a framework to describe the *magneto-optical properties* of nonsymmorphic semimetals, including optical absorbance and polarization rotations (Faraday and Kerr) under magnetic fields or intrinsic magnetization coupling with the out-of-plane spin. The focus then shifts to Bernal-stacked bilayer graphene, where we analyze the *insulator–metal phase transition* driven by an in-plane magnetic field and an out-of-plane displacement field. This transition occurs at high magnetic fields, leading us to propose the role of trigonal warping in reducing the critical field to experimentally accessible values. Also, we explore an investigation of twisted systems, where the reduced size of the *Moiré Brillouin zone* further enhances tunability. While the insulator–metal transition is not observed in twisted bilayer graphene, twisted multilayer graphene could provide an excellent platform to visualize similar effects, potentially revealing unique signatures in its *magnetic response*.

Keywords: *Low-dimensional quantum materials, Nonsymmorphic Dirac semimetals, Bernal bilayer graphene, Twisted bilayer graphene, Magneto-optical properties, Insulator–metal transition, Magnetic response, Trigonal warping, Moiré Brillouin zone.*

Chapter 1

INTRODUCTION

1.1 Rise of Graphene and other 2D materials

Graphene, a single layer of carbon atoms arranged in a honeycomb lattice, was first isolated from bulk graphite in 2004 by Geim and Novoselov ([1]). This landmark discovery demonstrated that truly two-dimensional crystals can be stable under ambient conditions and sparked enormous interest in atomically thin materials.

Its remarkable features include:

- **Gapless spectrum**: conduction and valence bands meet at Dirac points, enabling extreme electrical tunability and ultrafast switching ([1]).
- **Dirac quasiparticles**: low-energy carriers obey a massless Dirac equation, allowing tabletop studies of relativistic quantum phenomena such as Klein tunneling ([2]).
- **Exceptional mobility**: even at room temperature on rough substrates, carrier mobilities exceed $10^4\,\mathrm{cm}^2/\mathrm{V{\cdot}s}$, thanks to suppressed backscattering.
- **Mechanical robustness**: with a breaking strength $\sim$40 N/m—over 100$\times$ stronger than steel—a 1 m^2 graphene hammock can support a 4 kg cat while weighing only 0.77mg.
- **Chemical versatility**: controlled defect creation and functionalization (e.g. ion-beam drilling and selective etching) yield molecular-scale pores and new filtering applications.

Today most graphene work remains at the R&D level, yet early commercial uses have emerged in electronics, energy storage, and composites. The global graphene market, valued at \$20 M in 2014, is projected to exceed \$200 M by 2026 (Graphene Market Report 2015).

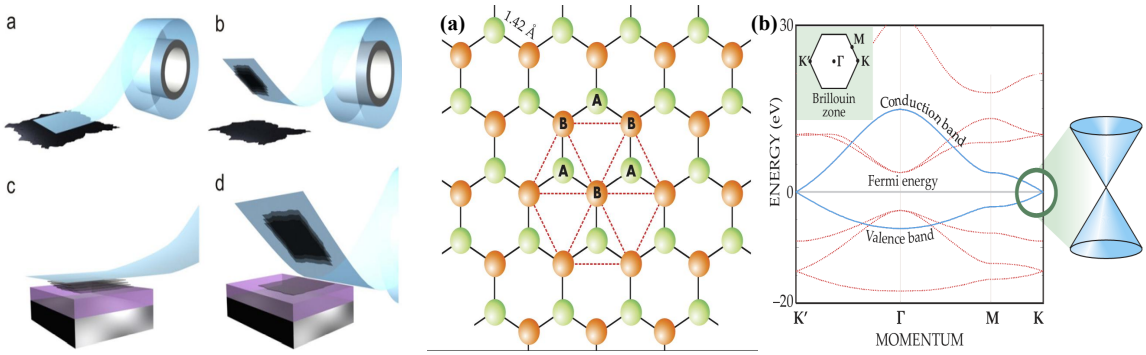

Figure 1.1: *(A) Mechanical exfoliation of 2D crystals: (a) adhesive tape is pressed against the thin debris of a 3D layered structure crystal, so that the top few layers stay attached to the tape (b); (c) after repeatedly peeling the tape against itself, the part of the tape with the thinnest crystals of layered material is pressed against a surface of choice; (d) upon peeling off, the bottom layer is left on the substrate, ready for microscope inspections. Source: Ref. [3]. (B) The honeycomb lattice of graphene and the Bloch band description of graphene's electronic structure. (a) This figure consists of two interpenetrating triangular sublattices: The sites of one sublattice (green) are at the centers of triangles defined by the other (orange). The lattice thus has two carbon atoms, designated A and B, per unit cell, and is invariant under 120° rotations around any lattice site. (b) The orbital energies depend on the momentum of charge carriers in the crystal Brillouin zone (inset, right). The π and $\pi*$ bands (blue in the electronic structure plot) are decoupled from the σ and $\sigma*$ bands (red) because of inversion symmetry and are closer to the Fermi energy because they participate less in bonding. The Fermi energy separates occupied and empty states. In a neutral graphene sheet, this is the energy where valence and conduction bands meet (zero energy above, often referred to as the neutrality point). The bands form conical valleys that touch at two of the high-symmetry points, conventionally labeled K and K' , in the Brillouin zone.Source: Ref. [4]*

1.1.1 Beyond Graphene: Gaps and Spin–Orbit Limitations

Despite its many advantages, graphene faces two key challenges for electronics and spintronics. First, as a gapless semimetal its conduction and valence bands meet at the Dirac points, making it impossible to switch off current completely in field-effect transistors. Second, graphene's intrinsic spin–orbit coupling is extremely weak ($\approx 10\mu$eV), precluding robust topological phases such as the quantum spin Hall effect ([6]).

To overcome these limitations, researchers have turned to heavier group-IV analogues and novel crystal symmetries. Silicene and germanene, for example, develop a finite bandgap through lattice buckling and enhanced spin–orbit interactions, albeit requiring carefully chosen substrates for stability. More generally, a simple co-dimension argument shows that any perturbation of the form $m\sigma_z$ will gap a 2D Dirac Hamiltonian $H = \alpha k_x \sigma_x + \beta k_y \sigma_y$, so that truly gapless Dirac cones demand extra symmetry constraints. In particular, nonsymmorphic space-group symmetries can enforce gapless crossings at high-symmetry points of the Brillouin zone, as demonstrated by several theoretical works (e.g., [7, 8, 9]).

A striking realization of these ideas is bismuthene on SiC, which exhibits a large quantum spin Hall gap of ≈ 0.8 eV ([10]). Even more recently, α-bismuthene—a nonsymmorphic monolayer—was

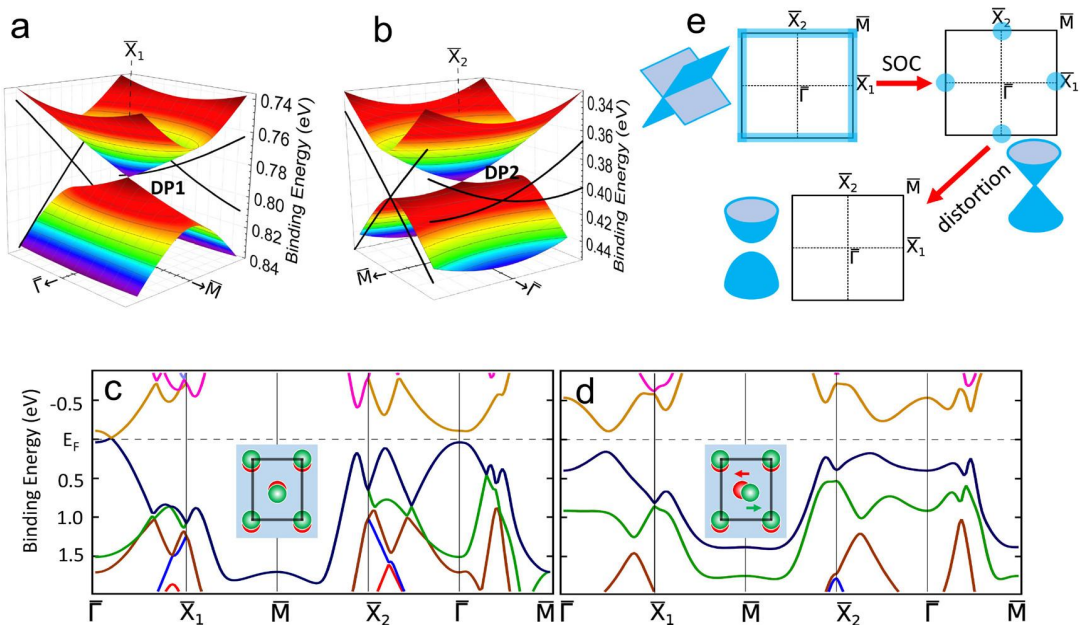

Figure 1.2: *From the paper by Kowalczyk et all [5] SOC and distortion effects on α-Bi band structure. (a,b) DFT band surface calculated in the vicinity of $\bar{X}_1$ and $\bar{X}_2$, respectively. (c) Band structure of α-Bi in the absence of spin–orbit coupling. (d) Band structure of distorted α-Bi. The distortion is shown in the inset. The two atoms are moved along arrow directions by 2% of the unit cell width. (e) Evolution of band configuration from without SOC to with SOC to with both SOC and symmetry-breaking distortion. The Dirac/nodal points are highlighted in blue in the Brillouin zone. Source: Ref([5]).*

shown to host symmetry-protected Dirac fermions despite strong spin–orbit coupling ([5]). These examples illustrate how heavy elements and lattice symmetries can both open substantial gaps and stabilize topological phases, bridging the gap between graphene's idealized physics and practical device requirements.

1.1.2 Van der Waals Heterostructures: A New Frontier

Building on the success of monolayer graphene, researchers now assemble "atomic Lego" by stacking different two-dimensional crystals into van der Waals (vdW) heterostructures. Each sheet retains its strong in-plane covalent bonding, while weak interlayer forces hold the stack together. By combining graphene with materials such as hBN, MoS_2 or WS_2, one can tailor band offsets, proximity effects and device functionality (e.g. "Designer van der Waals heterostructures," A. K. Geim et al.).

A natural first step is Bernal-stacked bilayer graphene (Fig. (1.4)). In this simplest vdW stack, applying an electric field perpendicular to the layers breaks inversion symmetry and opens a tunable bandgap (Controlling the electronic structure of bilayer graphene). This gate-induced gap transforms graphene from a semimetal into a switchable semiconductor, enabling transistor action while preserving

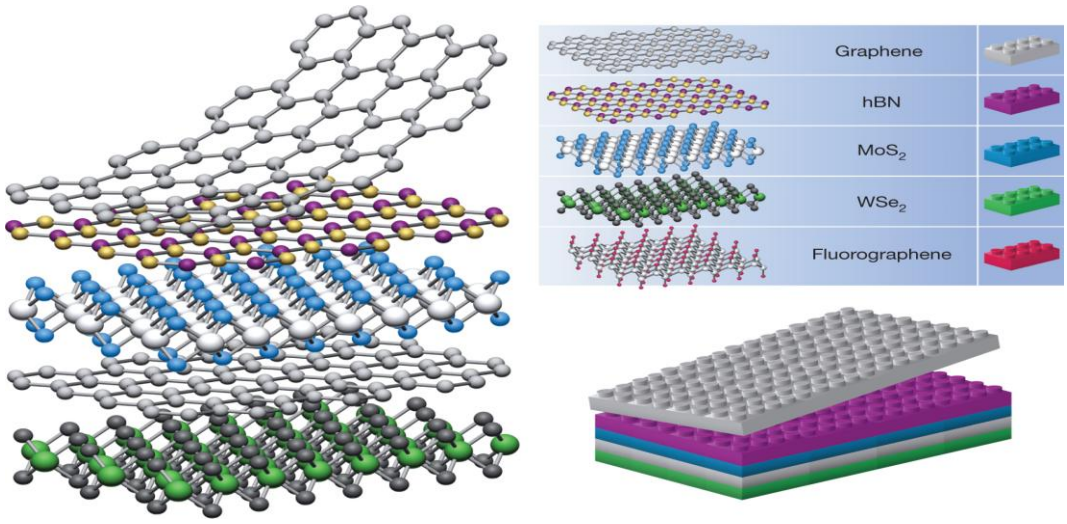

Figure 1.3: *Illustration of a vdW heterostructure. Source: Ref.[11].*

high mobility.

When two graphene sheets are overlaid with a small relative rotation, a long-wavelength interference pattern—known as a moiré superlattice (mSL)—emerges. The twist angle θ between layers determines the mSL periodicity, which can be directly imaged (see Fig. 1.5). Strictly periodic supercells occur only at commensurate angles, satisfying

$$\cos\theta \;=\; \frac{3m^2+3mr+\frac{1}{2}r^2}{3m^2+3mr+r^2}\,, \qquad 0^\circ < \theta < 30^\circ, \tag{1.1}$$

where m and r are coprime integers [13]. However, continuum theories bypass this restriction by focusing on the low-energy Dirac states in each layer and treating interlayer tunneling perturbatively.

The pioneering continuum model by Lopes dos Santos et al. [13] and its extension by Bistritzer and MacDonald [14] capture the essential physics at arbitrary θ. In these approaches, one writes an effective Hamiltonian

$$H_{\mathrm{TBG}} = \begin{pmatrix} H_1(-\frac{\theta}{2}) & T(\mathbf{r}) \\ T^\dagger(\mathbf{r}) & H_2(+\frac{\theta}{2}) \end{pmatrix},$$

where $H_i(\pm\theta/2)$ describes a Dirac cone rotated by $\pm\theta/2$, and $T(\mathbf{r})$ encodes the spatially periodic interlayer coupling.

Remarkably, at certain "magic" angles near $\theta \approx 1.1^\circ$, the lowest moiré minibands become

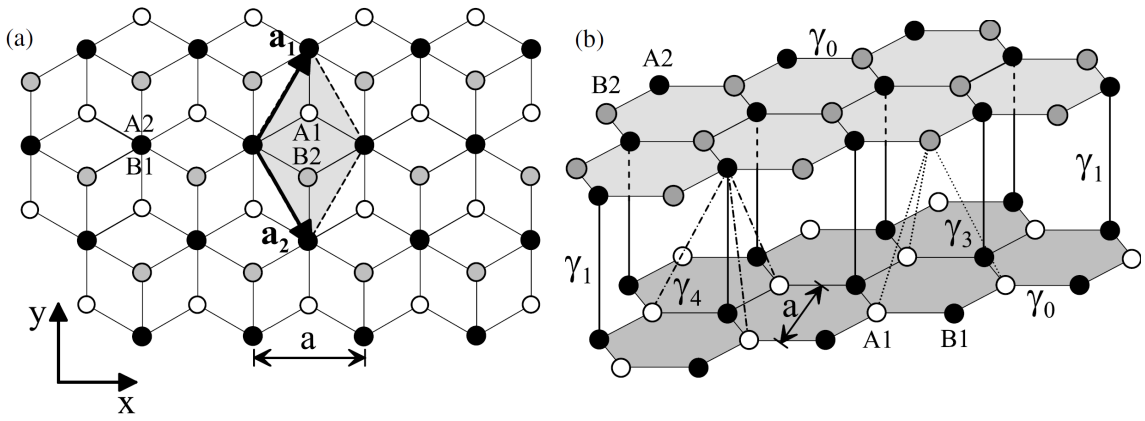

Figure 1.4: *(a) Plan and (b) side view of the crystal structure of bilayer graphene. Atoms A1 and B1 on the lower layer are shown as white and black circles, A2, B2 on the upper layer are black and grey, respectively. The shaded rhombus in (a) indicates the conventional unit cell. Source: Ref([12]).*

nearly flat, dramatically enhancing electron–electron interactions. Experiments on these magic-angle structures reveal correlated insulating phases and unconventional superconductivity ([15]), inaugurating the field of "twistronics." This demonstrates how simple geometric tuning—twist and interlayer coupling—can unlock rich many-body phenomena in van der Waals assemblies. Although practical challenges—substrate compatibility, interlayer contamination and reproducibility—currently limit most heterostructures to a few layers, advances in transfer techniques and interface cleaning are rapidly expanding the palette of realizable stacks. As control improves, vdW heterostructures and bilayer graphene systems promise on-demand engineering of bandgaps, topological phases and strongly correlated states, setting the stage for the theoretical studies in this thesis.

In summary, the isolation of graphene and its extraordinary Dirac physics laid the foundation for a diverse family of 2D materials. By exploring heavier elements, novel lattice symmetries, and twisted multilayers, researchers have engineered sizable bandgaps, strong spin–orbit effects, and flat, highly correlated bands. This rich landscape of graphene and graphene-like materials provides the backdrop for the band-engineering studies pursued in this thesis.

1.2 Motivation and Framework

The central goal of this work is to show how external perturbations—electric and magnetic fields—serve as powerful, reversible "knobs" to engineer and interrogate the electronic bands of two-dimensional crystals. Applying a perpendicular electric field (via a gate voltage) cleanly breaks inversion symmetry in bilayer or moiré superlattices, opening and tuning gaps while reshaping the Berry curvature landscape ("Controlling the electronic structure of bilayer graphene"). In twisted

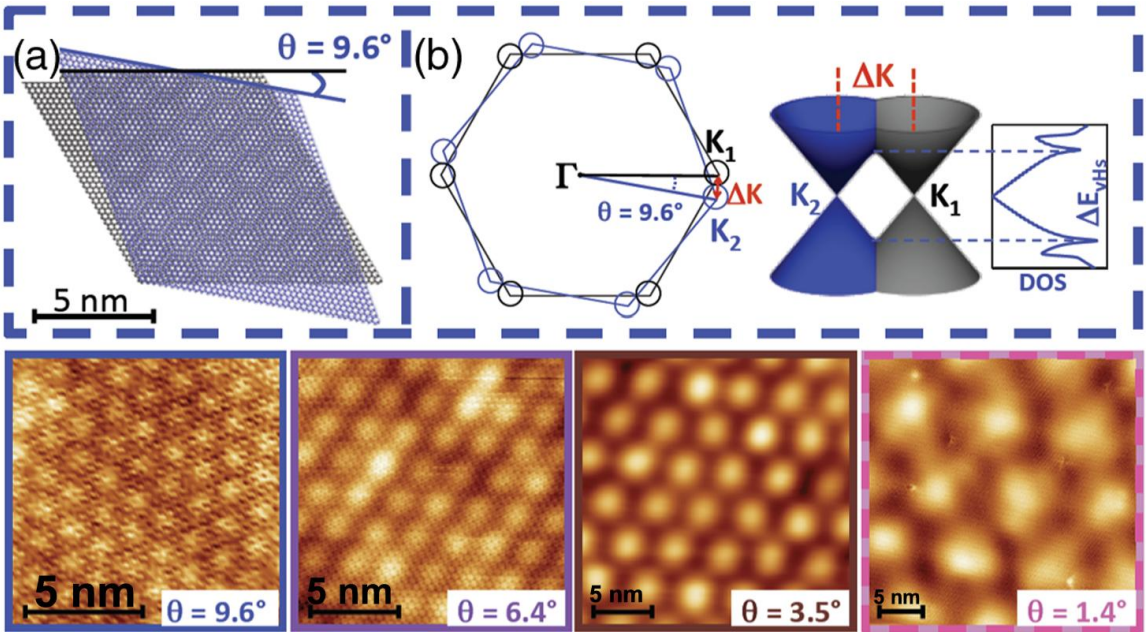

Figure 1.5: *(a) Illustration of a MP arising from a rotation angle $\theta = 9.6°$. (b) Emergence of vHs as a consequence of the rotation in reciprocal space. (c) STM images of several MP with different . The scale bar is* 5.0 *nm. Source: Ref([16]).*

bilayers and heterobilayers, the same field can transfer charge between layers or valleys, driving transitions between distinct electronic phases.

Magnetic fields, by contrast, quantize states into Landau levels, yielding quantum Hall plateaus and the fractal Hofstadter spectrum in moiré systems ("Hofstadter's butterfly and moiré superlattices"). They also break time-reversal symmetry, allowing Chern-insulator phases and giant magneto-optical effects that vanish at zero field. Together, these symmetry-breaking fields give continuous control over band topology, connectivity and degeneracies in 2D materials.

From a theoretical standpoint, these effects enter naturally into tight-binding and continuum models. Electric fields appear as layer-dependent potentials, while magnetic fields enter via Peierls phases or minimal coupling. Solving these models reveals emergent phenomena: flat minibands that amplify interactions in magic-angle twisted graphene ("Moiré bands in twisted double-layer graphene"), tunable infrared absorption edges in gated bilayers, and cyclotron-resonance peaks tied to Landau quantization.

Beyond graphene systems, nonsymmorphic 2D crystals such as α-bismuthene, MBi offer another ideal testbed. There, symmetry-protected Dirac crossings persist even under strong spin–orbit coupling ("Realization of symmetry-enforced two-dimensional Dirac fermions in nonsymmorphic α-bismuthene"), and external fields can selectively gap or tilt these crossings. Analyzing field effects

in such lattices extends the same band-engineering toolkit to new topological phases.

In all cases, theory complements experiment—angle-resolved photoemission, transport, Kerr/-Faraday rotation and optical spectroscopy—by explaining how and why gaps open, flat bands emerge, and optical/magnetic responses evolve. The framework developed here (tight-binding calculations, continuum approximations and linear-response theory) will validate and predict measurable properties across graphene, twisted bilayers and nonsymmorphic 2D materials, laying the groundwork for future functional devices and fundamental discoveries.

1.3 Objectives

The overarching objective of my research has been to develop a robust theoretical understanding of how symmetry, dimensionality, and external fields interplay to shape the electronic and optical responses of two-dimensional quantum materials. My journey began with a focus on nonsymmorphic Dirac semimetals—materials where glide planes and screw axes enforce band crossings that cannot be gapped without breaking symmetry. These systems exhibit unique symmetry-protected Dirac points, and I was drawn to the question: how do such protected states respond to external perturbations, especially electromagnetic fields?

1. Photon Absorption in Nonsymmorphic Dirac Semimetals. To address this, my first project centered on calculating the photon absorption spectrum of a nonsymmorphic 2D Dirac semimetal under external magnetic field. I explored how selection rules, enforced by nonsymmorphic symmetry, manifest in optical transitions between valence and conduction bands. This required extending analytical tools for light-matter interaction to models with exotic band dispersion such as Dirac cones. The results revealed not only anisotropic absorption features but also tunable absorption edges that depended on both field strength and symmetry orientation—highlighting how nonsymmorphic symmetry governs magneto-optical responses in ways distinct from conventional Dirac systems.

2. Faraday Rotation via Current–Current Response Theory. Building on the optical absorption work, I turned to optical rotations effects—specifically, the Faraday and Kerr rotation of linearly polarized light in a magnetic field. This required deriving the full current–current response function in the presence of both spin–orbit coupling and nonsymmorphic symmetry constraints. The resulting theoretical expressions predict logarithmic divergence in the Faraday angle at frequencies corresponding to absorption edge (band gap energy) transitions, offering a direct link between symmetry-enforced band crossings and observable optical rotation.

3. Magnetic Response of Bernal-Stacked Bilayer Graphene. I investigated the magnetic response of Bernal-stacked bilayer graphene subjected to an in-plane magnetic field and an out-of-plane displacement field. Using a four-band tight-binding model, I computed the insulator–metal phase transition spectrum and employed the Feynman–Hellmann formalism to evaluate the orbital magnetic susceptibility via second-order perturbation of the energy with respect to the magnetic field. To reduce the magnetic field required to induce the insulator–metal transition, I incorporated skew interlayer couplings that give rise to trigonal warping in the band structure. The inclusion of these couplings introduces new energy and length scales, significantly lowering the critical magnetic field to experimentally accessible values and thereby making the transition more feasible in practical settings.

4. Twisted Bilayer Graphene under Combined Fields. Finally, I extended the analysis to small-angle twisted bilayer graphene, incorporating both external electric and magnetic fields within the moiré superlattice framework. By projecting the system onto the low-dispersive miniband subspace and including Peierls phases along with interlayer potential differences, I demonstrated that the linear band dispersion evolves into a parabolic form. However, unlike the Bernal-stacked case, an insulator–metal transition cannot be realized as a function of field strength, indicating a distinct intrinsic nature of the parabolic bands. Nevertheless, the field-induced modifications in the band topology suggest promising avenues for exploring their influence on linear response properties—such as the Drude weight—and will pave the way for designing novel electronic phases in two-dimensional materials.

Together, these objectives chart a path from fundamental symmetry-driven phenomena in idealized Dirac semimetals to practical band-engineering applications in graphene-based heterostructures. Each step validates the theoretical framework against known experiments and suggests new measurements to probe the rich landscape of field-tunable 2D materials.

1.4 Thesis Outline

This dissertation begins with a broad overview of two-dimensional (2D) materials, starting from graphene and its derivatives, extending to nonsymmorphic 2D crystals, and emphasizing the motivation for employing external fields to engineer and probe their electronic band structures.

Chapter 2 introduces the unique characteristics of nonsymmorphic Dirac semimetals, outlining their theoretical framework, real-world realizations, and classification into distinct types.

In *Chapters 3 and 4*, we investigate the magneto-optical properties of nonsymmorphic Dirac semimetals in the presence of external magnetic fields. We derive the optical selection rules governing absorption, identify the role of lattice symmetries in protecting Dirac crossings, and develop a current–current response formalism for calculating photon absorption and Faraday rotation. Our results predict logarithmic enhancements in the optical rotation spectrum under applied magnetic fields.

Chapter 5 focuses on Bernal-stacked bilayer graphene, where we compute the band dispersion under crossed electric and magnetic fields and explore the field-driven metal–insulator (MI) transition. We further examine the orbital magnetic susceptibility, revealing how field-induced MI transitions manifest in measurable responses.

In *Chapter 6*, we extend the study to trigonal-warping–enabled Bernal-stacked bilayer graphene. We demonstrate that including trigonal warping substantially reduces the required field strength for the MI transition to occur.

Chapter 7 turns to small-angle twisted bilayer graphene (tBG). We describe the formation of its Moiré Brillouin zone, construct the continuum model, and analyze the renormalization of the Fermi velocity due to twisting. At the chiral limit, we successfully reproduce the celebrated flat bands at the magic angles. While initially motivated to explore the MI transition under combined electric and magnetic fields, our study reveals—based on the best of our knowledge—that the tBG system does not support this transition in a straightforward manner. We provide a justification for this finding.

Finally, *Chapter 8* summarizes the principal conclusions of this dissertation and highlights promising avenues for future research. Detailed derivations, supplementary calculations, and technical material are collected in the appendices.

Chapter 2

2D NONSYMMORPHIC DIRAC SEMIMETAL

Over the past decade, two-dimensional (2D) Dirac-like electron gases have attracted tremendous research interest, with examples ranging from graphene [2] to topological insulators [17] to Dirac and Weyl semimetals. These materials [18, 19, 20] possess several unique electronic and optical properties traceable to their linear energy dispersion and non-trivial Berry phase. Graphene has become the prototypical instance of two-dimensional Dirac fermions. However, the Dirac points in many existing 2D materials, including graphene, are vulnerable to spin-orbit coupling (SOC). Motivated by finding alternative 2D materials beyond graphene, various atomically thin materials, including silicene, germanene, few-layer black phosphorus, and other 2D compounds, have been theoretically proposed and experimentally prepared [21, 22, 23, 24]. Recently, symmetry-protected 2D Dirac semimetals have attracted intense interest. These materials feature Dirac points that are not gapped by SOC interaction and are protected by nonsymmorphic lattice symmetry [5, 25].

Dirac-like band dispersions have recently been observed in the nonsymmorphic monolayer film, α-bismuthene [5]. The lattice structure of α-bismuthene belongs to the #42 layer group (*pman*), as shown in Fig. 2(a). There are two atomic sublayers marked by 'A' and 'B' in α-bismuthene with a vertical spacing of 3.02 Å in between. The in-plane lattice constants are 4.53 and 4.72 Å in the x and y directions, respectively. The lattice is invariant under a glide mirror reflection. That is a mirror reflection to the middle plane between the two sublayers followed by a translation by a half lattice constant in both x and y directions. This nonsymmorphic glide mirror symmetry leads to band degeneracy at the high symmetry momentum points $\bar{X}_1$ and $\bar{X}_2$ of the Brillouin zone as described in Sec. (2.1) later. The first-principles band structure (Fig. 2(b)) indeed exhibits band crossing features among all the bands at $\bar{X}_1$ and $\bar{X}_2$. The top Dirac nodes in valence bands $\bar{X}_1$ and $\bar{X}_2$ are denoted by 'DP1' and 'DP2', respectively. The two Dirac nodes are not connected by any lattice symmetry operation. Therefore, they are at different energies: DP1 at 0.7 eV and DP2 and 0.4 eV. Though

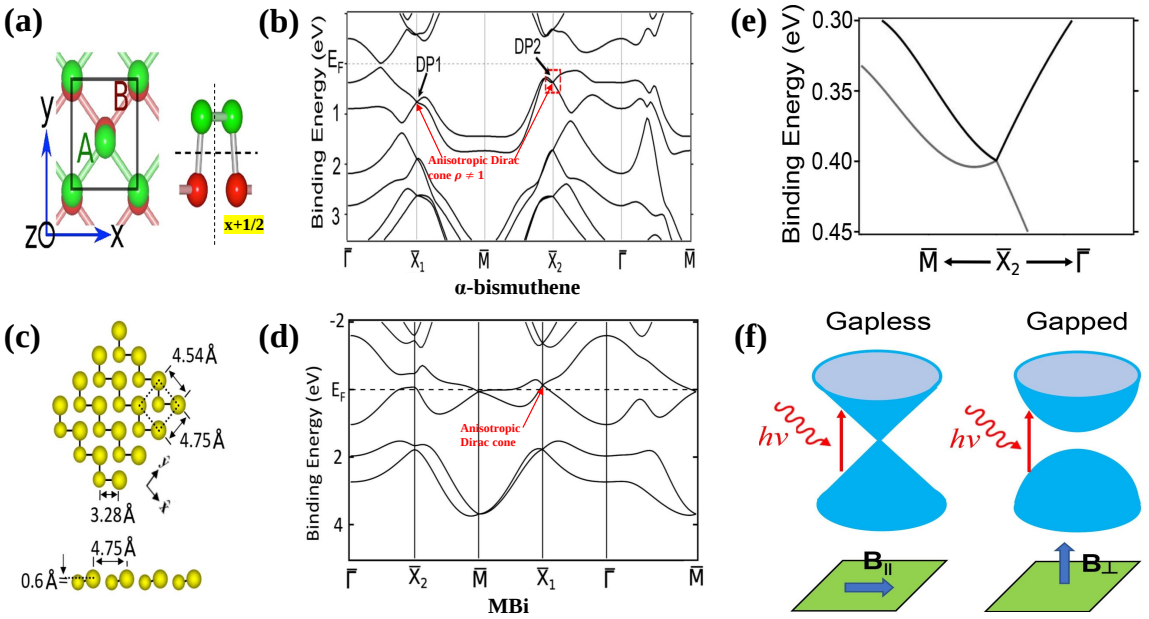

Figure 2.1: *(a) Lattice structure of α-bismuthene. (b) Band structure of α-bismuthene. This shows both DPs are below Fermi energy. The Fermi velocities are $v_x = 3.95 \times 10^5$ m/s and $v_y = 2.12 \times 10^5$ m/s at DP1, and $v_x = 1.19 \times 10^5$ m/s and $v_y = 4.67 \times 10^5$ m/s at DP2. (c) Lattice structure of Monolayer Bismuth. (d) Band structure of Monolayer Bismuth. This shows both DPs are below Fermi energy and are much closer than α-bismuthene. (e) Zoom-in band structure marked by the red box in (c), emphasizing the strong anisotropy present in DP2 ($\bar{X}_2$). (f) The band is gapped in case the direction of magnetic field is normal to the plane and gapless for parallel to the plane.*

the two nodes are not at the Fermi level in the pristine material, their energies can be shifted by applying a gating voltage and/or a strain. Another example of nonsymmorphic symmetry leading to protected Dirac points is found in Bi monolayer ([5]; see Fig. 2(c), with layer group LG-p21/m11 (screw axis), where the Dirac points are predicted to be much closer to the Fermi level(Fig. 2(d)).

To effectively optimize and utilize the unique properties of 2D materials, various strategies have been proposed to tune the optical and electronic properties, such as the introduction of electric fields, strain modulation [26, 27], atom doping [28], strain engineering [29], etc. However, to date, the optical properties of 2D nonsymmorphic Dirac materials have not been systematically investigated [30, 31].

There are two crucial differences between nonsymmorphic Dirac semimetals and graphene-like 2D Dirac materials. First, an anisotropy factor ρ is allowed by the lower symmetry of the system. Our calculations show that ρ plays a vital role in controlling photon absorption. Second, the spin (the σ matrices) and orbital (the τ matrices) degrees of freedom are coupled together in our model Hamiltonian. Therefore, nonsymmorphic Dirac semimetals support strong spin-orbit coupling, unlike graphene, in which the spin and orbital parts are largely decoupled. These two facts yield a richer

spectrum of optical properties in nonsymmorphic Dirac semimetals than in graphene.

One probe of the states of the 2D materials is through their interaction with the external electromagnetic field. In this report, we investigate the new features that nonsymmorphic symmetry brings to the magneto-optical properties of two-dimensional Dirac semimetal. We first show our study on the optical absorption spectra of the material with and without the presence of the magnetic field. Secondly, we showed that due to the nonsymmorphic symmetry present in our material, a circularly polarized electromagnetic wave falling and passing through such a material can experience different responses depending on the sign of the polarization, the so-called Faraday and Kerr rotation.

Firstly, we calculate the absorption coefficient. Our calculations show that it depends strongly on the anisotropy factor and the photon polarization. By rotating the latter, one can change the absorption coefficient by more than an order of magnitude, giving rise to *birefringence*. When a magnetic field is applied, the absorption coefficient also depends on an internal parameter, which we term the "mixing angle" of the band structure. This parameter becomes therefore accessible to experimental investigation. We further find that an in-plane magnetic field, while leaving the system gapless, can induce a Van-Hove singularity in the joint density of states: this causes a significant enhancement of the optical absorption at the frequency of the singularity for one direction of polarization but not for the orthogonal one, making the optical properties even more strongly dependent on polarization and anisotropy. These results suggest that a very pure nonsymmorphic 2D Dirac semimetal can be an excellent candidate material for tunable magneto-optic devices.

Secondly, we also present our frequency-dependent calculations for the magneto-optical properties like the optical Hall conductivity and Faraday and Kerr rotation angle. The results based on our theoretical calculations for optical conductivities reveal that the longitudinal conductivities depend on the anisotropy, which gives rise to the birefringence. However, the transverse component (the Hall conductivity) is only frequency-dependent and proportionate to the Faraday angle. At the zero-frequency limit, we get a finite value of Faraday rotation, which is $2\alpha_F$, where α_F is the Fine structure constant. Our theory is general and applies to all 2D materials which hold nonsymmorphic symmetry. The results indicate that materials like these can be a suitable polarization rotator with high transmittance overall.

2.1 Model and Symmetries

We have taken the example of α-bismuthene as the nonsymmorphic material described in the reference [5]. According to this paper the Dirac cones exists at $\bar{X}_1 = (\pi, 0)$ and $\bar{X}_2 = (0, \pi)$ of the

Brillouin zone. α-Bi is nonmagnetic and centrosymmetric, so the time-reversal (T) and inversion (P) symmetries are preserved. The symmetries in this model can be described by the three generators:

$$\begin{aligned} \tilde{M}_z &: (x+1/2, y+1/2, -z)\ i\sigma_z \\ P &: (-x, -y, -z)\ \sigma_0 \\ M_x &: (-x, y, z)\ i\sigma_x \end{aligned} \tag{2.1}$$

Here, $\tilde{M}_z$ represents a nonsymmorphic glide mirror operation – the mirror reflection accompanied by a half lattice translation parallel to the mirror plane in the case of α-bismuthene. In Eq. (2.1), x, y z are spatial coordinates, while σ_i are Pauli matrices for the degree of freedom of spin. It describes the action of symmetry operators on the spatial coordinates and spin space. It would instead represent a screw-axis symmetry in the case of monolayer Bi. We can write the matrix representation of the symmetry operators as

$$\begin{aligned} T &= -i\sigma_y \otimes \tau_0 K \text{ (Time reversal)} \\ \tilde{M}_z &= \sigma_z \otimes \tau_y \text{ (Glide mirror)} \\ P &= \sigma_0 \otimes \tau_x \text{ (Parity)} \\ M_x &= -i\sigma_x \otimes \tau_x \text{ (Mirror -x)}, \end{aligned} \tag{2.2}$$

where K is the complex conjugation part which can be thought of as a 2×2 matrix. Here, σ_i $(i = x, y, z)$ are Pauli matrices for spin and τ_i $(i = x, y, z)$ are Pauli matrices for orbital degrees of freedom, respectively, and σ_0 and τ_0 are the 2×2 identity matrix [5]. The three symmetries mentioned in Eq. (2.1) guarantee four-fold band degeneracies in $\bar{X}_1$ and $\bar{X}_2$, and the key reason for this is the nonsymmorphic character of $\tilde{M}_z$ which leads to a special commutation relation with P.

Following the definition of the symmetry operators we can write the following relations

$$\tilde{M}_z P = T_{110} P \tilde{M}_z; \quad \left(\tilde{M}_z\right)^2 = -T_{110}; \tag{2.3}$$

These equations declare that the eigenvalues of the glide mirror operator are momentum dependent, and can be written as $g_z = \pm ie^{-ik_x/2 - ik_y/2}$. The $\bar{X}_i$-points are T-invariant momentum points, which ensure a degenerate Kramers partner ($|\Phi(\bar{X}_i)\rangle$, $T|\Phi(\bar{X}_i)\rangle$), and these must share the same eigenvalues. Furthermore, from the above equation, we can conclude that at the $\bar{X}_i$-points, the eigenvalues of the glide mirror operator are $g_z = \pm 1$; which is purely real. Moreover, because we have $\{\tilde{M}_z, P\} = 0$ at these momentum points $P|\Phi(\bar{X}_i)\rangle$, $TP|\Phi(\bar{X}_i)\rangle$ must be other degenerate partners of the states with opposite eigenvalues.

2.2 Model Hamiltonian without magnetic field

For our purpose, we first consider the Dirac cone $\bar{X}_1 = (\pi, 0)$ where the Hamiltonian can be written as:

$$\begin{aligned} H &= \rho v k_x (\cos\alpha\ \sigma_x \otimes \tau_z + \sin\alpha\ \sigma_0 \otimes \tau_y) + v k_y\ (\sigma_y \otimes \tau_z) \\ &= \rho v k_x (\cos\alpha\ \gamma_z + \sin\alpha\ \gamma_x) + v k_y \gamma_y\ , \end{aligned} \tag{2.4}$$

where $\gamma_z = \sigma_x \otimes \tau_z$, $\gamma_y = \sigma_y \otimes \tau_z$ and $\gamma_x = \sigma_0 \otimes \tau_y$. We define ρ as the anisotropy factor $\rho = \frac{v_x}{v_y}$ because it refers to the mismatch in the Fermi velocity along x and y-direction, where $v_y = v$ and $\rho v = v_x$. The angle α is what we termed the "mixing angle," which is also an intrinsic parameter of the model.

The $\tilde{M}_z$ symmetry helps us to decompose the Hamiltonian into two 2×2 matrices representing the $\tilde{M}_z$ even sector (eigenvalue +1) and odd sector (eigenvalue -1). For convenience, we chose the even sector to work with, corresponding to $\sigma_z = 1$, $\tau_y = 1$ and $\sigma_z = -1$, $\tau_y = -1$.

2.2.1 Construction of the reduced Hamiltonian

We can classify the eigenstates according to the eigenvalues of $\tilde{M}_z = \tau_y \sigma_z$. In this section, we construct the reduced 2×2 Hamiltonian for the symmetry sectors $\tilde{M}_z = 1$ and $\tilde{M}_z = -1$.

In the $\tilde{M}_z$-even sector (eigenvalue +1) a convenient basis is

$$v_1 = \frac{1}{\sqrt{2}} \begin{pmatrix} 1 \\ 0 \\ i \\ 0 \end{pmatrix}, \qquad v_2 = \frac{1}{\sqrt{2}} \begin{pmatrix} 0 \\ 1 \\ 0 \\ -i \end{pmatrix} \tag{2.5}$$

corresponding to $\sigma_z = 1, \tau_y = 1$ and $\sigma_z = -1, \tau_y = -1$ respectively. Simple algebra leads to the following reduced Hamiltonian in the $\tilde{M}_z$-even sector:

$$H_{\tilde{M}_z=1} = \rho v k_x (\cos\alpha \sigma_z + \sin\alpha \sigma_x) + v k_y \sigma_y \tag{2.6}$$

The eigenvector of $H_{\tilde{M}_z=1}$ are best expressed in the basis

$$\frac{v_1+iv_2}{\sqrt{2}} = \frac{1}{2}\begin{pmatrix} 1 \\ i \\ i \\ 1 \end{pmatrix}, \qquad \frac{v_1-iv_2}{\sqrt{2}} = \frac{1}{2}\begin{pmatrix} 1 \\ -i \\ i \\ -1 \end{pmatrix} \tag{2.7}$$

In this basis (i.e., interpreting $\frac{v_1+iv_2}{\sqrt{2}}$ as the conventional $|\uparrow\rangle$ and $\frac{v_1-iv_2}{\sqrt{2}}$ as the conventional $|\downarrow\rangle$), σ_z becomes σ_x, σ_x becomes σ_y, and σ_y becomes σ_z. Thus we have

$$\tilde{H}_{\tilde{M}_z=+1} = \rho v k_x(\sigma_x \cos\alpha \ + \sigma_y \sin\alpha) + v k_y \sigma_z \tag{2.8}$$

Similar manipulations for the $\tilde{M}_z$-odd sector (eigenvalue -1) lead to

$$\tilde{H}_{\tilde{M}_z=-1} = \rho v k_x(-\sigma_x \cos\alpha \ + \sigma_y \sin\alpha) + v k_y \sigma_z \, . \tag{2.9}$$

The anisotropy factor ρ is material-dependent. The two Dirac cones of bismuthene have different ρ values, namely, $\rho = 1.86$ at $\bar{X}_1$ and 0.25 at $\bar{X}_2$, because the two valleys are not connected by any crystal symmetries. In the following discussion, we will take ρ as a free parameter of the model and study the ρ-dependence of optical absorption.

In both cases, the eigenvalues are respectively.

$$E = \pm v\sqrt{\rho^2 k_x^2 + k_y^2} \tag{2.10}$$

Notice that we could reduce the whole Hamiltonian to 2×2 form only because the system has the glide mirror symmetry $\tilde{M}_z$.

2.3 Model Hamiltonian with Magnetic field

Introducing a magnetic field in this system reduces the symmetry. We go back to the original form of the Hamiltonian to find the eigenstates and eigenvectors. The Hamiltonian with the magnetic field is

$$\tilde{H} = \rho v k_x\big(\cos\alpha \ \gamma_z + \sin\alpha \ \gamma_x\big) + v k_y \gamma_y + \vec{B}\cdot\tau_0 \ \vec{\sigma}, \tag{2.11}$$

The direction of the magnetic field is described by polar (μ) and azimuthal angles (ν) such that

$$\vec{B} = B\,(\sin\mu\cos\nu, \sin\mu\sin\nu, \cos\mu)\,, \tag{2.12}$$

We also set

$$v\rho k_x = \bar{k}\cos\phi\,, \qquad v k_y = \bar{k}\sin\phi\,. \tag{2.13}$$

With this notation the energy eigenvalues are [1]

$$\bar{E}(\phi) = \pm\sqrt{B^2 + \bar{k}^2 \pm 2B\bar{k}F(\phi)}\,, \tag{2.14}$$

where

$$F(\phi) = \sqrt{(\cos\phi\cos\alpha)^2 + \sin^2\mu(\cos\phi\cos\nu\sin\alpha + \sin\phi\sin\nu)^2}\,, \tag{2.15}$$

The spectrum is generally gapped in presence of magnetic field. We find the band gap Δ using Eq. (2.14) as:

$$\frac{\Delta}{B} = 2\min\frac{|\bar{E}(\phi)|}{B} = 2\sqrt{1 - \frac{A + C + \sqrt{A^2 + C^2 + 2AC\cos(2\gamma)}}{2}}, \tag{2.16}$$

where we have defined

$$\cos(2\gamma) = \frac{\sin^2\alpha - \tan^2\nu}{\sin^2\alpha + \tan^2\nu}\,, \tag{2.17}$$

and

$$A = \cos^2\alpha\,, \qquad C = \sin^2\mu(\cos^2\nu\sin^2\alpha + \sin^2\nu). \tag{2.18}$$

In the special case of magnetic field along the z-axis ($\mu = 0$), we get $A = \cos^2\alpha$, $C = 0$, $\frac{\Delta}{B} = 2\sin\alpha$.

If the magnetic field is along the x-axis ($\mu = \pi/2, \nu = 0$), we have $A = \cos^2\alpha$, $C = \sin^2\alpha$, $\cos(2\gamma) = 1$, yielding $\Delta = 0$.

If the magnetic field is along the y-axis ($\mu = \pi/2, \nu = \pi/2$), we have $A = \cos^2\alpha$, $C = 1$, $\cos(2\gamma) = -1$, yielding $\Delta = 0$.

The bandgap along z-direction of field depends on the mixing angle α. Thus, by measuring the bandgap in the presence of a magnetic field one can determine the value of the mixing angle.

[1] Notice that the eigenvalues come in pairs of opposite signs. This is because the original Hamiltonian anti-commutes with the operator $\tau_z\boldsymbol{\sigma}\cdot(\tilde{\mathbf{k}}\times\mathbf{B})$ where $\tilde{\mathbf{k}}$ is a vector with components $(k_x\sin\alpha, k_y, 0)$.

2.4 Calculation of the constant energy contours

With $\bar{k} = \sqrt{\bar{k}_x^2 + \bar{k}_y^2}$, $\bar{k}_x = \rho v k_x/B = \bar{k}\cos\phi$, $\bar{k}_y = v k_y/B = \bar{k}\sin\phi$, and setting $B = 1$ as the unit of energy we define the conduction band energies as

$$E_{c1}(\bar{k},\phi) = \sqrt{1 + \bar{k}^2 - 2\bar{k}F(\phi)}\,, \quad E_{c2}(\bar{k},\phi) = \sqrt{1 + \bar{k}^2 + 2\bar{k}F(\phi)} \tag{2.19}$$

and $E_{v1} = -E_{c1}$, $E_{v2} = -E_{c2}$. The α, μ, ν-dependence of F is omitted. Notice that $\bar{k} > 0$ and $0 < F < 1$ so we have $E_{c1} < E_{c2}$ for all $\mathbf{k}$.

The constant excitation energy contour for $v1 \to c1$ transitions is

$$\begin{aligned} (v1 \to c1) : \bar{k}_+(\phi) &= F(\phi) + \sqrt{F(\phi)^2 + \left(\frac{\omega}{2}\right)^2 - 1} \\ \bar{k}_-(\phi) &= F(\phi) - \sqrt{F(\phi)^2 + \left(\frac{\omega}{2}\right)^2 - 1} \\ &\Delta < \omega < 2\,, \quad \phi_{min} < |\phi| < \phi_{max}\,. \end{aligned} \tag{2.20}$$

where ω is the excitation energy and the angles ϕ_{min}, ϕ_{max} are the positive solutions of the equation

$$F(\phi)^2 = 1 - \left(\frac{\omega}{2}\right)^2\,. \tag{2.21}$$

The constant energy contour for $v1 \to c2$ (or $v2 \to c1$) transitions is

$$\begin{aligned} (v1 \to c2) : \bar{k}(\phi) &= \frac{\omega}{2}\sqrt{\frac{\omega^2 - 4}{\omega^2 - 4F(\phi)^2}} \\ &\omega > 2 \end{aligned} \tag{2.22}$$

This is simply a closed loop around the origin.

Finally, the constant excitation energy contour for the $v2 \to c2$ transitions is

$$\begin{aligned} (v2 \to c2) : \bar{k}(\phi) &= -\bar{k}_-(\phi) = -F(\phi) + \sqrt{F(\phi)^2 + \left(\frac{\omega}{2}\right)^2 - 1} \\ &\omega > 2\,. \end{aligned} \tag{2.23}$$

Again, this is a closed loop around the origin.

Chapter 3

OPTICAL ABSORPTION COEFFICIENT OF NONSYMMORPHIC DIRAC SEMIMETALS

We here present our work on the calculation of the optical absorption coefficient of the aforementioned material with and without the presence of the magnetic field. We will assume that at least one nonsymmorphic Dirac node is present at the Fermi level and is directly accessible to photon absorption processes. Our model for nonsymmorphic 2D Dirac cone is spelled out in Eq. (2.4) and we will examine the role played by the intrinsic parameters of that model, i.e., the "anisotropy factor" and the "mixing angle". While the Dirac cone is expected, under this assumption, to be the main contributor to the low-frequency optical absorption spectrum, it is not possible, in general, to completely eliminate low-frequency contributions from metallic regions of momentum space, where the Fermi level crosses partially occupied bands. This point will be addressed in detail in the concluding section, where we will argue that the residual metallic absorption can be clearly separated from Dirac-cone absorption in sufficiently clean samples because it gives rise to a distinct Drude absorption peak.

To calculate the absorption coefficient we perform our calculations without and with the magnetic field, and in the latter case, we consider three orthogonal directions of the field. We find that a magnetic field perpendicular to the plane opens a gap in the spectrum. The magnitude of this gap can be related to the internal "mixing angle" – a quantity not directly accessible from the band structure in the absence of a magnetic field. On the other hand, an in-plane magnetic field leaves the system gapless but splits the Dirac nodes. For one direction of the magnetic field, a Van-Hove singularity appears in the joint density of states. It is associated with a change in the topology of the constant energy contours at a saddle point in the band structure. The logarithmic divergence of the joint density of states leads to enhanced absorption for one direction of the photon polarization

but not for the orthogonal one, which implies that the absorption coefficient is very sensitive to the polarization of the incident light when the frequency approaches the Van-Hove singularity.

One of our significant findings is that the absorption coefficient can be tuned by changing the polarization and frequency of the incoming wave. This tunability is further enhanced by the intrinsic anisotropy of the Dirac cones. These results open the door to interesting magneto-optical applications of 2D nonsymmorphic Dirac materials.

3.1 Mathematical framework to calculate the optical absorption coefficient

The electromagnetic interaction is given by $\vec{J}\cdot\vec{A}(t)$, where $\vec{J}=\frac{\partial H}{\partial \vec{k}}$ is the current operator with components

$$J_x = \rho v(\cos\alpha\ \sigma_x\otimes\tau_z + \sin\alpha\ \sigma_0\otimes\tau_y)\,,\quad J_y = v\tau_z\sigma_y\,. \tag{3.1}$$

and $\vec{A}(t)$ is the vector potential

$$\vec{A}(t) = A_0\cos(\omega t)\ \mathbf{e}, \tag{3.2}$$

where A_0 is the amplitude of the electromagnetic wave and the polarization vector $\mathbf{e}$ is defined as. [1]

$$\mathbf{e} = \cos\beta\hat{\mathbf{x}} + e^{i\delta}\sin\beta\hat{\mathbf{y}} \tag{3.3}$$

The optical transition probability is

$$W_{v\to c}(\omega) = \frac{A^2v^2}{2\pi\hbar}\sum_j\int_0^\infty d\bar{k}\bar{k}\int_{\phi_{min}}^{\phi_{max}} d\phi\ |M_j(\phi)|^2\frac{\delta(\bar{k}-\bar{k}_j(\phi))}{|d(E_c-E_v)(\bar{k},\phi)/d\bar{k}|}, \tag{3.4}$$

where $\bar{k}_j(\phi)$, with $j=+$ or $-$ are the constant energy contours at the transition energy ω, i.e., the solutions of the equation $E_c(\bar{k},\phi)-E_v(\bar{k},\phi)=2\hbar\omega$, and $v\to c$ refers to the transition from the valence band to the conduction band. The squared matrix element of the current operator is given by

$$|M_j(\phi)|^2 \equiv \left|\langle\psi_{cj}(\phi)|\rho^{1/2}\ \cos\beta\ J_x + e^{-i\delta}\rho^{-1/2}\ \sin\beta\ J_y|\psi_{vj}(\phi)\rangle\right|^2\,, \tag{3.5}$$

where

$$|\psi_{vj}(\phi)\rangle \equiv |\psi_v(\bar{k}_j(\phi),\phi)\rangle\,,\quad |\psi_{cj}(\phi)\rangle \equiv |\psi_c(\bar{k}_j(\phi),\phi)\rangle. \tag{3.6}$$

[1] We are working in low energy regime thus using the dipole approximation and neglecting the photon momentum.

are, respectively, the valence and conduction band states evaluated at the iso-energy surface, i.e., $\bar{k} = \bar{k}_j(\phi)$. From Eq. (3.4) we have an expression for the transition probability that we can utilize to calculate the optical absorption from different pairs of bands (e.g, $v_1 \to c_1$ or $v_1 \to c_2$), with or without the magnetic field.

For example, if we consider only intra-valley transition $v_1 \to c_1$ we find that the transition probability is

$$W_{v1\to c1}(\omega) = \frac{A^2\omega}{2\pi\hbar}\int_{\phi_{\min}}^{\phi_{max}} d\phi \frac{k_+(\phi)|M_+(\phi)|^2 + k_-(\phi)|M_-(\phi)|^2}{\sqrt{F(\phi)^2 + \left(\frac{\omega}{2}\right)^2 - 1}}\ , \tag{3.7}$$

where ω is the excitation energy and has value $\Delta < \omega < 2B$ (Δ is the bandgap of the system). Here ϕ_{min} and ϕ_{max} are the lower and upper limits of integration, defined by the solutions of the equation

$$F(\phi)^2 = 1 - \left(\frac{\omega}{2}\right)^2\ . \tag{3.8}$$

The two branches of the energy contours $\bar{k}_\pm(\phi)$ coincide at ϕ_{min} and ϕ_{max} and thus combine to produce closed contours around the minimum excitation energy (Look into the supplementary material section 1.4 for calculation of the iso-energy contours).

3.2 Results and Discussions

Based on the mathematical framework described before, we can calculate the optical absorption coefficient for a general direction polarization with and without the magnetic field. First, we start with the case where there is no magnetic field in our system, and later we introduce a magnetic field in different directions.

3.2.1 Optical absorption coefficient without the magnetic field

In this case, as there is no magnetic field present, we have used the reduced Hamiltonian Eq. (2.8) for $\tilde{M}_z = +1$. The glide mirror symmetry holds for this case and has distinct eigenvalues for the two valleys ($\tilde{M}_z = \pm 1$), which prevents inter-valley transitions. As a result, we end up with only intra-valley transitions (i.e., $v_1 \to c_1$ or $v_2 \to c_2$ which are exactly equal). For the valley $\bar{X}_1$, we get the transition probability

$$W_{v1\to c1} = \frac{A^2\omega}{8}\Big(\rho\ \cos^2\beta + \rho^{-1}\sin^2\beta\Big), \tag{3.9}$$

The optical absorption coefficient calculated [32] for the general direction of polarization without magnetic field takes the form:

$$\eta = \frac{\pi e^2}{2\hbar c} f(\rho, \beta)\,, \tag{3.10}$$

where we have defined the *birefringence* function

$$f(\rho, \beta) = \left(\rho\ \cos^2\beta\ +\ \rho^{-1}\ \sin^2\beta\right)\ . \tag{3.11}$$

We have reinstated the $\hbar$ to get the dimensionless quantity, the fine structure constant ($\frac{e^2}{\hbar c} = 1/137$). This expression of optical absorbance is calculated for a single valley (which in the case of α-bismuthene could be either the $\bar{X}_1$ or the $\bar{X}_2$ valley) as a function of the anisotropy factor ρ. It is also evident that this result is very similar to the well-known result for graphene, [2] in that the absorption coefficient is frequency-independent, but now it has a strong polarization dependence, as indicated by the *birefringence* function. For large anisotropy ($\rho \ll 1$ or $\rho \gg 1$) the absorption coefficient can change by a significant factor upon rotating the polarization angle.

3.2.2 Optical absorption coefficient in the presence of a magnetic field along the z-direction

When working with the magnetic field along the z-direction, the Zeeman term preserves the glide mirror symmetry; thus, we can still decouple the Zeeman term for even and odd sectors under the glide mirror symmetry operator. The Zeeman term $B\tau_0\sigma_z$ can be reduced to $B\sigma_z$ in the even sector and $-B\sigma_z$ in the odd sector. We have used the reduced Hamiltonian for the even sector of $\tilde{M}_z$ (Eq. (2.8)) and added the Zeeman term:

$$H'_{M_z=1} = (\rho v k_x \cos\alpha + B)\sigma_x\ +\ \rho v k_x \sin\alpha\sigma_y\ +\ v k_y \sigma_z\ , \tag{3.12}$$

We write the eigenvalues as

$$E = \pm v\sqrt{\left(\rho k_x + \frac{B}{v}\cos\alpha\right)^2 + k_y^2 + \frac{B^2}{v^2}\sin^2\alpha}\ . \tag{3.13}$$

From Fig. 3.1(a), we see the energy bands when the magnetic field is along the z-direction, and there exists a gap equal to $\Delta = 2B\sin\alpha$ (Eq. (2.16)), which means the bandgap has dependence over the intrinsic quantity "mixing angle".

[2] The absorbance for monolayer graphene is $\eta_{graphene} = \frac{\pi e^2}{\hbar c}$.

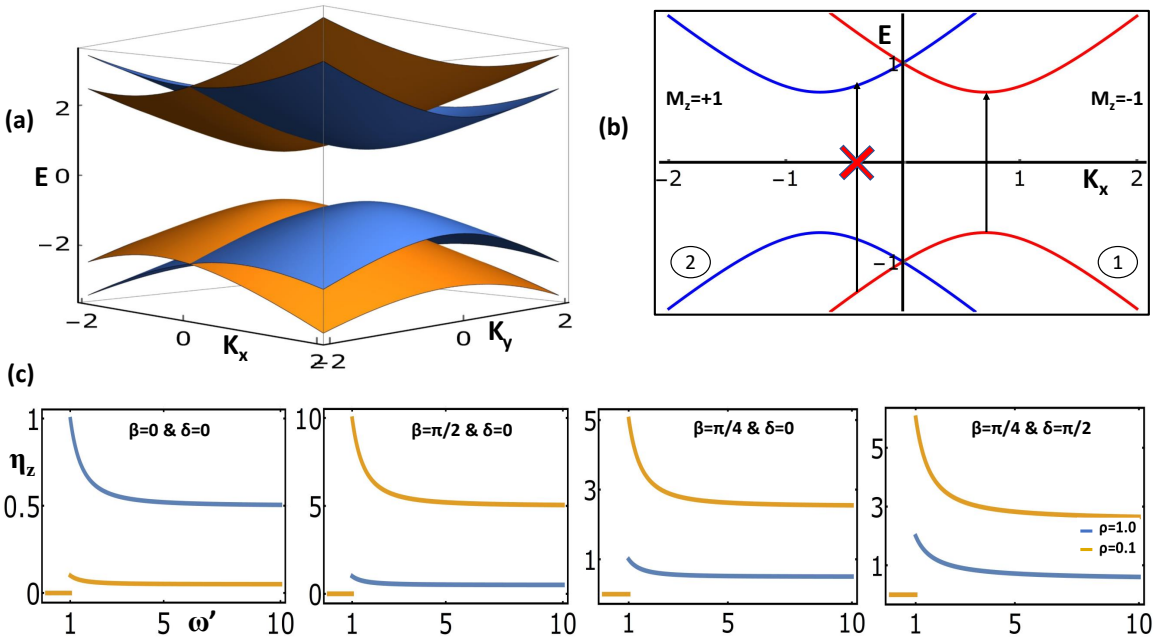

Figure 3.1: *(a) Three-dimensional plot of the band dispersion for the magnetic field in the z-direction. Notice that there is a band gap $\Delta = 2B\sin\alpha$ at two points separated by a wave vector proportional to B_z along k_x. The momenta k_x and k_y are in units of $\frac{B}{v}$ and the energy is in units of B. **(b)** This figure shows that only intra-valley transitions are possible as the two valleys hold opposite eigenvalues for $\tilde{M}_z$. **(c)** Plot of the optical absorption coefficient vs scaled frequency $\omega' = \frac{\omega}{2B\sin\alpha}$ for four different polarizations. The plot starts at $\omega \geq 2B\sin\alpha$.*

Both the current operators J_x and J_y and our Hamiltonian (Eq. (3.12)) commutes with $\tilde{M}_z$, which makes the transitions preserve the parity of $\tilde{M}_z$. In Fig. 3.1(b), we have shown the two valleys have opposite symmetries against the glide mirror symmetry for the z-direction of the magnetic field, and hence inter-valley transitions are not allowed.

Calculations similar to the previous section for optical absorbance (η_z) for the $\bar{X}_1$ valley leads us to

$$\eta_z = \frac{\pi e^2}{2\hbar c}\left[f(\rho,\beta)(1+\frac{4B^2}{\omega^2}\sin^2\alpha)+\frac{4B}{\omega}\sin\alpha\sin\delta\sin 2\beta\right]. \tag{3.14}$$

The *birefringence* function that appears in this expression will let us control the absorbance with the polarization of light. Also, it has a dependence on the frequency. For the $\bar{X}_2$ valley the expression is exactly the same with a different value for the anisotropy factor.

To understand the effect of the anisotropy factor on the absorbance, we assumed one Dirac point to be nearly isotropic ($\rho \approx 1.0$) and the other Dirac point to be highly anisotropic ($\rho \approx 0.1$). In Fig. 3.1(c), we have plotted the optical absorption coefficient (Eq. 3.14) with frequency (scaled frequency $\omega' = \frac{\omega}{2B\sin\alpha}$) for both the isotropic and anisotropic Dirac points for four different polarization. From these figures, one can see when the polarization is along x-direction ($\beta = 0; \delta = 0$)

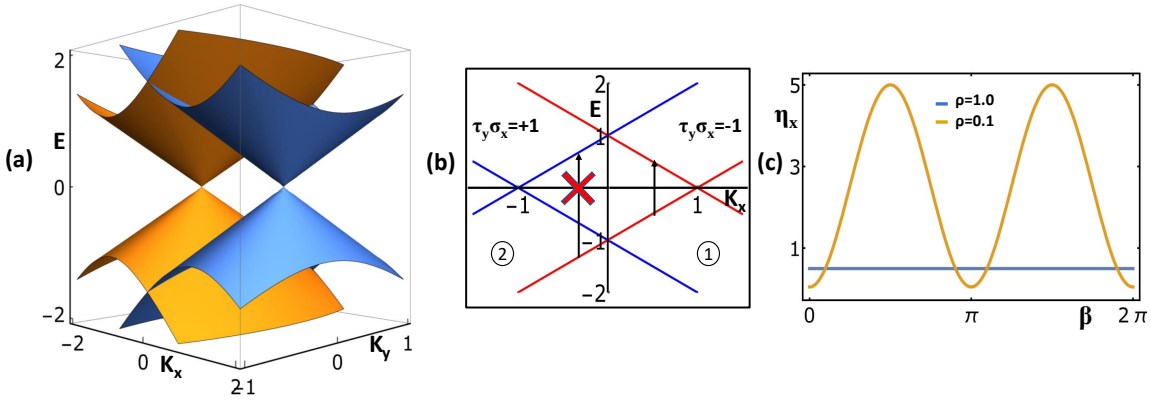

Figure 3.2: ***(a)*** *Three-dimensional plot of the energy bands for the magnetic field along the x-direction. The spectrum is gapless.* ***(b)*** *This figure shows that only intra-valley transitions are possible as the two valleys hold opposite eigenvalues of $\tau_y\sigma_x$.* ***(c)*** *Plot of the absorption coefficient η_x vs β for $\alpha = \pi/4$, for two different values of ρ, referring to the isotropic ($\rho = 1.0$) and the anisotrpic ($\rho = 0.1$) valley respectively. The absorption coefficient is in a unit of $\eta_{grahene}$.*

(Fig. 3.1(c(i)) the dominating Dirac point is the isotropic one ($\rho = 1.0$) unlike the other cases where the anisotropic ($\rho = 0.1$) case prevails in the absorption spectrum.

It shows when we change the polarization to the x-direction ($\beta = 0; \delta = 0$), we can significantly decrease the total absorbance, whereas if we switch to y-polarisation ($\beta = \pi/2; \delta = 0$) we increase the total absorption by an order of magnitude. This shows the Dirac point mainly contributing to the enhancement of the absorbance is the anisotropic one, and this is due to the *birefringence* function present in the expression.

3.2.3 Optical Absorption Coefficient in the presence of the Magnetic Field along the x-direction

For the magnetic field at x-direction, the Hamiltonian can be written as

$$H = \rho v k_x \ \cos\alpha \ \gamma_z + \rho v k_x \ \sin\alpha \ \gamma_x + v k_y \gamma_y + B_x \ \tau_0 \sigma_x \ , \tag{3.15}$$

The corresponding eigenvalues are:

$$E = \pm\sqrt{(\rho v k_x \pm B)^2 + v^2 k_y^2} \ , \tag{3.16}$$

From Fig. 3.2(a), we see that there is no bandgap, and the two valleys cross each other. Similarly to the z-direction, we find that a symmetry operator $\tau_y\sigma_x$ is present in this case, which commutes with the current operators and the Hamiltonian. This has opposite signs in the two valleys (shown

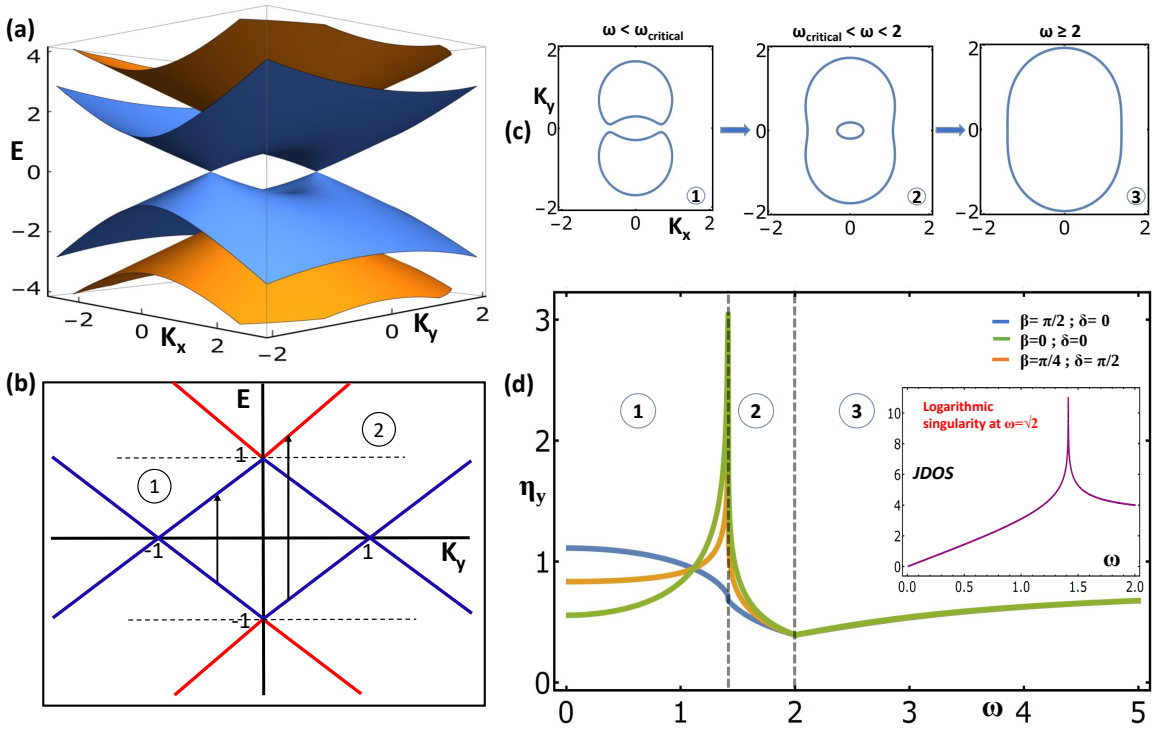

Figure 3.3: ***(a)*** *Plot of the energy bands for magnetic field along the y-direction for the $\bar{X}_1$ valley. There is no gap for transitions from v_1 to c_1, as these two bands touch at the Dirac points $(0, \pm B/v)$. On the other hand, the v_2 and c_2 bands are separated by a gap $2B$ at $(0,0)$.* ***(b)*** *Plot of the band dispersion along the line $k_x = 0$. Notice that both "intra-valley" ($v_1 \to c_1$) and "inter-valley" ($v_1 \to c_2$) transitions are possible, the latter only for frequencies larger than $2B$.* ***(c)*** *Change of topology of the iso-energy contours with increasing excitation energy. The first change in topology occurs at the saddle-point frequency $\omega = 2B\sin\alpha$, the second at $\omega = 2B$.* ***(d)*** *Plot of the absorption coefficient η_y (in units of $\eta_{graphene} = \frac{\pi e^2}{\hbar c}$.) vs. ω for $\alpha = \pi/4$. Notice the logarithmic singularity at $\omega = 2B\sin\alpha$ and the cusp at $\omega = 2B$. These features are related to the changes in the topology of the iso-energy contours shown in panel (c). Inset: joint density of states as a function of ω showing a logarithmic divergence at the saddle point $\omega = 2B\sin\alpha$, where $\alpha = \pi/4$.*

Fig. 3.2(b)) and thus only allows intra-valley transitions for optical absorption. This symmetry operator $\tau_y\sigma_x$ (product of the two broken symmetries, time reversal, and glide mirror) protects Dirac cones even though time-reversal symmetry is broken due to the presence of the magnetic field.

For each valley, we get the optical absorption coefficient in the form:

$$\eta_x = \frac{\pi e^2}{2\hbar c}\, f(\rho, \beta)\,, \tag{3.17}$$

which coincides with the result obtained with no magnetic field.

3.2.4 Optical absorption coefficient in the presence of a magnetic field in the y-direction

For a magnetic field in the y-direction, the Hamiltonian can be written as

$$H = \rho v k_x \cos\alpha \gamma_z + \rho v k_x \sin\alpha \gamma_x + v k_y \gamma_y + B_y \tau_0 \sigma_y \,, \tag{3.18}$$

where the γ matrices are defined after Eq. (2.4). Its eigenvalues are

$$E = \pm\sqrt{\left(\sqrt{(\rho v k_x \cos\alpha)^2 + (v k_y)^2} \pm B\right)^2 + \left(\rho v k_x \sin\alpha\right)^2} \,. \tag{3.19}$$

Let us start our calculation for the magnetic field in y-direction by keeping $\rho = 1$ (isotropic valley). This means that the only source of anisotropy is the magnetic field itself. From Fig. 3.3(a) we see that the Dirac point, which initially was at $\bar{X}_1$, is split by the magnetic field term $B\tau_0\sigma_y$ into two distinct Dirac points located at $k_x = 0$, $k_y = \pm B/v$. The two Dirac points are related to each other by parity symmetry ($\sigma_0\tau_x$ combined with the inversion of $\mathbf{k}$), which remains intact in this case. The bands emanating from the two Dirac cones (depicted in blue in Fig. 3.3(a)) account for the low-frequency part of the absorption spectrum. The high and low energy bands, depicted in orange in Fig. 3.3(a), become degenerate with the blue bands at the $\bar{X}_1$ point ($k_x = k_y = 0$), as required by parity symmetry. Also, this band dispersion gives rise to a saddle point at $k_x = \cos\alpha, k_y = 0$ as can be directly verified from Eq. (3.19). The singularity occurs in the "blue" bands, and the transition frequency associated with it is $\omega_{critical} = 2B\sin\alpha$.

We performed numerical calculations for the absorption coefficient in the presence of a magnetic field along the y-direction. There is no selection rule from the symmetry constraints in this case. Thus we have included all the possible transitions (inter-valley transitions i.e., $v_1 \to c_2$ together with intra-valley transitions i.e., $v_1 \to c_1$) and obtained the optical absorption coefficient as shown in Fig. 3.3(d). Notice that we only have intra-valley transitions for $\omega \leq 2B$. For $\omega \geq 2B$ we include $v_1 \to c_2$ and $v_2 \to c_2$ transitions.

The absorption spectrum has a logarithmic singularity at the saddle-point frequency $\omega = \omega_{critical} = 2B\sin\alpha$ (Fig. 3.3(d)). Furthermore, this singularity is prominent only for light polarized along the x-direction ($\beta = 0, \delta = 0$).

To understand the origin of this singularity we have calculated the joint density of states (JDOS)

which is defined as

$$g(\omega) = \sum_{\mathbf{k}} \delta\big(\omega - E_c(\mathbf{k}) - E_v(\mathbf{k})\big) = \frac{1}{2\pi\rho v^2} \sum_j \int_0^\infty d\bar{k}\bar{k} \int_{\phi_{min}}^{\phi_{max}} d\phi \frac{\delta(\bar{k} - \bar{k}_j(\phi))}{|d(E_c - E_v)(\bar{k},\phi)/d\bar{k}|} \ , \quad (3.20)$$

In the vicinity of $\omega_{critical}$ this evaluates to

$$g(\omega) \simeq \frac{\omega}{\pi\rho v^2} \cot\alpha \ln\left|\frac{\sin\alpha}{\omega - \omega_{critical}}\right| . \quad (3.21)$$

Thus we see that the logarithmic singularity in the absorption spectrum for x-polarization reflects an underlying singularity in the JDOS. This singularity can also be understood by observing the change in the topology of the iso-energy contours which occurs at $\omega_{critical}$, as illustrated in panel (c) of Fig. 3.3. This effect – akin to the change of Fermi surface topology in a Lifshitz transition – is entirely induced by the magnetic field. The downward cusp in the absorption spectrum around $\omega = 2B$ can also be understood due to the vanishing of the inner iso-energy contour at this excitation frequency, as shown Fig. 3.3(c(2)).

It remains to be explained why the absorption spectrum does not have a logarithmic divergence at $\omega = \omega_{critical}$ when the incident light is polarized in the y-direction. In fact, in this case, we only observe a small downward cusp at $\omega = \omega_{critical}$. The reason for this difference becomes clear when we consider the behavior of the squared matrix elements of the current operators (J_x and J_y) at the saddle point. The matrix element of J_y vanishes at the saddle point energy, whereas the matrix element of J_x remains finite. This is further discussed in the Appendix A.1.

The scenario described in the previous paragraphs is not related to band anisotropy, which should be evident from the fact that we observed a strong polarization dependence of the absorption spectrum even though the anisotropy parameter ρ was set to 1 (we have discussed the optical absorbance for the anisotropic Dirac cone and the total absorbance in the Appendix A.2. The scenario is also robust with respect to variations of the mixing angle α: while the plots of Fig. 3.3 have been obtained for $\alpha = \pi/4$, we find the same qualitative behavior for other values of α (Appendix A.3).

3.3 Summary and conclusion

In this work, we have reported a detailed theoretical analysis of the photon absorption spectrum for a generic model of nonsymmorphic 2D semimetals with and without a magnetic field. In the absence of a magnetic field, the absorption coefficient is very similar to the absorption coefficient for

graphene, which is $\frac{\pi e^2}{\hbar c} = 2.3\%$ but multiplied by the *birefringence* function we define in Eq. (3.11). For a strongly anisotropic cone with $\rho \ll 1$, $f(\rho, \beta)$ grows as $1/\rho$, which leads to an order of magnitude enhancement of the absorption coefficient for the anisotropic valley. Furthermore, this enhancement is highly sensitive to the direction of the photon polarization, as can be seen from the $\sin^2 \beta$ factor in the *birefringence* function. This function together with the photon polarization can enable a valley selection in the absorbance spectrum in the case that a nearly isotropic valley and a strongly anisotropic valley are present near the Fermi level.

Upon switching on the magnetic field, the absorption spectrum becomes frequency-dependent, and the absorption function is also coupled with anisotropy factor ρ and the mixing angle α. We now have more than one control parameter at hand to tune the absorption coefficient, which enables us to tune the absorption coefficient efficiently by varying the photon polarization angle β. The range of tunability of the total absorbance (taking both isotropic and anisotropic valley into account) is quite broad, going from 1 to up to 10 in units of $\eta_{graphene}$, which is larger than that envisaged in previous works [33, 34]. A magnetic field perpendicular to the plane opens a gap $2B \sin \alpha$, whose observation allows an experimental determination of the hidden "mixing angle" α. On the other hand, an in-plane magnetic field leaves the system gapless but splits the Dirac cones and makes absorption more sensitive to photon energy. For example, in Fig. 3.3(d), we plotted the absorption coefficient for a magnetic field along the y-direction as a function of frequency for different photon polarizations. The Van Hove singularity in the joint density of states, from the saddle point in the band dispersion [35], gives rise to a sharp peak in the absorption spectrum and thus greatly enhances the photon absorption at the critical frequency.

We note that the generic band model of 2D Dirac semimetals is employed in this work, and thus the results can be applied to study the optical properties of all Dirac semimetals with different nonsymmorphic lattice symmetries. The significant tunability in photon absorption enabled by the band anisotropy and external magnetic fields establishes nonsymmorphic 2D Dirac semimetals as a promising platform for optoelectronic and magnetoelectronic device applications.

We conclude with a few comments on the prospects of observing the features described in this paper in experiments on realistic materials such as α-bismuthene. We have already mentioned the problem of positioning the symmetry-protected Dirac cone at the Fermi level, or, at least, very close to it. This can be achieved by doping or by the application of mechanical stress. However, the proper positioning of the Dirac point is not sufficient to guarantee that the low-frequency portion of the optical absorption spectrum will be dominated by interband transitions between the lower and the upper Dirac cone. The reason is that, in general, there are partially occupied bands giving

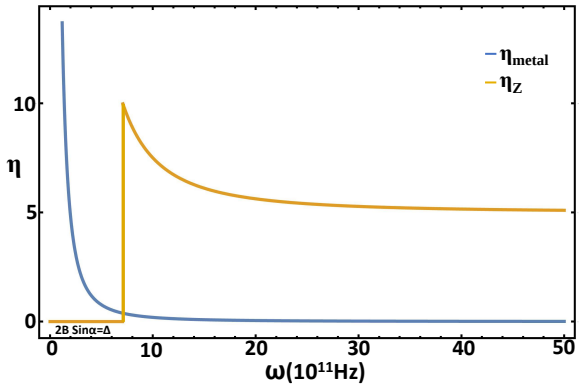

Figure 3.4: *Estimated metallic absorption coefficient (η_{metal} – blue line) vis-a-vis the absorption coefficient due to the Dirac cone with a magnetic field B perpendicular to plane (η_z – orange line) vs. frequency (ω – in units of 10^{11} Hz.). Our estimate of metallic absorption is based on the Drude formula for metallic conductivity, with Fermi energy on the order of 0.1 eV and momentum relaxation time $\tau = 10^{-10}s$. We also take B= 5 T and $\alpha = \pi/4$. For this very clean system, the metallic absorption is a Lorentzian with a finite and sharp peak. It is well separated from the Dirac-cone absorption and the latter can be measured with negligible contribution from the former. The absorption coefficient is in units of $\frac{\pi e^2}{\hbar c} \simeq 0.023$.*

rise to a low-frequency metallic absorption background, which can obscure the signal from the Dirac cone. What saves the day is the fact that, in a sufficiently clean system, this background absorption (arising from intraband transitions within the partially occupied bands) has the form of a Drude peak at zero frequency with a width given by the inverse of the momentum relaxation time τ. The bandgap for magnetic field in the z-direction is $2B\sin\alpha$, and the photon absorption from interband transition starts above the gap. Assuming a magnetic field of 1 Tesla ($\approx 10^{-23}$Joules) the width of the Drude peak becomes smaller than the gap for τ greater than $\approx 10^{-11}s$.

The Drude contribution to the absorption coefficient is calculated by dividing the power dissipated in the layer per unit area, $W_o = Re(j.E) = Re(\sigma)E^2$, where $j = \sigma E$ is the current density and σ is the Drude conductivity of the carriers in the partially filled band, by the incident power $W_i = cE^2/(4\pi)$. The result is

$$\eta_{metallic} = \frac{W_0}{W_i} = \frac{4\pi Re(\sigma)}{c}\,. \tag{3.22}$$

Inserting the well-known expression for the Drude-conductivity of a two-dimensional electron gas, $\sigma = \frac{\sigma_0}{1-i\omega\tau}$, where $\sigma_0 = \frac{ne^2\tau}{m}$ and $n = \frac{m\epsilon_F}{\pi\hbar^2}$ is the two-dimensional carrier density and ϵ_F is the Fermi energy, we arrive at

$$\eta_{metallic} = \frac{\pi e^2}{\hbar c}\frac{4\epsilon_F\tau/\pi\hbar}{1+(\omega\tau)^2}\,. \tag{3.23}$$

This absorption spectrum is plotted in Fig. (3.4) vis-a-vis the one from the Dirac cone (η_Z). We have assumed a relaxation time $\tau = 10^{-10}s$, a Fermi energy of 0.1 eV, and a magnetic field of

5 T, which leads to a peak width at half maximum of about ($\mathcal{FWHM} = \frac{2\hbar}{\tau}$) 0.36 Tesla which is significantly smaller than the energy scale ($2B\sin\alpha \approx 7T$) on which the most interesting features of our nonsymmorphic model (for example, the magnetic field-induced van Hove singularity) appear. Notice that the metallic absorption spectrum is in the form of a Lorentzian ($\frac{A}{\pi}\frac{\tau}{(1+(\omega\tau)^2}$), thus the absorption coefficient remains finite at zero frequency. Choosing a sufficiently large relaxation time we can get the width of the Drude peak to be very narrow. Theoretical studies of two-dimensional materials have shown that large values of the momentum relaxation time are possible [36, 37]. Therefore we are hopeful that for very clean materials, it will be possible to achieve $\tau \approx 10^{-10}s$ experimentally. Thus, in sufficiently clean materials the spectral features predicted in this paper can be clearly distinguished from the Drude peak arising from the partially occupied bands.

Chapter 4

FARADAY AND KERR EFFECT OF NONSYMMORPHIC DIRAC SEMIMETALS

4.1 Introduction

The Dirac semimetals with nonsymmorphic symmetry are a comparatively recent addition to the 2D material family. These materials feature Dirac points that are not gapped by spin-orbit coupling and are protected by nonsymmorphic lattice symmetry [5, 25]. Specific realizations of these materials have recently been proposed to occur in the nonsymmorphic monolayer film of α-bismuthene, the monolayer of bismuth (MBi), black phosphorene, PtPb4, and in several others, and more details on the lattice structures and symmetries can be found in Refs. [5, 38, 39, 40, 41, 42, 43, 44].

In our paper (Ref. [38]) discussed in the previous chapter, we have shown that nonsymmorphic Dirac semimetals are very interesting when the Zeeman coupling breaks the time-reversal symmetry and opens a gap. As a result, it creates sharp features in the optical absorption spectrum. In addition, these materials are intrinsically anisotropic and therefore exhibit the phenomenon of optical birefringence. In the context of 2D materials, for a TRS broken system, the rotation of the polarization of the transmitted (reflected) light, i.e., the Faraday (Kerr) effect, can be used to deduce the off-diagonal element of the optical conductivity σ_{xy} as was shown for monolayer graphene by Crassee et al. [45]. Nandkishore and Levitov have recently proposed that the quantum anomalous Hall state could be observed by measuring the Kerr rotation [46] in bilayer graphene samples. Inspired by the various interesting physics one can get from a gapped nonsymmorphic 2D Dirac semimetal, we investigate the magneto-optical properties like Faraday and Kerr rotation in our paper, owing to their invaluable scientific and engineering applications. In an applied context, these effects can be used for nondestructive material characterization, magneto-optical memory, magnetic field or current

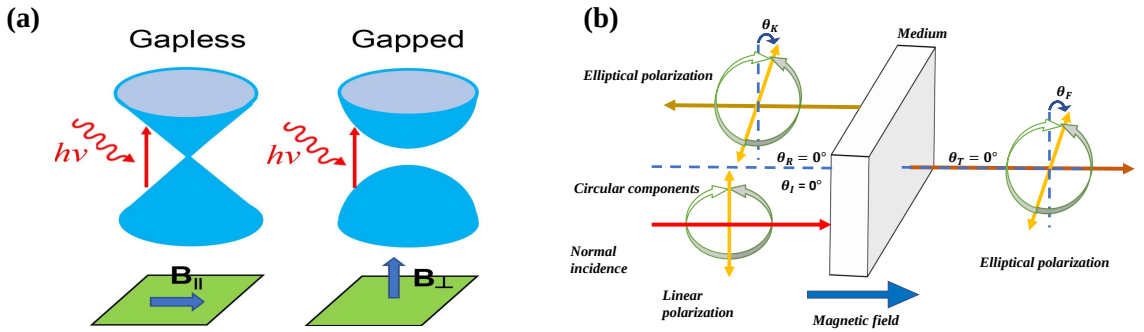

Figure 4.1: ***(a)*** *Schematic band diagram of a nonsymmorphic two-dimensional Dirac semimetal in the presence of a magnetic exchange potential. The exchange potential (in the form of a Zeeman term) creates the gap in otherwise linearly dispersing bands when it couples to out-of-plane spin. For an in-plane spin coupling, there is no gap.* ***(b)*** *Schematics of the Faraday and Kerr rotation effects. In our study, we consider light incident normal to the plane: thus, we keep the* $\boldsymbol{\theta}_I = 0$ *and* $\boldsymbol{\theta}_R = 0$.

sensing, polarization rotators, and nonreciprocal optical devices (isolator, circulator)[47, 48].

For a single atomic layer, whose thickness is much smaller than the wavelength of the incident light, the relationship between the Hall conductivity and Faraday (Kerr) angle $\theta_F(\theta_K)$ can be derived by solving the Maxwell equations on the two sides of the atomic layer and matching solutions at the boundary. Such a derivation is worked out for bilayer graphene in Ref. [45, 49], for thin films of topological insulators in Ref. [50, 51, 52], and for thin films of topological Weyl semimetals in Ref. [53, 54]. However, the chiral response of 2D nonsymmorphic Dirac materials has not been systematically investigated.

Here we present our derivation of the Faraday and Kerr rotation angles for a nonsymmorphic Dirac semimetal model, including intrinsic anisotropy. We consider an effective Zeeman coupling arising from exchange interactions with magnetic impurities or a nearby magnetized film [55, 56, 57]. The out-of-plane coupling of the exchange potential to the spin gives rise to a gap in the Dirac cone (proximity effect) whether an in-plane coupling does not[41, 50, 58, 59, 60]. This exchange potential can be tuned by changing the magnetization in the ferromagnetic insulator. Based on this model, we calculate the complete frequency-dependent optical conductivity tensor, including diagonal and off-diagonal (Hall) terms, and using that, we construct the frequency-dependent transmission (reflection) matrix. When acting on the polarization vector of the incident light, this matrix gives out the polarization of the transmitted or reflected light. Through a simplified approach, we calculate the change in the direction of polarization of a linearly polarized wave upon transmission or reflection and show that the Faraday rotation angle is significantly enhanced as the frequency of the incident light approaches the threshold for optical absorption. In the appendix, we provide complete analytical formulas to calculate the Faraday and the Kerr rotation angles for a general state of polarization of

the incident light and show that a single complex Faraday or Kerr rotation angle can describe the change in the polarization state. As a special case, we show that linearly polarized incident light acquires, upon transmission/reflection, an elliptic component of polarization, which is caused by the anisotropy of the system.

4.2 Model Hamiltonian

It is well known that two-dimensional materials with nonsymmorphic symmetries, such as glide mirror and screw-axis ([61, 62]), support symmetry-protected level crossings at time-reversal invariant points in the Brillouin zone. For example, α-bismuthene (α-Bi), with a glide-mirror symmetry $\tilde{M}_z$ [5, 38] has symmetry-protected Dirac points at points $\bar{X}_1 = (\pi, 0)$ and $\bar{X}_2 = (0, \pi)$ of the Brillouin zone. The points X_1 and X_2 are not related to each other by a symmetry operation of the material. Therefore the corresponding Dirac cones will have, in general, different dispersions and different energies at the crossing point. We note that having symmetry-protected Dirac points does not guarantee that these points will occur in close vicinity of the Fermi level, where they can control the electronic properties of the material. We will assume that at least one of the Dirac points is indeed at the Fermi level: this is not too far from reality for the X_1 point of α-Bi.

A general Hamiltonian that captures the low-energy dispersion of nonsymmorphic Dirac semimetals near the Dirac point has been derived in Ref. ([5, 38]). It has the form

$$H = \rho v k_x (\cos\alpha \ \sigma_x \otimes \tau_z + \sin\alpha \ \sigma_0 \otimes \tau_y) + v k_y \ (\sigma_y \otimes \tau_z)\,, \tag{4.1}$$

where the Pauli matrices σ and τ refer to spin degrees of freedom and orbital degrees of freedom, respectively – the orbital degrees of freedom are associated with p-orbitals of the atomic sites of the α-Bismuthene lattice [5]. The essential glide-mirror symmetry is represented by the operator $\tilde{M}_z = \sigma_z \otimes \tau_y$, while the remaining time-reversal, inversion, and the x-mirror symmetries are represented by $T = -i\sigma_y \otimes \tau_0 K$, $P = \sigma_0 \otimes \tau_x$ and $M_x = -i\sigma_x \otimes \tau_x$ respectively.

In Eq. (4.1) we have introduced ρ as the anisotropy factor $\rho = \frac{v_x}{v_y}$ which gives the ratio of the Fermi velocities along x and y-direction, where $v_y = v$ and $\rho v = v_x$. For example, in α-Bi, the Dirac cones at X_1 and X_2 have $\rho = 1.86$ and $\rho = 0.25$, respectively (again, this difference is allowed because the two valleys at X_1 and X_2 are not connected by any crystal symmetries). The angle α, which we call the "mixing angle", is also an intrinsic parameter of the model and is related to the spin-orbit coupling of the system. While α does not affect the dispersion of the bands in the absence of a gap,

it plays a central role in determining the magnitude of the gap that appears when the time-reversal symmetry is broken, and a gap opens up.

The $\tilde{M}_z$ symmetry allows us to decompose the 4×4 Hamiltonian into two 2×2 blocks representing the $\tilde{M}_z$ even sector (eigenvalue $+1$) and odd sector (eigenvalue -1). Since the eigenvalues are the same in the two sectors, for convenience, we choose to work within the even sector, corresponding to $\sigma_z = 1$, $\tau_y = 1$ and $\sigma_z = -1$, $\tau_y = -1$. Choosing a convenient basis as described in Ref. [38]) σ_z becomes σ_x, σ_x becomes σ_y, and σ_y becomes σ_z. The reduced Hamiltonian is written as

$$\tilde{H}_{\tilde{M}_z=1} = \rho v k_x(\sigma_x \cos\alpha \ + \sigma_y \sin\alpha) + v k_y \sigma_z \,, \tag{4.2}$$

whose eigenvalues are

$$E = \pm v\sqrt{\rho^2 k_x^2 + k_y^2} \tag{4.3}$$

Notice that we could reduce the whole Hamiltonian to 2×2 form only because the system has the glide mirror symmetry $\tilde{M}_z$.

A magnetic exchange potential coupling to the out-of-plane spin can arise from a magnetic proximity effect and takes the form of a Zeeman term $\mathcal{B}_\mathcal{M}\sigma_z\tau_0$ in the Hamiltonian, where $\mathcal{B}_\mathcal{M}$ is the effective out-of-plane field arising from the exchange coupling. The glide mirror symmetry is preserved in the presence of this term. We can, therefore, still use the reduced Hamiltonian Eq. (4.2) under the glide mirror symmetry operator. To this end, we decouple this term for even and odd sectors (the same as we do for the Hamiltonian). We note that $\mathcal{B}_\mathcal{M}\tau_0\sigma_z$ can be reduced to $\mathcal{B}_\mathcal{M}\sigma_z$ in the even sector and $-\mathcal{B}_\mathcal{M}\sigma_z$ in the odd sector. Continuing to work in the even sector with the modified basis and also with the term added, we find

$$H'_{M_z=1} = (\rho v k_x \cos\alpha + \mathcal{B}_\mathcal{M})\sigma_x \ + \ \rho v k_x \sin\alpha\sigma_y \ + \ v k_y \sigma_z \,, \tag{4.4}$$

whose eigenvalues are

$$E = \pm v\sqrt{\left(\rho k_x + \frac{\mathcal{B}_\mathcal{M}}{v}\cos\alpha\right)^2 + k_y^2 + \frac{\mathcal{B}_\mathcal{M}^2}{v^2}\sin^2\alpha} \,. \tag{4.5}$$

The main qualitative effect of the exchange potential is the appearance of a gap in the excitation spectrum. We find the band gap using Eq. (4.5) as:

$$\Delta = 2\min|\bar{E}| = 2\mathcal{B}_\mathcal{M}\sin\alpha, \tag{4.6}$$

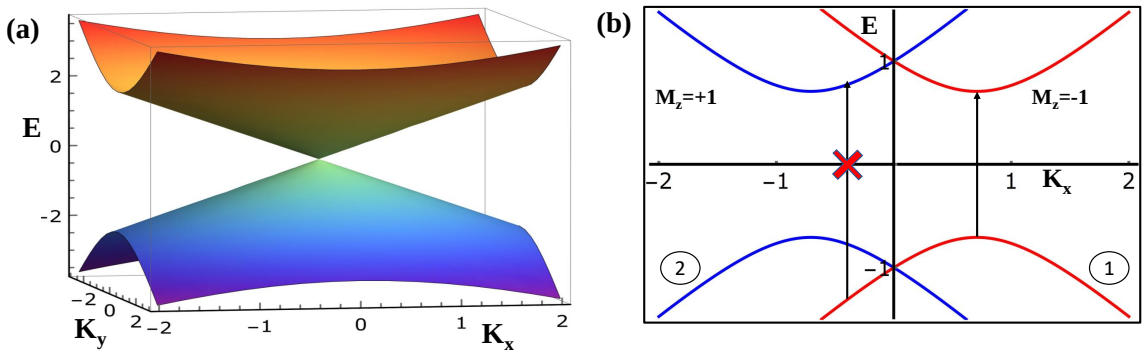

Figure 4.2: *(a) The band dispersion of α-Bi near the X_1 Dirac point.* ***(b)*** *This figure shows that only intra-valley transitions are possible as the two valleys hold opposite eigenvalues for $\tilde{M}_z$ when there is a gap present in the system.*

In practice, this gap is expected to be on the order of a few meV [41, 55, 56, 57, 58, 59, 60]. As anticipated, Eq. (4.6) offers a direct way to determine the mixing angle of our model from optical absorption experiments. The eigenfunctions for this Hamiltonian are

$$|\psi_{c\mathbf{k}}\rangle = \begin{pmatrix} \cos\frac{\theta}{2}\, e^{-i\gamma} \\ \sin\frac{\theta}{2} \end{pmatrix}; \quad |\psi_{v\mathbf{k}}\rangle = \begin{pmatrix} \sin\frac{\theta}{2}\, e^{-i\gamma} \\ -\cos\frac{\theta}{2} \end{pmatrix}, \tag{4.7}$$

with

$$\tan\gamma = \frac{\rho k_x \sin\alpha}{\rho k_x \cos\alpha + \frac{\mathcal{B}_{\mathcal{M}}}{v}}; \quad \tan\theta = \frac{\sqrt{(\rho k_x + \frac{\mathcal{B}_{\mathcal{M}}}{v}\cos\alpha)^2 + \frac{\mathcal{B}_{\mathcal{M}}^2}{v^2}\sin^2\alpha}}{k_y}, \tag{4.8}$$

which clearly depends on the effective Zeeman field $\mathcal{B}_{\mathcal{M}}$. To proceed with the study of optical properties, we need the current operators $\hat{j}_x$ and $\hat{j}_y$, which are obtained by taking the derivative of our Hamiltonian (Eq. (4.4)) with respect to k_x and k_y respectively, i.e., $\hat{\mathbf{j}} = \frac{\partial H}{\partial \mathbf{k}}$ with components

$$\hat{j}_x = \rho v\left(\cos\alpha\sigma_x + \sin\alpha\sigma_y\right), \quad \hat{j}_y = v\sigma_z\,. \tag{4.9}$$

These operators commute with the glide mirror operation $\tilde{M}_z$, which makes the transitions preserve the parity of $\tilde{M}_z$. Fig. 4.2(b) shows that the two valleys have opposite parity under the glide mirror symmetry; hence, inter-valley transitions are not allowed.

4.3 The transmission/reflection matrix

To treat effects like Faraday (Kerr) rotation for a single atomic layer, we need to compute the 2×2 matrices that connect the polarization state of the incoming light (a 2-dimensional complex vector in

the plane perpendicular to the direction of propagation of the light) to the polarization states of the transmitted and reflected light. (We assume here for simplicity that the incident, transmitted, and reflected light all travel along the z-axis perpendicular to the layer). In the standard treatment, these matrices are obtained by matching the electric fields on opposite sides of the layer, taking into account the two-dimensional electronic current that flows in the layer under the action of the electric field, causing the magnetic field to change discontinuously across the layer. In what follows, we will assume that the layer is much thinner than the wavelength of the light so that the thickness of the layer can be neglected, and positions immediately before and after the layer will be labeled by $z = 0^-$ and $z = 0^+$, respectively.

We work in the gauge where the scalar potential and the z component of the vector potential of the incoming electromagnetic wave vanish. The transverse components of the vector potential $\mathbf{A} = (A_x, A_y)$ satisfy the Maxwell equation (in Gaussian units)

$$-\partial_z^2 \mathbf{A}(z) - \frac{\omega^2}{c^2}\mathbf{A}(z) = \frac{4\pi}{c}\mathbf{J}(z)\,, \tag{4.10}$$

where ω is the wave's frequency and $\mathbf{J}(z)$ is the three-dimensional current density, concentrated in an infinitesimal region around $z = 0$. We define the two-dimensional current density in the layer as

$$\mathbf{j} = \int dz \mathbf{J}(z)\,, \tag{4.11}$$

where the integral over z, while formally extending to infinity, converges within a small vanishing region corresponding to the thickness of the layer. The two-dimensional current density $\mathbf{j}$ is related to the electric field by the frequency-dependent electrical conductivity tensor $\boldsymbol{\sigma}(\omega)$:

$$\mathbf{j} = \boldsymbol{\sigma}(\omega) \cdot \mathbf{E}\,. \tag{4.12}$$

The electric and magnetic field are given respectively by $\mathbf{E} = \frac{i\omega}{c}\mathbf{A}$ and $\mathcal{H} = \hat{\mathbf{z}} \times \mathbf{A}'$ where $\mathbf{A}'$ is the derivative of $\mathbf{A}$ with respect to z.

Integrating Eq. (4.10) over z from $z = -\epsilon$ to $z = +\epsilon$, with ϵ tending to zero we obtain:

$$\delta\mathbf{A}' \equiv -\mathbf{A}'|_{-\epsilon}^{\epsilon} = \frac{4\pi}{c}\mathbf{j} = \boldsymbol{\sigma} \cdot \mathbf{E}\,. \tag{4.13}$$

This tells us that $\mathcal{H}$ "jumps" across the layer. At the same time, the vector potential itself (and

hence the electric field) is continuous across the layer, i.e.,

$$\delta\mathbf{A} \equiv \mathbf{A}(\epsilon) - \mathbf{A}(-\epsilon) = 0\,. \tag{4.14}$$

We seek a solution to the form

$$\mathbf{A}(z) \propto \begin{cases} \mathbf{e}_i e^{ikz} + \mathbf{R}\cdot\mathbf{e}_i e^{-ikz}, & z < 0 \\ \mathbf{T}\cdot\mathbf{e}_i e^{ikz}\,, & z > 0 \end{cases} \tag{4.15}$$

where $\mathbf{e}_i$ is a two-dimensional complex vector describing the state of polarization of the incident polarization of the incoming wave in the (x, y) plane, $\mathbf{R}$ and $\mathbf{T}$ are the reflection, and the transmission matrices – 2×2 complex matrices acting on the polarization. Imposing the boundary conditions (4.13) and (4.14) we find

$$\mathbf{T} = (1 + a.\boldsymbol{\sigma})^{-1}\,, \tag{4.16}$$

$$\mathbf{R} = \mathbf{T} - \mathbf{1} = a\boldsymbol{\sigma}\cdot(1 + a.\boldsymbol{\sigma})^{-1}\,, \tag{4.17}$$

where we have defined $a \equiv \frac{2\pi}{c}$. As previously mentioned, the transmission matrix ($\mathbf{T}$), acting on the incoming polarization vector ($\mathbf{e}_i$), gives the polarization of the transmitted light $\mathbf{e}_t$ and similarly, the reflection matrix ($\mathbf{R}$) gives the polarization of the reflected light $\mathbf{e}_r$.

$$\mathbf{e}_t = \mathbf{T}\cdot\mathbf{e}_i; \quad \mathbf{e}_r = \mathbf{R}\cdot\mathbf{e}_i \tag{4.18}$$

Now that we have established the relation between the transmission/reflection matrices and the conductivity tensor, we will calculate the latter.

4.4 Calculation of the conductivity tensor

In this section, we calculate the conductivity tensor using linear response theory, as described in Ref. ([63]). The conductivity tensor for our model system is given by

$$\sigma_{\alpha\beta}(\omega) = \frac{ie^2}{\omega}\chi_{j_\alpha j_\beta}(\omega)\,, \tag{4.19}$$

where $\chi_{j_\alpha j_\beta}$ is the current-current response function

$$\chi_{j_\alpha j_\beta}(\omega) = \sum_{\mathbf{k}} \left\{ \frac{\langle \psi_{c\mathbf{k}} | \hat{j}_\alpha | \psi_{v\mathbf{k}} \rangle \langle \psi_{v\mathbf{k}} | \hat{j}_\beta | \psi_{c\mathbf{k}} \rangle}{\omega - \omega_{cv}(\mathbf{k}) + i\eta} - \frac{\langle \psi_{c\mathbf{k}} | \hat{j}_\beta | \psi_{v\mathbf{k}} \rangle \langle \psi_{v\mathbf{k}} | \hat{j}_\alpha | \psi_{c\mathbf{k}} \rangle}{\omega + \omega_{cv}(\mathbf{k}) + i\eta} \right\} , \tag{4.20}$$

where $\psi_{c\mathbf{k}}$ and $\psi_{v\mathbf{k}}$ are the Bloch states of the conduction and valence band, respectively, and $\omega_{cv}(\mathbf{k})$ is the difference of their energies. η is an infinitesimal positive real number. The operators $\hat{j}_\alpha$ are defined in Eq. (4.9). We notice that the "diamagnetic" contribution to the conductivity [63] is absent because our model Hamiltonian is linear in $\mathbf{k}$.

In the next two subsections, we treat this tensor's off-diagonal and diagonal components separately.

4.4.1 Off-diagonal component of the conductivity tensor (σ_{xy})

We calculate the off-diagonal component of the conductivity tensor first. We separately consider the imaginary and the real parts of the response function $\chi_{j_x j_y}$. For the imaginary part, we find (in the limit $\eta \to 0$)

$$\chi''_{j_x j_y} = 2\rho v^2 \sum_k \frac{2\omega}{\omega^2 - \omega_{cv}^2(\mathbf{k})} \frac{\mathcal{B}_{\mathcal{M}} \sin\alpha}{E(\mathbf{k})} , \tag{4.21}$$

where the integral over $\mathbf{k}$ is done according to the Cauchy principal value prescription. This is different from zero both below ($|\omega| \leq \Delta$) and above the gap ($|\omega| \geq \Delta$). For the real part of $\chi_{j_x j_y}$ we find

$$\chi'_{j_x j_y} = 2\pi\rho v^2 \sum_{\mathbf{k}} \frac{\mathcal{B}_{\mathcal{M}} \sin\alpha}{E(\mathbf{k})} \left[\delta(\omega - \omega_{cv}(\mathbf{k})) + \delta(\omega + \omega_{cv}(\mathbf{k})) \right] , \tag{4.22}$$

which differs from zero only above the gap, i.e., for $|\omega| > \Delta$. In writing these expressions, we have included a factor 2 arising from the double degeneracy of the energy eigenvalues associated with glide-mirror parities $\tilde{M}_z = 1$ and $\tilde{M}_z = -1$ (see discussion before Eq. (4.4)). Then, making use of Eq. (4.19) we obtain the real part of the off-diagonal conductivity

$$\sigma'_{xy}(\omega) = -\frac{e^2}{2\pi\hbar} \frac{\Delta}{\omega} \log \left| \frac{\Delta - \omega}{\Delta + \omega} \right| \text{ (Here reinstating the } \hbar \text{ to match dimension)} . \tag{4.23}$$

This expression shows that the Hall conductivity has logarithmic divergence when ω approaches the gap frequency Δ. Similarly, the imaginary part of the off-diagonal conductivity is given by

$$\sigma''_{xy} = \frac{e^2}{4\hbar} \frac{\Delta}{\omega} \Theta(|\omega| - \Delta) , \tag{4.24}$$

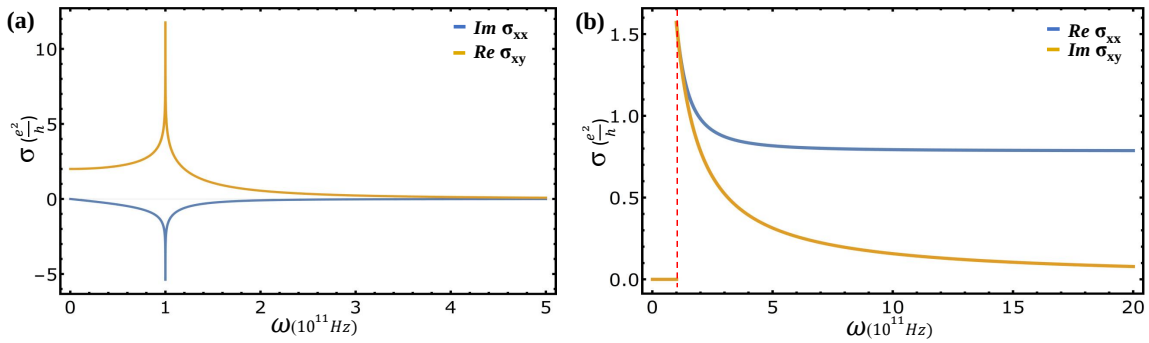

Figure 4.3: ***(a)*** *Plots of σ'_{xy} and σ''_{xx} vs ω. Both exhibit a logarithmic singularity at the absorption edge $\omega = \Delta$ ($\Delta = 2\mathcal{B}_{\mathcal{M}} \sin\alpha = 1$ in this plot); however, the divergence in σ'_{xy} has a stronger prefactor. Notice that σ'_{xy} has a finite value ($2\frac{e^2}{h}$) at zero frequency, whereas σ''_{xx} vanishes.* ***(b)*** *Plots of σ''_{xy} and σ'_{xx} vs ω. These functions vanish for frequencies below the gap. The red dashed line marks the absorption edge.*

where $\Theta(x)$ is the Heaviside step function $\Theta(x) = 1$ for $x > 0$ and $\Theta(x) = 0$ for $x < 0$. Notice that σ_{xy} vanishes for $\mathcal{B}_{\mathcal{M}} = 0$, leaving the system with only diagonal components of the conductivity in the absence of $\mathcal{B}_{\mathcal{M}}$.

4.4.2 Diagonal components of the conductivity tensor (σ_{xx}, σ_{yy})

Following the same procedures as in the previous section, we obtain the following formulas for the real and imaginary parts of the diagonal response functions $\chi_{j_x j_x}$ and $\chi_{j_y j_y}$:

$$\chi'_{j_x j_x}(\omega) = 2\rho^2 v^2 \sum_{\mathbf{k}} \frac{2\omega_{cv}(\mathbf{k})}{\omega^2 - \omega_{cv}^2(\mathbf{k})} \left(\frac{k^2 \sin^2\phi(\mathbf{k}) + \mathcal{B}_{\mathcal{M}}^2 \sin^2\alpha}{E^2(\mathbf{k})} \right); \quad \chi'_{j_y j_y}(\omega) = \frac{\chi'_{j_x j_x}(\omega)}{\rho^2} \,. \tag{4.25}$$

and

$$\chi''_{j_x j_x}(\omega) = -2\pi\rho^2 v^2 \sum_{\mathbf{k}} \left[\delta(\omega - \omega_{cv}(\mathbf{k})) - \delta(\omega + \omega_{cv}(\mathbf{k}))\right] \left(\frac{k^2 \sin^2\phi(\mathbf{k}) + \mathcal{B}_{\mathcal{M}}^2 \sin^2\alpha}{E^2(\mathbf{k})} \right). \tag{4.26}$$

where $\phi(\mathbf{k}) = \arctan\left(\frac{k_y}{\rho k_x + \frac{\mathcal{B}_{\mathcal{M}}}{v}\cos\alpha} \right)$ and $\chi''_{j_y j_y} = \chi''_{j_x j_x}/\rho^2$. Using Eq. (4.19), we can conclude that the imaginary and real parts of the conductivity are given by

$$\sigma''_{xx}(\omega) = \frac{\rho e^2}{4\pi\hbar} \left[\frac{\Delta}{\omega} + \frac{(\Delta^2 + \omega^2)}{2\omega^2} \log\left| \frac{\Delta - \omega}{\Delta + \omega} \right| \right] \; ; \quad \sigma''_{yy}(\omega) = \frac{\sigma''_{xx}(\omega)}{\rho^2} \,, \tag{4.27}$$

and

$$\sigma'_{xx}(\omega) = \frac{\rho e^2}{8\hbar} \left[1 + \frac{\Delta^2}{\omega^2} \right] \Theta(|\omega| - \Delta); \quad \sigma'_{yy}(\omega) = \frac{\sigma'_{xx}(\omega)}{\rho^2} \,. \tag{4.28}$$

The anisotropy parameter ρ is the ratio between the velocities in the x and y-directions and reduces to 1 in the isotropic case.

4.5 Calculation of the Faraday and Kerr rotation angles

From Eq. (4.16) we see that the transmission matrix is given by

$$\mathbf{T} = \frac{1}{N}\begin{pmatrix} 1+a\sigma_{yy} & -a\sigma_{xy} \\ -a\sigma_{yx} & 1+a\sigma_{xx} \end{pmatrix}, \tag{4.29}$$

where $\sigma_{xy} = -\sigma_{yx}$ and

$$N = (1+a\sigma_{xx})(1+a\sigma_{yy}) + (a\sigma_{xy})^2 \tag{4.30}$$

On the other hand, from Eq. (4.17), we find that the components of the reflection matrix are given by

$$\mathbf{R} = \begin{pmatrix} T_{xx}-1 & T_{xy} \\ T_{yx} & T_{yy}-1 \end{pmatrix}, \tag{4.31}$$

From these formulas, we now proceed to extract the Faraday and Kerr rotation angles.

4.5.1 Isotropic system

For the isotropic system we have $\sigma_{xx} = \sigma_{yy}$ ($\rho = 1$) which leads to $T_{xx} = T_{yy}$. In this case, it is easy to see that the states of circular polarization are eigenstates of the transmission and reflection matrix, meaning that these states of polarization are not changed upon transmission or reflection but suffer a phase shift.

The Faraday and Kerr rotation angles are defined as half of the difference between the phase shifts of the left circular polarized (LCP) wave and the right circular polarized (RCP) waves in the transmitted and reflected wave, respectively [49, 50, 64]:

$$\theta_F = \frac{1}{2}Arg\left[\frac{E^t_{LCP}}{E^t_{RCP}}\right]; \qquad \theta_K = \frac{1}{2}Arg\left[\frac{E^r_{LCP}}{E^r_{RCP}}\right]. \tag{4.32}$$

The x and y components of the electric field are related to the LCP and RCP components as follows:

$$\begin{pmatrix} E_x \\ E_y \end{pmatrix} = \frac{1}{\sqrt{2}}\begin{pmatrix} 1 & 1 \\ -i & i \end{pmatrix}\begin{pmatrix} E_{LCP} \\ E_{RCP} \end{pmatrix} \tag{4.33}$$

Substituting this in the equations that relate the transmitted and reflected fields to the incident field[1], namely,

$$\begin{pmatrix} E_x^t \\ E_y^t \end{pmatrix} = \begin{pmatrix} T_{xx} \\ T_{yx} \end{pmatrix} E_x^i; \quad \begin{pmatrix} E_x^r \\ E_y^r \end{pmatrix} = \begin{pmatrix} R_{xx} \\ R_{yx} \end{pmatrix} E_x^i \ . \tag{4.34}$$

we easily find

$$\theta_F = \frac{1}{2} Arg \left[\frac{T_{xx} + iT_{xy}}{T_{xx} - iT_{xy}} \right] = \frac{1}{2} Arg \left[\frac{1 + a\sigma_{xx} + ia\sigma_{xy}}{1 + a\sigma_{xx} - ia\sigma_{xy}} \right] \ , \tag{4.35}$$

and

$$\theta_K = \frac{1}{2} Arg \left[\frac{R_{xx} + iR_{xy}}{R_{xx} - iR_{xy}} \right] = \frac{1}{2} Arg \left[\frac{\sigma_{xx} - i\sigma_{xy}}{\sigma_{xx} + i\sigma_{xy}} \frac{1 + a(\sigma_{xx} + i\sigma_{xy})}{1 + a(\sigma_{xx} - i\sigma_{xy})} \right] . \tag{4.36}$$

At zero frequency, the Hall conductivity has a nonzero value ($\sigma_{xy}(0) = 2\frac{e^2}{h}$), but the longitudinal one is zero. This results in a nonzero Faraday rotation angle at zero frequency:

$$\theta_F(0) = \frac{1}{2} Arg \left[\frac{1 - ia\sigma_{xy}(0)}{1 + ia\sigma_{xy}(0)} \right] = \frac{1}{2} Arg \left[\frac{1 - 2i\alpha_F}{1 + 2i\alpha_F} \right] = 2\alpha_F \, , \tag{4.37}$$

where $\alpha_F = \frac{e^2}{\hbar c}$ is the fine structure constant. Plotting the Faraday angle as a function of frequency, we see that, similar to the conductivities, it has a sharp rise at the absorption edge. Still, instead of diverging, it reaches a maximum theoretical value $\frac{\pi}{2}$. More precisely, when we choose the frequency very near to the absorption edge, we find that

$$\theta_F(\omega \sim \Delta) \approx \frac{1}{2} Arg \left[\frac{a\sigma_{yy} - ia\sigma_{xy}}{a\sigma_{yy} + ia\sigma_{xy}} \right] \approx \frac{1}{2} Arg \left[\frac{-ia\sigma_{xy}}{+ia\sigma_{xy}} \right] = \frac{\pi}{2} \, , \tag{4.38}$$

where the second approximate equality follows from the fact that the logarithmic divergence of $\sigma_{xy}(\omega)$ for $\omega \to \Delta$ has a larger prefactor compared to the logarithmic divergence of $\sigma_{xx}(\omega)$. The range of frequencies around $\omega = \Delta$ in which the Faraday angle would be close to the theoretical limit $\frac{\pi}{2}$ is exponentially small ($\simeq e^{-1/\alpha_F}$) and unobservable in practice. Nevertheless, an order of magnitude increase in θ_F is visible in Fig. 4.4(b). While the peak value of θ_F is a far cry from $\pi/2$, it is still more significant than any value previously measured near the absorption edge for two-dimensional systems [64, 65].

A similar analysis can be done for the Kerr rotation angle. From Eq. (4.36), we see that in the low-frequency regime, the Kerr rotation angle is $\theta_K \approx \frac{\pi}{2}$. This large value describes that left and right circularly polarized waves are reflected with amplitudes of opposite signs, corresponding to a phase difference of π. In Fig. 4.4(c), it can be seen that this value remains constant below the

[1] Considering we have the incident wave linearly polarized along the x-direction.

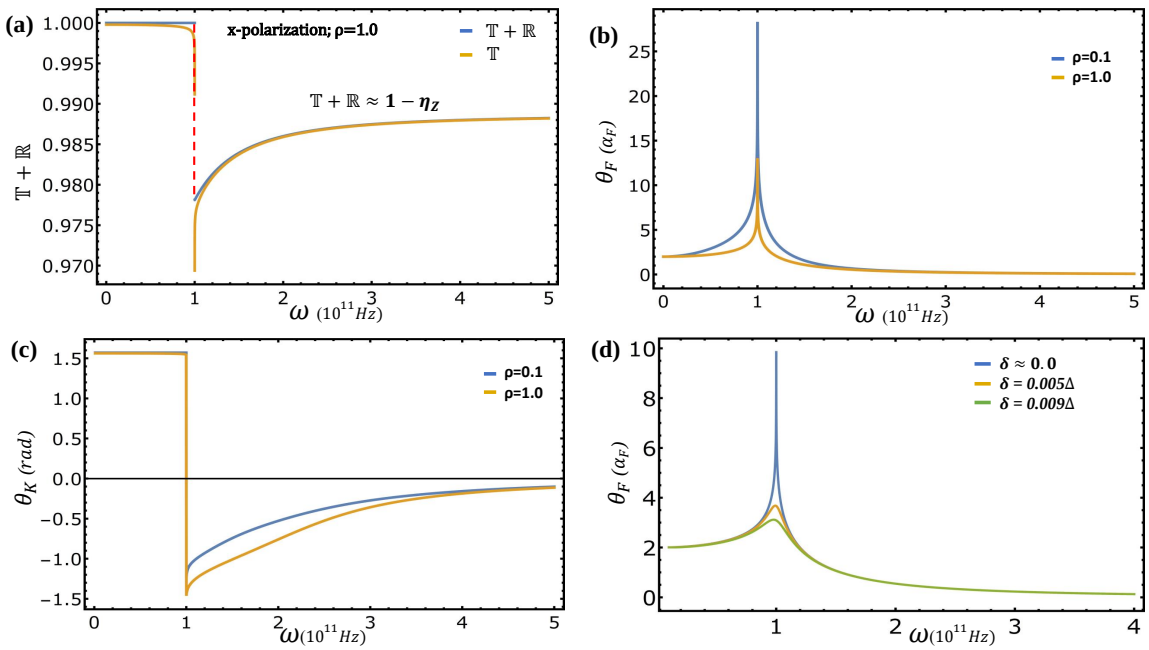

Figure 4.4: ***(a)*** *Plot of transmittance and transmittance+reflectance vs frequency in units of* $\Delta = 10^{11}$ *Hz. Notice that transmittance and reflectance add to* 1 *below the absorption edge, marked by the vertical red dashed line. The value of the reflectance can be inferred from the small difference between these two plots. Above the absorption edge, the sum* $\mathbb{T} + \mathbb{R}$ *is less than* 1 *due to the optical absorption.* ***(b)*** *Faraday rotation angle vs frequency. The orange line is for the isotropic case (*$\rho = 1.0$*), and the blue line is for the anisotropic case (*$\rho = 0.1$*) calculated as described in Section VB. I Notice that the same zero-frequency value (*α_F*) is independent of the anisotropy parameter* ρ*. The enhancement of the Faraday rotation angle at the absorption threshold is much larger in the anisotropic case.* ***(c)*** *Kerr rotation angle vs frequency. The orange and blue lines are for* $\rho = 1$ *and* $\rho = 0.1$*, respectively.* ***(d)*** *The effect of disorder broadening (*$\delta = 1/\tau$*) on the Faraday rotation angle, calculated by the procedure described in Section VI.*

absorption edge, but it reverses its sign as the frequency crosses the absorption edge.

As a final point, in Fig. 4.4(a) we plot the transmittance $\mathbb{T}$ and the reflectance $\mathbb{R}$ defined as follows[64]:

$$\mathbb{T} = \frac{1}{2}\left(|T_{LCP}|^2 + |T_{RCP}|^2\right); \quad \mathbb{R} = \frac{1}{2}\left(|R_{LCP}|^2 + |R_{RCP}|^2\right). \tag{4.39}$$

Below the absorption edge, we verify that we have $\mathbb{T} + \mathbb{R} = 1$, in accordance with the fact that there is no absorption of energy in this frequency range. Above the absorption edge, on the other hand, we find $\mathbb{T} + \mathbb{R} < 1$, where the difference refers to the existence of absorption above the gap. In our recent study (Ref. [38]), we have shown when there is a gap present in this system, it will give rise to significant absorption above the gap, and this is just another confirmation of the same.

4.5.2 Anisotropic system

The calculation of the Faraday angle for an anisotropic system presents us with some basic difficulties. The right and left circularly polarized states are no longer eigenstates of the transmission

and reflection matrix: rather, an incident LCP wave will acquire an RCP component upon transmission/reflection, and similarly, an incident RCP wave will acquire an LCP component. If, on the other hand, we start with a linearly polarized incident wave, then the transmitted/reflected waves will not be in a state of linear polarization, having acquired elliptic components. It is still possible to define a rotation angle, as discussed in Appendix A. Still, this rotation angle will then depend on the orientation of the incident linear polarization with respect to the crystallographic axes.

In this section, we adopt a practical definition of the Faraday and Kerr rotation angles, which avoids these difficulties and yields values independent of the state of polarization of the incident wave. The idea is to generalize the definition we used in the isotropic case and define the magneto-optical rotation angles as half the difference of the phase shifts associated with the exact eigenstates of the transmission and reflection matrices.

To do this, we will diagonalize the transmission matrix first. In the chiral basis [2] this matrix has the following structure

$$\tilde{\mathbf{T}} = U^\dagger \cdot \begin{pmatrix} T_{xx} & T_{xy} \\ -T_{xy} & T_{yy} \end{pmatrix} \cdot U = \begin{pmatrix} \bar{T} + iT_{xy} & \Delta T \\ \Delta T & \bar{T} - iT_{xy} \end{pmatrix} \tag{4.40}$$

where

$$\bar{T} \equiv \frac{T_{xx} + T_{yy}}{2}\,, \quad \Delta T \equiv \frac{T_{xx} - T_{yy}}{2}\,. \tag{4.41}$$

Its eigenvalues can be written as

$$T_\pm = \bar{T} \pm i\sqrt{T_{xy}^2 - \Delta T^2}; \tag{4.42}$$

Similarly, the eigenvalues of the reflection matrix are given by

$$R_\pm = \bar{R} \pm i\sqrt{R_{xy}^2 - \Delta R^2}; \tag{4.43}$$

In terms of T_+ and T_-, the Faraday rotation angle is expressed as

$$\theta_F \equiv \frac{1}{2} Arg\left[\frac{T_+}{T_-}\right] = \frac{1}{2} Arg\left[\frac{\bar{T} + i\sqrt{T_{xy}^2 - \Delta T^2}}{\bar{T} - i\sqrt{T_{xy}^2 - \Delta T^2}}\right]\,, \tag{4.44}$$

[2] The chiral basis states are related to the $x-y$ basis states by the unitary transformation $U = \frac{1}{\sqrt{2}}\begin{pmatrix} 1 & 1 \\ i & -i \end{pmatrix}$, $U^\dagger = \frac{1}{\sqrt{2}}\begin{pmatrix} 1 & -i \\ 1 & i \end{pmatrix}$. We then have $\tilde{v} = U^\dagger v$ where v is the representative of a state in the $x-y$ basis and $\tilde{v}$ is the representative of the same state in the chiral basis.

In terms of the conductivities, this becomes

$$\theta_F = \frac{1}{2} Arg \left[\frac{2 + a\tilde{\sigma}_{xx}\left(\rho + \rho^{-1}\right) + ia\sqrt{4\sigma_{xy}^2 - \tilde{\sigma}_{xx}^2\left(\rho - \rho^{-1}\right)^2}}{2 + a\tilde{\sigma}_{xx}\left(\rho + \rho^{-1}\right) - ia\sqrt{4\sigma_{xy}^2 - \tilde{\sigma}_{xx}^2\left(\rho - \rho^{-1}\right)^2}} \right] , \tag{4.45}$$

where $\tilde{\sigma}_{xx} \equiv \frac{\sigma_{xx}}{\rho}$. The corresponding expression for the Kerr rotation angle is

$$\theta_K = \frac{1}{2} Arg \left[\frac{a\tilde{\sigma}_{xx}\left(\rho + \rho^{-1}\right) + ia\sqrt{4\sigma_{xy}^2 - \tilde{\sigma}_{xx}^2\left(\rho - \rho^{-1}\right)^2}}{a\tilde{\sigma}_{xx}\left(\rho + \rho^{-1}\right) - ia\sqrt{4\sigma_{xy}^2 - \tilde{\sigma}_{xx}^2\left(\rho - \rho^{-1}\right)^2}} \right] \tag{4.46}$$

where we have omitted a negligible second order term $2a^2\left(\tilde{\sigma}_{xx}\tilde{\sigma}_{yy} + \tilde{\sigma}_{xy}^2\right)$.

In Fig. 4.4(b) and (c), we compare the Faraday and Kerr rotation angles calculated for the isotropic case ($\rho = 1$, orange line) and the strongly anisotropic case ($\rho = 0.1$, blue line). The two plots are qualitatively similar, and their low-frequency limits do not depend on the anisotropy parameter ρ. However, the anisotropy results in a sharper enhancement of the Faraday rotation angle at the absorption edge, whereas the Kerr rotation angle is reduced.

A more complete discussion of the Faraday and Kerr rotation angles in an anisotropic system is provided in Appendix B.1.

4.6 Disorder broadening

Our calculations thus far have been done with the assumption that momentum is strictly conserved, i.e., there is no impurity scattering. A simple, although nonrigorous way, to take into account the effect of a finite momentum relaxation time τ is to replace the infinitesimal η in Eq. (4.20) by the finite quantity $\delta = 1/\tau$. This is expected to be qualitatively correct as long as δ remains much smaller than the gap Δ. With this modification, the conductivity is calculated straightforwardly and works out to be

$$\sigma_{xy}(\omega) = -\frac{e^2}{4\pi\hbar}\frac{\Delta}{\omega}\log\frac{\omega' - \Delta}{\omega' + \Delta} \quad ; \tag{4.47}$$

$$\sigma_{xx}(\omega) = \frac{i\rho e^2}{8\pi\hbar\omega}\left[\Delta + \frac{(\omega'^2 + \Delta^2)}{2\omega'}\ \log\frac{\omega' - \Delta}{\omega' + \Delta}\right] , \tag{4.48}$$

where $\omega' \equiv \omega + i\delta$ and log is understood to denote the complex logarithm. From the expression of the conductivities above, we can see that the logarithmic divergence is not present anymore. Instead, we have a function that has a finite peak at the absorption edge. The Faraday rotation angle is still

given by Eq. (4.35), and it is plotted in Fig. 4.4(d). We see that with increasing disorder, the curve is broadened, and the peak value is decreased. A significant enhancement of θ_F can still be observed if the system is sufficiently pure.

4.7 Conclusion

We have performed a detailed theoretical analysis of the Faraday and Kerr rotation for a generic model of gapped nonsymmorphic 2D semimetals. Both the gap and the required breaking of time-reversal symmetry are caused by a Zeeman term coupling with the out-of-plane component of the spin. The Zeeman coupling could be generated by a real magnetic field, but such a field would also couple to the orbital motion of the electrons in the plane. This is not the case for our model as it depends on the exchange interaction with a magnetic dopant or proximal magnetization – the so-called proximity effect. This gives rise to an "effective Zeeman coupling," which, being of Coulombic origin, does not have the drawback of coupling to the orbital motion of the electrons in the same way that a real magnetic field does [50, 58].

First, we matched Maxwell's equation for either side of the 2D layer to express the transmission and reflection matrices in terms of the conductivity matrix of the layer. We calculated the frequency-dependent conductivity and finally computed the Faraday and Kerr rotation angles. We also observed the appearance of an elliptic component of the polarization, which inevitably accompanies the Faraday or the Kerr rotation when linearly polarized light is transmitted or reflected by the layer.

The Faraday rotation angle has a sharp peak at the absorption edge, which results in order of magnitude enhancement relative to its zero-frequency value. We also find a giant Kerr rotation ($\approx \pi/2$) in the low-frequency region which abruptly changes signs just above the absorption edge. The anisotropy of the system, parameterized by $\rho < 1$, does not change these qualitative features but leads to an even sharper enhancement of the Faraday rotation angle at the absorption edge. We also calculated the effect of a finite momentum relaxation time on the Faraday rotation angle due to disorder. Not surprisingly, the peak becomes broader and weaker with increasing disorder.

We propose that the dependence of the polarization rotation and the ellipticity on the incident angle, as shown, and the variation of their magnitudes with changing frequency, can be used to study the optical properties of nonsymmorphic 2D Dirac semimetals experimentally in the presence of a gap-inducing effective Zeeman field. The giant peak value in Faraday and Kerr rotation angles enabled by the band anisotropy and the field suggests that these materials can be useful platforms for optoelectronic and magnetoelectronic device applications.

Chapter 5

INSULATOR-METAL TRANSITION AND MAGNETIC CROSSOVER IN BILAYER GRAPHENE

5.1 Introduction.

The effects of perpendicular magnetic fields on the electronic properties of monolayer graphene have been studied in a variety of contexts over the years. Landau levels[66], integer [67] and fractional[68] quantum Hall effects were demonstrated experimentally within several years of graphene discovery[2]. Very recently, a giant magnetoresistance of Dirac electrons in high-mobility graphene has been discovered [69]. In addition, it has been shown that the orbital magnetic response of graphene can be controlled by modifying the number of charge carriers via gating. Perfect diamagnetism at the charge neutrality point [70] is superseded by paramagnetism as the Fermi level approaches a van Hove singularity in the density of states [71] making it possible to switch the monolayer between diamagnetic and paramagnetic regimes[72]. All of these effects have been experimentally observed [73] and thoroughly investigated theoretically [74, 75, 76].

In recent years, bilayer and multilayer graphene have garnered significant attention following the discovery of flat bands in twisted bilayer graphene that host superconductivity [77]. These structures are also remarkable for their orbital magnetic properties [74, 78]. A key feature of multilayer structures is their sensitivity to in-plane magnetic fields, which are coupled to the in-plane component of the orbital magnetic moment due to the looping motion of the electron between layers [79, 80, 81, 82, 83]. In a bilayer system, for instance, the vector potential associated with the in-plane magnetic field can have opposite signs in the two layers, while remaining constant in each layer. This causes the band structures of the layers (before turning on interlayer coupling) to shift in opposite directions in momentum space, leading to non-trivial modifications of the band structure when interlayer

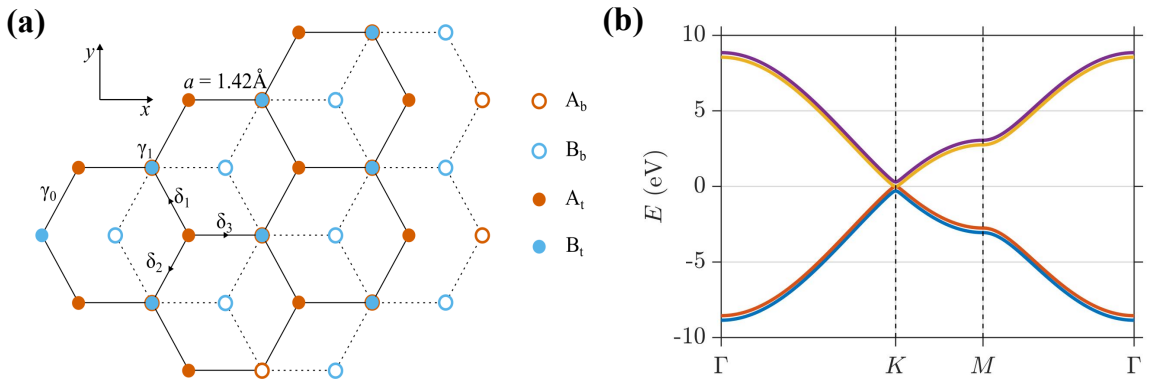

Figure 5.1: *Bernal-stacked graphene bilayer. In this stacking configuration, the coupling is between the $B_t \to A_b$. The three hopping directions are marked as δ with their usual definition. Electronic spectrum for AB stacking BLG, along the k-space trajectory $\Gamma - K - M - \Gamma$. We set $t_\perp = 0.3eV$.*

coupling is considered. This effect was experimentally demonstrated a few years ago in twisted bilayer graphene, where an in-plane magnetic field was used to alter the separation of nearby Dirac cones[84].

However, despite this pioneering work, the potential of in-plane magnetic fields as a tool for band-structure manipulation remains largely unexplored. In particular, no attention has been paid to the possibilities opened by the interplay between an in-plane magnetic field and an electric field perpendicular to the layer, the latter being commonly used as a tool to change the band gap [85, 86].

This paper aims to describe some of these possibilities. We focus, for clarity, on the simplest model of a non-twisted, Bernal-stacked graphene bilayer [12, 87, 88, 89] and show that it can be driven through a transition from a gapped insulator to a compensated semimetal by the application of a very strong in-plane magnetic field combined with a vertical displacement field. This phenomenon is just an example of the kind of control that can be exerted on the properties of bilayer graphene by means of crossed magnetic and electric fields: the magnetic field controls the k-space separation of the Dirac cones arising from each layer, while the electric field controls their displacement along the energy axis.

Second, we show that an even richer scenario emerges when we consider the orbital magnetic response to an in-plane magnetic field as a function of doping and electric bias. We find that the in-plane orbital magnetic susceptibility (OMS) switches from diamagnetic to paramagnetic concomitantly with the field-induced IM transition at half-filling. Moving away from half-filling we find that the in-plane magnetic response can be switched from diamagnetic to paramagnetic by adjusting the displacement field and the position of the chemical potential within the bands. We also demonstrate a clear correlation between the amplitude of the fluctuations of the in-plane magnetic moment and the magnitude of the paramagnetic response Appendix C.3.

Taken together, our findings reveal an unexpected and hitherto unnoticed interplay between electronic transport and in-plane magnetism in layered electronic systems. Crucially, this interplay can be controlled by modest displacement fields on the order of 100 meV, even though the value of the in-plane magnetic field required to achieve sizeable effects – while formally proportional to the interlayer coupling – is unrealistically high ($\sim$ 1000 T for bilayer graphene). To remedy this, we propose several strategies for applying the controlling fields to artificially strained and/or twisted multilayer structures. These structures are indeed considered most promising for band structure engineering, which targets desired physical properties. With Brillouin zones up to 100 times smaller than the "natural" ones, these artificial structures should exhibit the predicted effects at much smaller values of the in-plane field – as low as 10 T.

5.2 Model

Monolayer graphene features a honeycomb arrangement of carbon atoms, which can be interpreted as a triangular Bravais lattice containing two atoms within each primitive unit cell. The basis vectors for this lattice are defined as

$$\mathbf{a}_1 = \frac{a}{2}(3, \sqrt{3}), \quad \mathbf{a}_2 = \frac{a}{2}(3, -\sqrt{3}), \tag{5.1}$$

where the parameter $a \approx 1.42\,\text{Å}$ denotes the interatomic distance between neighboring carbon atoms. The associated vectors in reciprocal space are

$$\mathbf{b}_1 = \frac{2\pi}{3a}(1, \sqrt{3}), \quad \mathbf{b}_2 = \frac{2\pi}{3a}(1, -\sqrt{3}). \tag{5.2}$$

Central to understanding graphene's electronic behavior are the momentum-space locations known as the K and K' points, situated at the vertices of the Brillouin zone. These are referred to as Dirac points, with their specific coordinates given by

$$K = \left(\frac{2\pi}{3a}, \frac{2\pi}{3\sqrt{3}a}\right), \quad K' = \left(\frac{2\pi}{3a}, -\frac{2\pi}{3\sqrt{3}a}\right). \tag{5.3}$$

The Bernal-stacked graphene bilayer is described by a tight-binding Hamiltonian with nearest-

neighbor intra- and interlayer hopping [87]

$$H_{\mathbf{k}} = \begin{pmatrix} V & \gamma_0 f(\mathbf{k}_\mathrm{t}) & 0 & 0 \\ \gamma_0 f^\dagger(\mathbf{k}_\mathrm{t}) & V & \gamma_1 & 0 \\ 0 & \gamma_1 & -V & \gamma_0 f(\mathbf{k}_\mathrm{b}) \\ 0 & 0 & \gamma_0 f^\dagger(\mathbf{k}_\mathrm{b}) & -V \end{pmatrix} \tag{5.4}$$

The four basis states are $\mathrm{A_t}$, $\mathrm{B_t}$, $\mathrm{A_b}$, and $\mathrm{B_b}$ with A and B denoting the sublattice and t/b subscripts identifying the top and bottom layers. The hopping energy between $\mathrm{B_t}$ and $\mathrm{A_b}$ is $\gamma_1 = 0.3$eV, while the hopping term between the nearest neighbors within a layer is $\gamma_0 = -2.8$eV [12]. $f(\mathbf{k}) = \sum_{n=1}^{3} e^{i\mathbf{k}\cdot\boldsymbol{\delta}_n}$, where $\boldsymbol{\delta}_1 = a(-1, \sqrt{3})/2$, $\boldsymbol{\delta}_2 = a(-1, -\sqrt{3})/2$, and $\boldsymbol{\delta}_3 = a(1, 0)$ are the vectors connecting atoms A to their nearest neighbors within a layer. The function $f(k)$ describing nearest neighbour hopping, with the information of the hopping directions is given by

$$f(k) = e^{ik_x a} + 2e^{-ik_x a/2} cos(\sqrt{3}k_y a/2) \tag{5.5}$$

The diagonal terms $\pm V$ originate from an external electric field applied perpendicular to the bilayer (the displacement field). Finally, the constant vector potential is incorporated into the Hamiltonian by using the Peierls substitution $\mathbf{k} \to \mathbf{k} \pm e\mathbf{A}/\hbar$, so that we have

$$\mathbf{k}_{\mathrm{t/b}} a = \mathbf{k} a \pm \pi\Phi(\sin\theta, -\cos\theta, 0)\,, \tag{5.6}$$

where l is the interlayer separation and $\Phi = Bal/\Phi_0$ is the magnetic flux through a rectangle defined by an intra-plane bond and an inter-plane segment in units of the magnetic flux quantum $\Phi_0 = h/e \simeq 4.14 \times 10^5$ T.Å^2. Here $\theta = \pi/2$ corresponds to a vector potential parallel to the x-axis (zig-zag direction) and a magnetic field parallel to the y-axis (armchair direction). We can easily show (see Appendix C.1) that the eigenvalues of $\hat{H}_{\mathbf{k}}$ change sign under reversal of $\mathbf{k}$ – other parameters remain unchanged. This implies that the system at half-filling can either be an insulator – if there are no zero eigenvalues – or a compensated semimetal with equal densities of electrons and holes in pockets below and above the Fermi level.

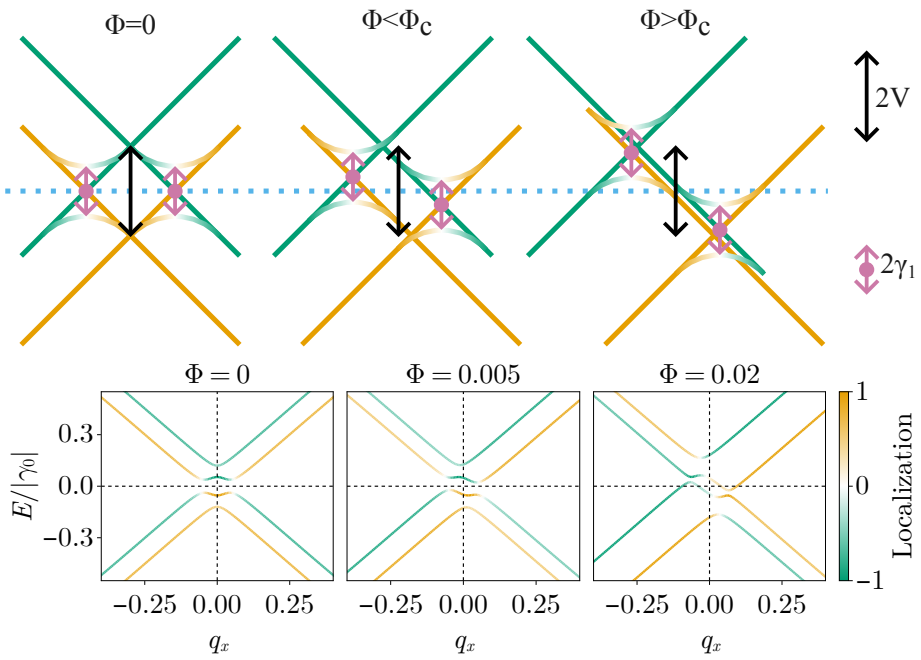

Figure 5.2: *Top row: Schematic illustration of the evolution of the bilayer band structure as a function of* Φ *at finite* V*. The two colors correspond to the unperturbed Dirac cones from the two layers. The dashed lines show the level of repulsion due to inter-layer coupling. The IM transition occurs when the upper anticrossing level on the right and lower one on the left move respectively below and above the chemical potential at half-filling. Bottom row: Numerically computed bands close to the K point* $\left(2\pi/\sqrt{3}, 2\pi/3\right)$ *with* $V = \gamma_1/2$ *demonstrating the insulator-metal transition at* $\Phi_c = |\gamma_1/3\pi\gamma_0| \approx 0.011$*. The direction of the field for all plots is* $\theta = \pi/2$*. The color of the bands shows the distribution of the states over the layers, as defined in the text.*

5.3 Insulator-metal transition

We now show that an IM transition (or, more precisely, a transition from insulator to compensated semimetal) must necessarily occur at a critical value of Φ at half-filling. The top panel of Fig. 5.2 shows schematically the band structures of the two non-interacting monolayers (green and orange cones for top and bottom, respectively) in the vicinity of a Dirac point. The two cones are displaced vertically along the energy axis by the potential V and horizontally along the momentum axis by the in-plane field Φ. Importantly, the crossing between levels belonging to different layers moves above and below the chemical potential by an amount $2\pi v\Phi$ where $v = 3|\gamma_0|/2$ is the velocity of the Dirac fermions with lengths given in terms of the carbon bond length a. With the interlayer coupling switched on, one of the crossing levels is pushed up by γ_1 while the same amount pushes down the other. The system remains an insulator **(possibly a zero-gap insulator in the special case** $V = 0$**)** as long as $\gamma_1 < 3\pi|\gamma_0|\Phi$ and switches to compensated semimetal when this inequality is

violated. This simple argument allows us to pinpoint the transition at

$$\Phi_c = \frac{\gamma_1}{3\pi|\gamma_0|} \tag{5.7}$$

in perfect agreement with more accurate analytical treatment, as shown in Appendix C.2. Notice that Φ_c does not depend on the direction of the in-plane field.

In addition to providing a schematic illustration, we calculate the bands close to the K point and show how they change with Φ. [1] Comparing the results at the bottom of Fig. 5.2 to the schematics in the top row, we observe a good qualitative agreement between the two. For the parameter values given following Eq. (5.4), $\Phi_c \approx 0.011$. Indeed one can see that, for $\Phi < \Phi_c$, the numerical calculations result in a gapped bandstructure, while $\Phi > \Phi_c$ yields a compensated semimetal.

We pause here to comment on the peculiar nature of the semi-metallic state emerging from the IM transition. Due to the simultaneous presence of two types of carriers at the Fermi level its transport properties are expected to be strongly affected by electron-hole scattering resulting in reduced electrical conductivity and enhanced thermal conductivity [93, 94]. The system is also a good candidate for observing the elusive two-fluid hydrodynamics [95, 96].

Although the critical magnetic field is formally proportional to the interlayer coupling γ_1 – and thus can be exponentially reduced by increasing the spacing between the layers – its numerical value is still very large. With commonly accepted values of a and l we find $B_c = |\gamma_1/3\pi\gamma_0|\Phi_0/al \approx 1000$ T. In the concluding section, we will discuss several effects that could bring this large value down to a more accessible range.

5.4 Magnetic Response

The magnetic field enters the Hamiltonian in Eq. (5.4) in the form of a flux; it is convenient to write

$$\begin{aligned} M &= \frac{1}{\mathcal{V}}\frac{d\Omega}{dB} = \frac{al}{\Phi_0}\frac{1}{\mathcal{V}}\frac{d\Omega}{d\Phi}\,, \\ \chi &= \frac{\mu_0}{\mathcal{V}}\frac{d^2\Omega}{dB^2} = \left(\frac{al}{\Phi_0}\right)^2\frac{\mu_0}{\mathcal{V}}\frac{d^2\Omega}{d\Phi^2}\,, \end{aligned} \tag{5.8}$$

[1] All computations in this paper are performed using JULIA [90]. The plots are made with Makie.jl package [91] using the color scheme designed for colorblind readers [92]. The scripts used for computing and plotting can be found at Bilayer graphene in crossed field setup

where μ_0 is the magnetic constant, $\mathcal{V}$ is the area of the system, $d\Phi/dB = al/\Phi_0$ and Ω is the Helmholtz free energy given by

$$\Omega(\Phi,\theta,V,\mu,T) = -T\sum_{\mathbf{k},n}\ln\left[1+e^{-\frac{E_n(\mathbf{k},\Phi,\theta,V)-\mu}{T}}\right]. \tag{5.9}$$

Here, $E_n(\mathbf{k},\Phi,\theta,V)$ is the energy of the nth eigenstate at wave vector $\mathbf{k}$, temperature T, and chemical potential μ. To compute χ, we first set $\Phi \to \Phi+\delta$ and Taylor-expand the Hamiltonian to the second order in δ which yields $H_{\mathbf{k}} \simeq H_{0,\mathbf{k}} + \delta H'_{0,\mathbf{k}} + \frac{1}{2}\delta^2 H''_{0,\mathbf{k}}$, where $H_{0,\mathbf{k}}$ is the Hamiltonian at $\delta = 0$, $H'_{0,\mathbf{k}}$ and $H''_{0,\mathbf{k}}$ are its first and second derivatives also evaluated at $\delta = 0$. Using perturbation theory, we expand the eigenvalues E_n to second order in δ

$$\begin{aligned} E_n(\mathbf{k}) \approx{}& \langle\mathbf{k},n|H_{0,\mathbf{k}}|\mathbf{k},n\rangle + \delta\langle\mathbf{k},n|H'_{0,\mathbf{k}}|\mathbf{k},n\rangle + \delta^2\langle\mathbf{k},n|H''_{0,\mathbf{k}}|\mathbf{k},n\rangle/2 \\ &+ \delta^2\sum_{m\neq n}\frac{|\langle\mathbf{k},n|H'_{0,\mathbf{k}}|\mathbf{k},m\rangle|^2}{E_{0,n}(\mathbf{k})-E_{0,m}(\mathbf{k})}, \end{aligned} \tag{5.10}$$

where $|\mathbf{k},n\rangle$ are eigenvectors of $H_{0,\mathbf{k}}$ and $E^0_n(\mathbf{k})$ are the corresponding eigenvalues. We insert this expression into the logarithm of Eq. (5.9) and expand again to second order in δ to extract the magnetization and the susceptibility:

$$\begin{aligned} M &= -\frac{1}{\mathcal{V}}\frac{al}{\Phi_0}\sum_{\mathbf{k},n} n_F(E_{0,n}(\mathbf{k}))\langle\mathbf{k},n|H'_{0,\mathbf{k}}|\mathbf{k},n\rangle, \\ \chi &= -\frac{\mu_0}{\mathcal{V}}\left(\frac{al}{\Phi_0}\right)^2\sum_{\mathbf{k},n}\left[n_F(E^0_n(\mathbf{k}))\langle\mathbf{k},n|H''_{0,\mathbf{k}}|\mathbf{k},n\rangle + \sum_{m\neq n}\frac{n_F(E^0_n(\mathbf{k}))-n_F(E^0_m(\mathbf{k}))}{E^0_n(\mathbf{k})-E^0_m(\mathbf{k})}|\langle\mathbf{k},n|H'_{0,\mathbf{k}}|\mathbf{k},m\rangle|^2\right] \\ &\quad -\frac{\mu_0}{\mathcal{V}}\left(\frac{al}{\Phi_0}\right)^2\sum_{\mathbf{k},n} n'_F(E^0_n(\mathbf{k}))|\langle\mathbf{k},n|H'_{0,\mathbf{k}}|\mathbf{k},n\rangle|^2 \end{aligned} \tag{5.11}$$

where n_F is the Fermi distribution function and n'_F its derivative with respect to energy. The sum over momenta in the first Brillouin zone is converted into an integral $\mathcal{V}^{-1}\sum_{\mathbf{k}} \to (2\pi a)^{-2}\int_0^{\frac{4\pi}{3}} dk_x \int_0^{\frac{2\pi}{\sqrt{3}}} dk_y$. Numerically calculated χ as a function of Φ at $\mu = 0$ is shown in Fig. 5.3 for several values of V. The most important feature exhibited by the plots is the sharp transition from diamagnetic to paramagnetic behavior at the point of IM transition. It is possible to understand the origins of this behavior by considering individual terms in Eq. (5.11) for $T \to 0$. The first term is negative, i.e., diamagnetic, and has a very weak dependence over the chemical potential. The second and third terms are both positive and therefore paramagnetic. Specifically, the second term describes inter-band paramagnetism [97] and the final term is a Fermi contour contribution that arises from

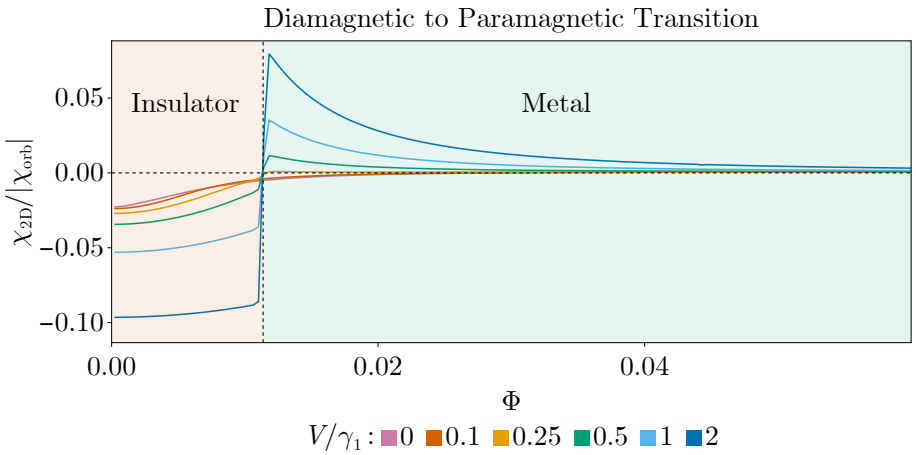

Figure 5.3: *Plot of the orbital magnetic susceptibility (OMS) vs in-plane magnetic flux Φ at $\mu = 0$. The calculation is done at $T = 12K$. Initially diamagnetic in the insulating phase, the susceptibility rapidly becomes paramagnetic at the critical field. The size of the jump in the OMS increases with increasing voltage V between the layers and vanishes for $V \to 0$.*

the direct coupling of the in-plane magnetic field with the fluctuating orbital moment (Appendix C.3): this term vanishes when the system is an insulator.

Clearly, the diamagnetic contribution dominates in the insulating phase. The sharp switch to paramagnetism that accompanies the IM transition results from the irruption of the Fermi surface term. The subsequent decrease of χ with a further increase in Φ suggests that the magnitude of the paramagnetic response strongly depends on the nature of the contributing states at the Fermi level. A closer look at the bottom row of Fig. 5.2 with $\Phi = 0$ reveals that when the Fermi level is close to the band edge the contributing states are essentially *delocalized*, i.e., evenly distributed over the two layers. This implies large inter-layer fluctuations, which in turn are related to large fluctuations of the in-plane component of the orbital moment (see Appendix C.3): hence the large susceptibility "jump" at the IM transition. However, for a displacement field of $V \approx \gamma_1/2$; increasing Φ past Φ_c results in more localized states at the Fermi level, as can be seen in Fig. 5.2 for $\Phi = 0.02$, reducing the orbital moment fluctuation and hence the weak paramagnetic response. Finally, one can see that if V is not sufficiently large (check Appendix C.3 for large displacement field: $V > \gamma_1/2$), that is to say, if the initial insulator at $\Phi = 0$ is not sufficiently strong, the IM transition does not produce sufficient contrast between the two phases and the diamagnetic to paramagnetic crossover is eventually lost.

Finally, we address the role of chemical potential in magnetic susceptibility by plotting χ as a function of μ for several values of Φ and V in Fig. 5.4. Additional gating and/or intentional doping can change the chemical potential. At zero magnetic field (panel (a)) the susceptibility is always negative (i.e., diamagnetic) at $\mu = 0$, in agreement with Fig. 5.3. As μ touches the band edge, χ

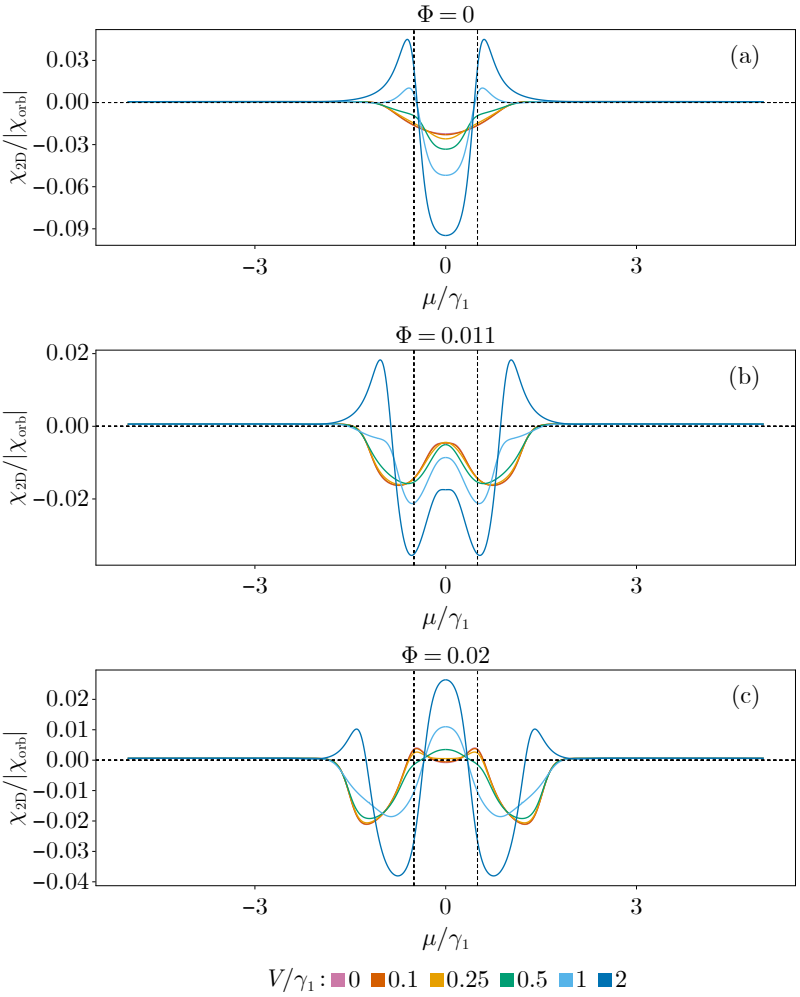

Figure 5.4: *Orbital magnetic susceptibility χ (in units of $\alpha = \mu_0(l/2\pi\Phi_0)^2$) as a function of μ for different values of V and Φ with $\theta = \pi/2$. The calculations are performed at a finite temperature $T = 300K$.*

changes sign and becomes paramagnetic as the Fermi contour contribution becomes dominant, due to the presence of delocalized states at the Fermi level. Further increase of μ reduces the magnitude of χ, as the states at the Fermi level become more localized on one or the other layer.

At the critical magnetic field (Fig.5.4(b)), the zero-μ χ is strongly pushed in the positive direction, in agreement with Fig. 5.3. This "push" results from the combined effect of delocalized states and the band edges, but it is not yet sufficient to create a paramagnetic response. The "push" diminishes as μ moves away from the charge neutrality point and states at the Fermi contour become more localized. Further increasing μ introduces another paramagnetic spike in χ when μ touches the edge of the higher conduction or lower valence bands.

Fig.5.4(c) shows the behavior of the susceptibility in the metallic state. The remarkable feature is that paramagnetism now occurs even at the charge neutrality point. We interpret this as the result

of increasing delocalization of states at the Fermi level, which generates larger fluctuations of the in-plane moment (details in Appendix C.3).

5.5 Observability and Conclusion

We have explored the possibility of altering the band structure, the transport, and the magnetic properties of stacked 2D materials by an in-plane magnetic field acting in conjunction with a vertical displacement field. While our calculations for bilayer graphene employ impractically high magnetic fields, we see considerable potential for reducing the required field through material engineering techniques.

First of all, we notice that electron-electron interactions [98, 99] are predicted to enhance the slope of the single-layer cones by a potentially large numerical factor (logarithmically divergent in theory at the charge neutrality point). While current experiments might be too disordered to observe this effect, it should be present in cleaner samples. This effect can considerably decrease the critical value of Φ.

Second, applying a tensile P-strain pulling the layers apart [100] can exponentially reduce the inter-layer coupling parameter. The strained inter-layer coupling strength is $\gamma_1' = \gamma_1 e^{-5.56*\epsilon_p}$, where $\epsilon_p = (L - L_0)/L_0$ quantifies the uniaxial strain, L and L_0 are, respectively, the deformed and undeformed inter-layer distances of the bilayer. According to this equation γ_1 will be reduced by a factor 3 when the strain is around 20%, and the critical field for the IM transition will be lowered to 270 T (without aid from the many-body effect mentioned above).

Smaller critical fields can also be achieved by turning to artificial graphene structures [101, 102, 103, 104, 105] where the lattice constant is much larger and, accordingly, the band structure can be modified by relatively small magnetic fields. A particularly intriguing case is that of twisted multilayer graphene systems, such as twisted bilayer graphene [106] and twisted double-bilayer graphene [107]. Where shifting the Dirac cones could require an in-plane magnetic field on the order of 10T due to the Moire Brillouin zone.[2] The possibility of tuning the Dirac cones—bringing them together or pushing them apart—has already been experimentally demonstrated in twisted bilayer graphene [84]. Generalizing this behavior to twisted multilayer systems could enable the induction of a metal-insulator transition at significantly lower magnetic fields.

[2]In these systems, a mini (or Moiré) Brillouin zone emerges, and the distance between the nearest Dirac cones is reduced to approximately one-hundredth of its original value for small twist angles. This reduction leads to a critical magnetic field of approximately 10 T. Our work outlines a fundamental mechanism for the IM transition in crossed fields within the simplest possible model. Although more complex systems, such as twisted multilayer graphene, are beyond the scope of this paper, they offer a promising direction for future research.

Chapter 6

TRIGONAL WARPING ENABLED LOW-FIELD METAL-INSULATOR TRANSITION IN AB-STACKED BILAYER GRAPHENE

6.1 Introduction

Bilayer and multilayer graphene systems, however, offer even richer tunability. Their interlayer coupling and stacking geometry enable mechanical, electrical, and magnetic control over band topology. For instance, twisted bilayer graphene hosts flat bands that give rise to superconductivity and correlated insulating states [77], while Bernal-stacked bilayers exhibit gate-tunable bandgaps [108] and orbital magnetism sensitive to in-plane magnetic fields ($B_{\|}$) [79, 80]. The latter arises because $B_{\|}$ couples asymmetrically to the two layers, shifting their uncoupled band structures in opposite momentum directions. However, accurately capturing the low-energy behavior under such conditions requires accounting for full tight-binding which includes the skew interlayer couplings. Including this effect is therefore essential to understand the experimentally relevant magnetic response the required field scales of the insulator–metal transition.

When interlayer hybridization is activated, this generates reconstructed Fermi surfaces and anomalous orbital responses [83]. Despite these advances, the low-energy band structure of BLG remains controversial. The low-energy distortion of the Fermi surface induced by interlayer skew couplings (γ_3, γ_4) in the Slonczewski–Weiss–McClure model [109, 110]. These terms are less pronounced in tight-binding descriptions of AB-stacked bilayer graphene at higher energy regimes [111], yet near the Dirac points they significantly renormalize the Fermi velocity and impart a threefold symmetry to the band topology [12, 108, 112]. Quantum-Hall experiments at low carrier density report an eightfold degeneracy of the lowest Landau level—consistent with a parabolic dispersion and spin, valley, and

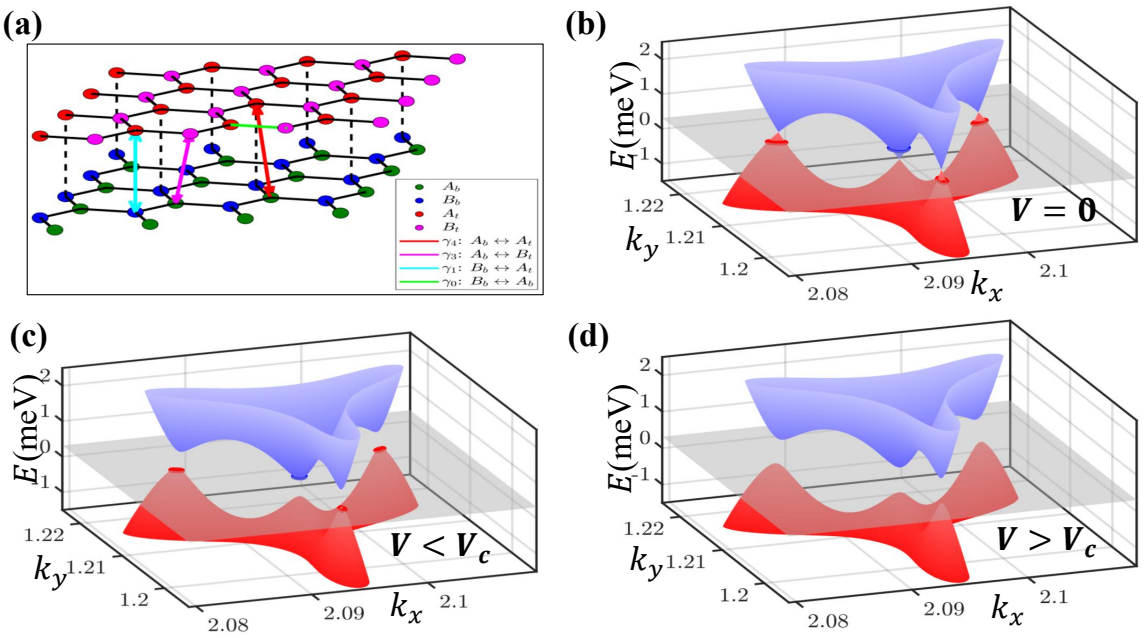

Figure 6.1: *AB-stacked bilayer graphene lattice and band structure with trigonal warping.* ***(a)*** *Side view of the AB-stacked lattice showing relevant interlayer hopping terms.* ***(b)*** *Semi-metallic state at zero field with* $E_F = 0.313$ meV. ***(c)*** *Semi-metallic state with displacement field slightly below the critical value.* ***(d)*** *Insulating state achieved by exceeding the critical displacement field.*

orbital symmetries [67, 113, 114] —whereas tight-binding models that include skew hoppings (γ_3, γ_4) predict a gapless fine-structure featuring four mini-Dirac cones and van Hove singularities at modest displacement fields [2, 113, 115] . Moreover, large $E_\perp$ opens sizable gaps and yields anomalous quantum-Hall sequences in BLG[116, 117, 118, 119] and Bernal trilayer graphene [120, 121, 122], rhombohedral trilayer graphene [123, 124] and Bernal tetralayer graphene [125], which is consistent with the theoretical band structure predicting a trigonally-warped low-energy Fermi surface topology.

Recently, Seiler et al. [108] investigated the fine structure of trigonal warping under an applied displacement field—both theoretically and experimentally—underscoring its relevance. In their work they aimed to resolve the puzzle of why the linearly dispersing bands and electric-field-induced changes of topology have not been observed experimentally in BLG. They combined high-field magneto-transport on hBN-encapsulated bilayer graphene with realistic tight-binding modeling to show signs of topological changes in the band structure involving a van Hove singularity should be detectable, e.g., in a quantizing magnetic field in which the presence of four Dirac cones results in an exotic sequence of Landau levels distinct from the previously studied instances of Landau levels. Establishing BLG as a truly field-tunable Dirac material with an accessible gap up to 250 meV and rich correlated phenomenology.

However, the combined effects of $B_\parallel$ and transverse electric fields ($E_\perp$)—an exotic pairing for

bilayer band engineering—remain underexplored, more so in the presence of trigonal warping. In our prior work [111], we demonstrated that $B_{\parallel}$ and $E_{\perp}$ synergistically drive an insulator-metal (IM) transition in AB-stacked bilayer graphene (AB-BLG). Here, $E_{\perp}$ opens a bandgap, while $B_{\parallel}$ hybridizes layer-polarized states, closing the gap above a critical field B_c.

In our previous work [111], we showed that $E_{\perp}$ and $B_{\parallel}$ together drive an insulator–semimetal transition in BLG by opening a gap and then closing it above a critical field B_c. That study, however, neglected trigonal warping and predicted $B_c \gtrsim 100\,\mathrm{T}$, well beyond experimental reach.

Here, we remedy this omission by incorporating skew hoppings into the full tight-binding simulations of the $B_{\parallel}$–$E_{\perp}$–induced transition (Fig. 6.1a–b). Focusing on the Fermi surface within roughly 1% of the original Brillouin zone (i.e., within ~ 1 meV of the Dirac points), we uncover two key results. First, there exists a critical displacement field beyond which a true gap opens. Second, trigonal warping dramatically lowers the critical magnetic field B_c for the IM transition, reducing it from over 100T [111] to ~ 10T—a range accessible to modern cryogenic magneto-transport experiments [126]. At very large $B_{\parallel}$, warping effects become negligible as the Fermi surface coalesces into a single anisotropic pocket, recovering the high-field behavior reported in our earlier study [111].

These results resolve the paradox between early theoretical predictions of weak field responses and recent experiments observing $B_{\parallel}$-tunable magnetism at moderate fields , while highlighting trigonal warping as a critical lever for designing graphene-based magneto-electronic devices.

More broadly, our work demonstrates how low-energy band topology—shaped by skew couplings—can be engineered with crossed electric and magnetic fields, opening new directions in correlated Dirac physics and device applications.

6.2 Tight Binding Model.

The Bernal-stacked graphene bilayer is described by a tight-binding Hamiltonian with nearest-neighbor intra- and interlayer hopping [87]

$$H_{\mathbf{k}} = \begin{pmatrix} -V/2 & \gamma_0 f(\mathbf{k}_{\mathrm{t}}) & \gamma_4 f(\mathbf{k}) & \gamma_3 f^*(\mathbf{k}) \\ \gamma_0 f^\dagger(\mathbf{k}_{\mathrm{t}}) & -V/2+\Delta & \gamma_1 & \gamma_4 f(\mathbf{k}) \\ \gamma_4 f^*(\mathbf{k}) & \gamma_1 & V/2+\Delta & \gamma_0 f(\mathbf{k}_{\mathrm{b}}) \\ \gamma_3 f(\mathbf{k}) & \gamma_4 f^*(\mathbf{k}) & \gamma_0 f^\dagger(\mathbf{k}_{\mathrm{b}}) & V/2 \end{pmatrix} \tag{6.1}$$

The four basis states are $\mathrm{A_t}$, $\mathrm{B_t}$, $\mathrm{A_b}$, and $\mathrm{B_b}$ with A and B denoting the sublattice and t/b subscripts identifying the top and bottom layers. The hopping energy between $\mathrm{B_t}$ and $\mathrm{A_b}$ is $\gamma_1 = 0.361$eV,

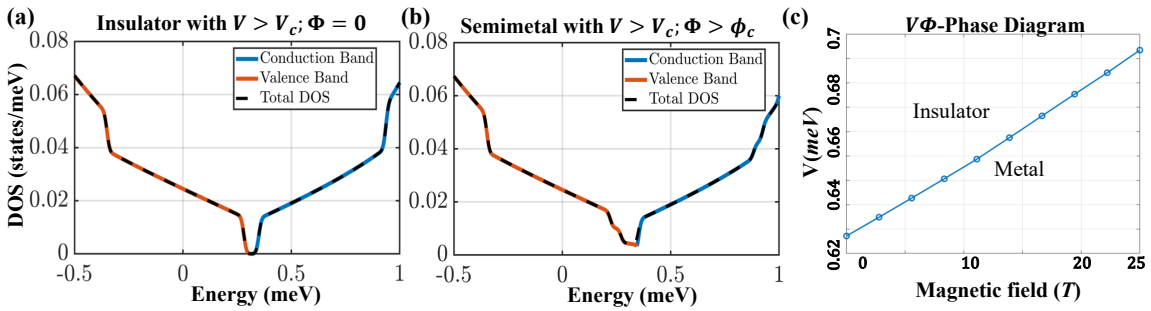

Figure 6.2: *Density of states across the metal–insulator transition.* ***(a)*** *Insulating state for $V > V_c$ with vanishing DoS.* ***(b)*** *Semi-metallic state restored by in-plane magnetic field $\phi > \phi_c$.* ***(c)*** *V–ϕ phase diagram showing the critical magnetic field for gap closure, with cutoff at* 25 T.

while the hopping term between the nearest neighbors within a layer is $\gamma_0 = -2.61$eV [108, 127]. $f(\mathbf{k}) = \sum_{n=1}^{3} e^{i\mathbf{k}\cdot\boldsymbol{\delta}_n}$, where $\boldsymbol{\delta}_1 = a(-1, \sqrt{3})/2$, $\boldsymbol{\delta}_2 = a(-1, -\sqrt{3})/2$, and $\boldsymbol{\delta}_3 = a(1, 0)$ are the vectors connecting atoms A to their nearest neighbors within a layer and $a \approx 1.42$Å is the carbon bond length in graphene. The diagonal terms $\pm V$ originate from an external electric field applied perpendicular to the bilayer (the displacement field). In addition to the nearest-neighbor intralayer hopping energy, we also include the skew interlayer couplings $\gamma_3 = -0.283$ eV, $\gamma_4 = 0.138$ eV and the energy difference between dimer and non-dimer sites $\Delta = 0.015$ eV [108, 127]. Using this model, we demonstrate that the insulator-to-metal (IM) transition predicted in the effective Hamiltonian discussed in the our previous work [111] and it also occurs in the full tight-binding model.

Finally, the constant vector potential is incorporated into the Hamiltonian by using the Peierls substitution $\mathbf{k} \to \mathbf{k} \pm e\mathbf{A}/\hbar$, so that we have

$$\mathbf{k}_{\mathrm{t/b}} a = \mathbf{k} a \pm \pi\Phi(\sin\theta, -\cos\theta, 0)\,, \tag{6.2}$$

where l is the interlayer separation and $\Phi = Bal/\Phi_0$ is the magnetic flux through a rectangle defined by an intra-plane bond and an inter-plane segment in units of the magnetic flux quantum $\Phi_0 = h/e \simeq 4.14 \times 10^5$ T.Å^2. Here $\theta = \pi/2$ corresponds to a vector potential parallel to the x-axis (zig-zag direction) and a magnetic field parallel to the y-axis (armchair direction). It is worth noting that the skew-coupling terms do not accumulate the Peierls phase; and the possible reasoning could be understood as the skew couplings are a second derivative of the motion in the z-direction; which does not get effected by the in-plane vector potential.

6.3 Accessible IM-Transition Enabled by Trigonal Warping

In our previous work [111], we analyzed the insulator–semimetal transition in AB-stacked bilayer graphene at half filling under a transverse field $E_\perp$ and an in-plane magnetic flux Φ, modeling each layer as a Dirac cone displaced vertically by $\pm V$ and horizontally by $\Delta k = \Phi/a$. By including only the interlayer coupling γ_1, we found that the system remains gapped for

$$\gamma_1 < 3\pi|\gamma_0|\,\Phi \quad \Longrightarrow \quad \Phi_c = \frac{\gamma_1}{3\pi|\gamma_0|},$$

and transitions to a compensated semimetal when this inequality is violated, corresponding to an unreasonably large critical field $B_c \approx 100\,\mathrm{T}$ (with additional P-strain). In the present work, we show that including trigonal-warping terms dramatically lowers B_c into the $\sim$ 10T (Fig. 6.2) range by concentrating low-energy states in to trigonal shaped iso-energy contours where the interlayer form factor remains finite. This significantly lower B_c arises because skew hoppings (γ_3, γ_4)—and the resulting trigonal warping—is taken into account: their inclusion enhances interlayer coherence near the Dirac points and requires accesible fields to hybridize the bands.

Following the Ref.[12] one can show that at low-energy; the effect of trigonal warping in the two-band model causes a Lifshitz transition for energies $|E| < \epsilon_L$, where $\epsilon_L = \frac{\gamma_1}{4}\left(v/v_3\right)^2 \approx 1\mathrm{meV}$. The iso-energetic lines are broken into four separate 'pockets' consisting of one central pocket and three 'leg' pockets. By resolving the band structure at $1/100^{\mathrm{th}}$ of the original Brillouin zone (BZ) length scale, we uncover threefold-symmetric Dirac cones (Fig. 6.1c) that fundamentally alter the insulator-metal (IM) transition.

6.3.1 Critical Displacement Field and Gap Opening

At zero in-plane field ($B_\parallel = 0$) and in the low-energy window ($|E| \lesssim 1\,\mathrm{meV}$), trigonal warping fragments the Fermi surface into one central pocket (conduction band) and three satellite pockets (valence band) around each K point (Fig. 6.1b). Applying a perpendicular displacement field $E_\perp$ gaps the central Dirac cone at zero energy but leaves the warped pockets intact, so the system remains semimetallic until

$$V_c \approx 0.63\ \mathrm{meV}\,. \tag{6.3}$$

Below V_c, residual valence-band pockets sustain a finite density of states at the Fermi level (shifted to $E_F \approx 0.31\,\mathrm{meV}$ by particle–hole asymmetry from γ_4), whereas for $V > V_c$ all pockets are gapped

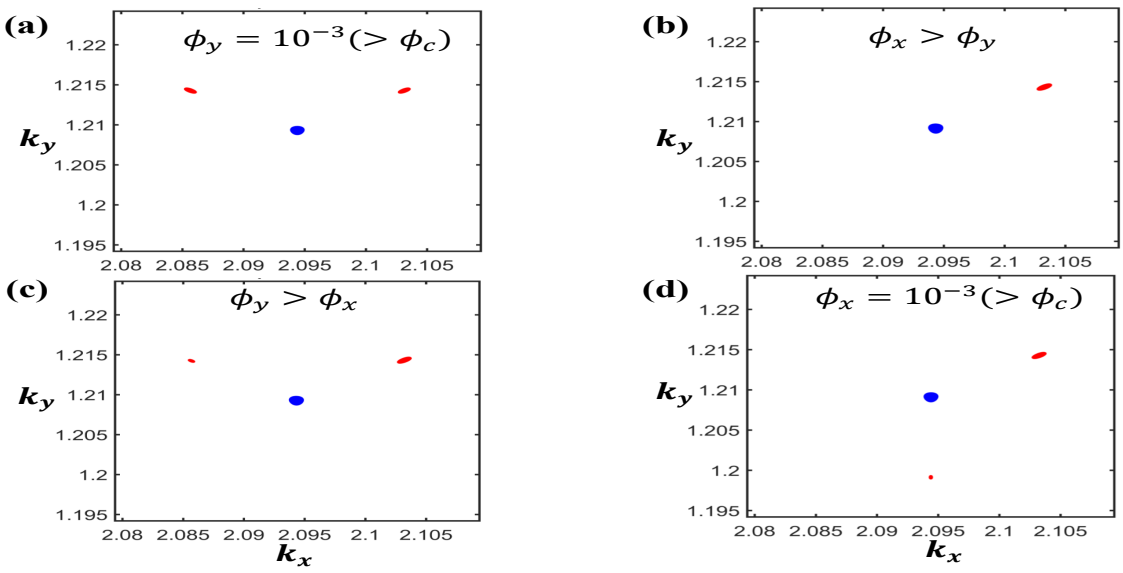

Figure 6.3: *Evolution of Fermi Surface with different direction of in-plane magnetic field (ϕ) at IM Transition ($V > V_c$).*

and a full bulk gap appears (Fig. 6.1c–d). This suppressed gap opening—absent in high-energy models—provides the baseline for mapping the IM phase boundary in the (V, Φ) plane.

We extract V_c by direct diagonalization of the full tight-binding Hamiltonian on a dense k-grid, tracking the minimum indirect gap via Eq. (6.4). Because V_c depends sensitively on the skew-hopping ratio γ_3/γ_1, our results suggest that strain or dielectric engineering could tune the threshold, offering an additional control parameter for low-field IM transitions.

This behavior has two key implications. First, it highlights the necessity of including skew-hopping terms (γ_3, γ_4) when modeling low-energy transport and optics: below V_c, the ungapped pockets dominate conductivity and yield anisotropic cyclotron orbits in quantum-oscillation measurements. Second, the Berry-curvature textures of these warped pockets—even prior to full gap opening—may drive pronounced valley-Hall or nonlinear Hall responses that switch sharply at V_c.

With V_c established as the "zero-field" gap threshold, we can now explore how an in-plane magnetic flux Φ further suppresses or closes the gap, thereby tracing out the IM phase boundary in the (V, Φ) plane.

6.3.2 Phase-Boundary Determination

To map out the insulating and semimetallic regions in the (V, Φ) plane, we compute the 4×4 bilayer Hamiltonian $H(\mathbf{k}; V, \Phi)$ on a fine grid of Bloch momenta $\mathbf{k}$ centered at the K point, including all Slonczewski–Weiss–McClure hoppings $(\gamma_0, \gamma_1, \gamma_3, \gamma_4)$ and the displacement field V. For each (V, Φ)

we diagonalize H and extract the two middle eigenvalues

$$E_2(\mathbf{k}; V, \Phi) \leq E_3(\mathbf{k}; V, \Phi)\,,$$

$E_2(\mathbf{k}; V, \Phi)$-higest valence band and $E_3(\mathbf{k}; V, \Phi)$-lowest conduction band. We define the local gap

$$E_g(V, \Phi) = \min_{\mathbf{k}} \big[E_3(\mathbf{k}; V, \Phi) - E_2(\mathbf{k}; V, \Phi)\big]. \tag{6.4}$$

By convention, $E_g > 0$ corresponds to an insulator, while $E_g \leq 0$ signals a compensated semimetal. For fixed Φ, we scan V in small increments, compute $E_g(V)$ via Eq. (6.4), and interpolate between successive points to locate the critical displacement $V_c(\Phi)$ at which $E_g = 0$. Repeating this procedure for various Φ constructs the phase-boundary curve $V_c(\Phi)$ illustrated in Fig. 6.2(c).

6.3.3 Magnetic-Field Dependence and Reduced B_c

To investigate the metal–insulator transition in our bilayer graphene system, we first examine the density of states (DoS) under different external field configurations, as shown in Fig. 6.2. When the displacement field V exceeds the critical value V_c, the DoS at the Fermi level vanishes, signalling the opening of a full bandgap and the onset of an insulating phase (Fig. 6.2(a)). Applying an in-plane magnetic field ϕ above a critical threshold ϕ_c closes this gap, producing a finite DoS at the Fermi level and restoring a semi-metallic phase (Fig. 6.2(b)). To capture the complete transition, we construct a V–ϕ phase diagram beginning at $V = V_c$ and extending to $V \approx 0.71$ meV, indicating the critical magnetic field required for gap closure at each displacement field. For relevance to current experiments, we limit the field range to $B \leq 25$ T (Fig. 6.2(c)).

With the phase boundary in hand, we convert $\Phi_c(V)$ into a critical magnetic field $B_c(V) = \Phi_c(V)\,\Phi_0/(a\,l)$. Including trigonal warping, we find Φ_c lies near 10 T—two orders of magnitude lower than the unwarped prediction ($B_c \gtrsim 1000$ T). The dramatic reduction has two main origins: (i) Trigonal warping reconstructs the low-energy spectrum into four mini-Dirac pockets, each retaining interlayer coherence through skew hopping γ_3. Hybridization at these discrete pockets requires much smaller in-plane Peierls phases than in the isotropic case. (ii) Once Φ exceeds $\Phi_c(V)$, the DoS at the Fermi level changes abruptly from zero to a finite value, reflecting the sudden emergence of compensated electron–hole pockets.

Quantitatively, we find that in the low-energy regime a displacement field $V > V_c$ opens an indirect gap, defined as the difference between the minimum of the conduction band and the maximum of the

valence band $E_{c,min} - E_{v,max} = \Delta(V) \propto V - V_c$; but an in-plane magnetic field closes this gap by promoting interlayer hybridization. This behavior differs qualitatively from our earlier high-energy analysis, where the zero -B (magnetic field) indirect gap was essentially set by the interlayer coupling γ_1 and appeared insensitive to V. In the present, warped low-energy bandstructure the zero-B gap is parametrically smaller (fractions of a meV rather than hundreds of meV). The primary cause is likely the skew coupling γ_4, which breaks electron–hole symmetry and unpins the relative energies of the pocket extrema, so that the "bare" gap at zero field scales with $V - V_c$ rather than being fixed by γ_1.

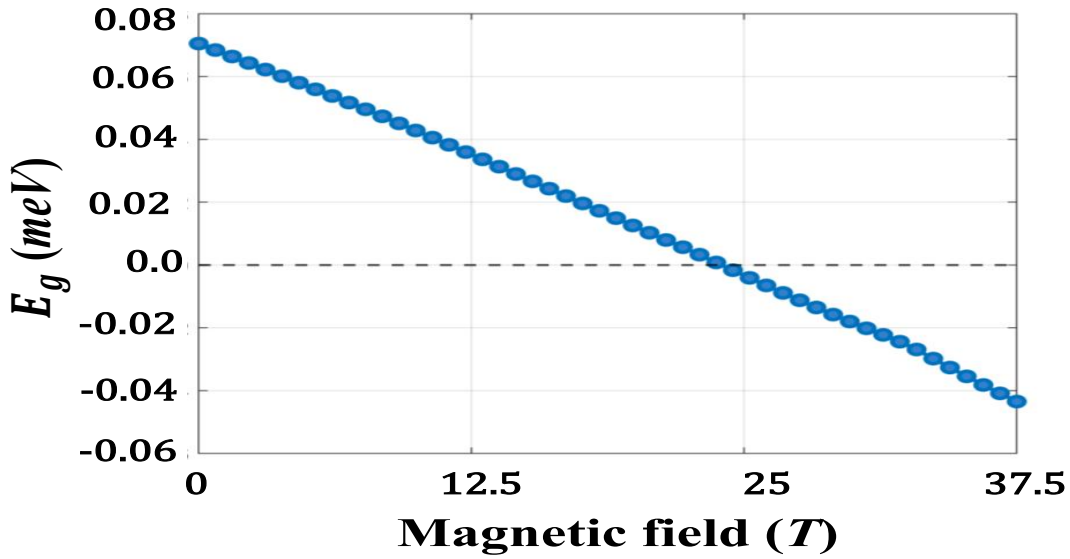

Figure 6.4: *At displacement field $V > V_c$: $0.7meV$. Evolution of the indirect band-gap E_g with respect to applied in-plane magnetic field strength ϕ. Shows almost linearly decreasing nature with increasing magnetic field.*

It is useful to parametrize the field dependence of the bare gap by the magnetic-field induced momentum shift. Denoting by k_B the characteristic momentum displacement produced by the in-plane field (with $k_B \propto eB\ell/\hbar$, where ℓ is the interlayer spacing), the leading effect of the field on the gap can be written phenomenologically (Fig. 6.4) as

$$E_g(B) \;=\; E_g(0) \;-\; \alpha\,\hbar v\,k_B, \tag{6.5}$$

where $E_g(0) \equiv \Delta(V)$, v is the relevant Dirac velocity near the pockets, and $\alpha \gtrsim 1$ is a dimensionless coefficient that encapsulates details of the pocket geometry and interlayer overlap. Equation (6.5) captures the linear closing of the gap with field observed in our numerics.

Setting $E_g(B_c) = 0$ yields an analytic estimate for the critical field,

$$B_c \;=\; \frac{E_g(0)}{\alpha\,\hbar v}\,\frac{\hbar}{e\ell} \;\propto\; E_g(0) \;\propto\; (V - V_c). \tag{6.6}$$

Thus, because $E_g(0) \propto V - V_c$ in the trigonal-warped low-energy regime, B_c acquires an approximately linear dependence on the displacement field. This explains our observation at Fig. 6.2 that B_c grows roughly linearly with $V - V_c$ (e.g. reaching $B_c \sim 25\,\mathrm{T}$ at $V \approx 0.71\,\mathrm{meV}$ in the parameter set used here), and it also clarifies why the required fields are orders of magnitude smaller than the unwarped estimate.

Finally, we emphasize the crossover to the high-field (or high-momentum) regime. The linear scaling in Eq. (6.6) holds while the magnetic-field–induced momentum shift satisfies $k_B \ll k_w$, where k_w is the characteristic momentum scale of trigonal warping (the distance of the mini-pockets from the central cone [12]). Once k_B becomes comparable to or larger than k_w, warping is effectively washed out, the pocket picture breaks down, and the phase boundary should saturate toward the constant-field behavior found in our previous high-energy study.

In short, including trigonal warping both (i) reduces the zero-field gap (via γ_4 and the pocket structure) and (ii) converts the IM critical field from a V-independent constant into an approximately linear function of $V - V_c$, with a crossover back to the earlier constant-B_c result at sufficiently large in-plane magnetic field.

6.4 Discussion & Conclusion

In this work, we have demonstrated that including trigonal-warping terms (γ_3, γ_4) in the tight-binding description of AB-bilayer graphene under crossed in-plane $(B_\parallel)$ and displacement $(E_\perp)$ fields leads to an insulator–semimetal (IM) transition at magnetic fluxes and field strengths an order of magnitude smaller than previously predicted. While earlier high-field treatments—neglecting skew couplings—yielded critical fields $B_c \gtrsim 1000\,\mathrm{T}$, we find $B_c \sim 10\,\mathrm{T}$ once low-energy warping distorts the Fermi surface into four mini-Dirac pockets of finite interlayer overlap. This dramatic reduction stems from two complementary effects: (i) the emergence of threefold-symmetric pockets near each Dirac point, where the interlayer form factor f_k remains finite even under in-plane Peierls phases, and (ii) the enhanced hybridization mediated by γ_3, which lowers the energy cost of band-inversion at each pocket.

Our full tight-binding calculations (Fig. 6.1) confirm that for $\Phi < \Phi_c$ the system remains a gapped

insulator, whereas for $\Phi > \Phi_c$ compensated electron-hole pockets immediately appear. Importantly, Φ_c varies only weakly with the direction of the applied in-plane field, owing to the threefold symmetry of the warped pockets, and remains within the reach of modern cryogenic magneto-transport facilities [126]. This behavior contrasts with our previous high-energy analysis, where the critical magnetic field was found to be independent of the applied electric field, yielding a constant B_c for all V. The present low-energy treatment reveals an almost linear dependence of B_c on V, which we expect to saturate once the magnetic-field–induced momentum shift exceeds the characteristic scale set by trigonal warping. At that point, the phase boundary should converge to the constant-field result from our earlier study.

Conspicuously absent from our discussion is the effect of Zeeman coupling, which shifts the energies of opposite spins by $\pm\mu_B B$ (with $\mu_B = e\hbar/2m$), independently of momentum. In the convention used here the down-spin band is pushed downward by $-\mu_B B$ while the up-spin band is pushed upward by $+\mu_B B$. As a result the spin-resolved separations between conduction and valence extrema are modified as

$$E_{c,\min}(\downarrow) - E_{v,\max}(\uparrow) = E_g(B) - 2\mu_B B = E_g(B) - \frac{e\hbar B}{m},$$

and

$$E_{c,\min}(\uparrow) - E_{v,\max}(\downarrow) = E_g(B) + 2\mu_B B = E_g(B) + \frac{e\hbar B}{m},$$

where $E_g(B)$ denotes the spinless (orbital) gap including orbital-field effects. Because one channel is reduced by $2\mu_B B$, the net effect of Zeeman coupling is to make the system more semimetallic at zero displacement: a larger displacement field is therefore required to open a spin-degenerate bulk gap. In other words, Zeeman shifts produce a small upward renormalization of the critical displacement V_c needed to convert the warped semimetal into a full insulator.

Crucially, however, in the low-energy, trigonal-warped regime the zero-field gap itself scales with the displacement as $E_g(0) \equiv \Delta(V) \propto V - V_c$, so the leading control parameter for the IM transition is $V - V_c$ rather than the Zeeman energy. The Zeeman contribution thus appears merely as an additive correction to E_g (equivalently a tiny shift of V_c), and it does not alter the orbital mechanism that closes the V-dependent gap. Consequently the critical in-plane field B_c that closes an already opened gap remains governed by the orbital physics and the difference $V - V_c$, to leading order independent of the Zeeman term.

This statement can be quantified by comparing the Zeeman scale $2\mu_B B \sim e\hbar B/m$ with the orbital

field term responsible for gap closing, which in our phenomenology scales as $\sim (\alpha v_F e B \ell)/(2\pi)$. Their ratio is

$$\frac{e\hbar B/m}{(\alpha v_F e B\ell)/(2\pi)} \sim \frac{\hbar}{m v_F \ell}\frac{2\pi}{\alpha} \sim \frac{a}{\alpha \ell},$$

where a is the in-plane bond length and we used $\hbar/(mv_F) \sim a$ parametrically. With $a/\ell \approx 0.3$ and $\alpha \gtrsim 1$ (in practice $\alpha > 1$ in the warped, low-energy regime) this ratio is small. Even in the conservative case $\alpha \simeq 1$, the Zeeman correction to the required transition field is modest; for realistic parameters it is essentially negligible.

We therefore conclude that Zeeman coupling increases the threshold displacement V_c slightly (because it makes the unperturbed system more semimetallic), but the resulting fractional change of the critical in-plane field is vanishingly small in the parameter range studied. Accordingly, Zeeman effects do not alter our principal conclusion that trigonal warping renders the IM transition experimentally accessible.

These findings open several exciting avenues for future exploration. Experimentally, gated bilayer-graphene devices can now be probed in pulsed or hybrid magnets up to ∼30 T to directly observe the predicted gap closing via measurements of longitudinal conductivity, thermopower, and quantum oscillations [128]. The three mini-pocket topology also suggests the possibility of tuning carrier imbalance between pockets by suitable strain or twist, enabling controlled studies of multi-valley hydrodynamics and two-fluid transport [95].

Finally, the central role of skew-hopping–induced warping in lowering B_c raises the prospect that other two-dimensional moiré and multilayer systems—where skew couplings are inherently strong—may exhibit similarly accessible IM transitions. For instance, trilayer graphene, transition-metal dichalcogenide bilayers, and twisted heterostructures could be designed to exploit warping-facilitated band inversions at modest fields. By revealing how low-energy geometrical distortions can govern field-driven phase boundaries, our study provides a blueprint for engineering tunable semimetallic states in van der Waals materials.

Chapter 7

TWISTED BILAYER GRAPHENE UNDER CROSSED ELECTRIC AND MAGNETIC FIELD

7.1 Introduction

Understanding field-induced electronic phase transitions in two-dimensional materials has been a overarching theme of this thesis. In particular, Bernal-stacked bilayer graphene has served as a model system for studying such transitions under external electric and magnetic fields. Our previous investigation into this system revealed two key effects: an insulator-to-metal transition and a corresponding shift in magnetic response from diamagnetism to paramagnetism. However, a major challenge remains—the required external field strengths are prohibitively large, making experimental verification difficult.

To overcome this limitation, we turn to twisted multilayer graphene, a system that hosts moiré superlattices with significantly reduced Brillouin zone dimensions. We start with twisted bilayer graphene and in low-angle TBG, the moiré mini Brillouin zone is approximately 1/100th the size of the original graphene Brillouin zone. This rescaling has profound consequences: momentum shifts that require extreme fields in Bernal bilayers can now be achieved with field strengths that are orders of magnitude lower. The moiré potential also enhances interaction effects, making TBG a prime candidate for realizing field-induced phase transitions under experimentally accessible conditions. Twisted bilayer graphene (TBG) has emerged as a revolutionary platform for exploring correlated quantum phenomena, driven by its tunable Moiré superlattice and flat electronic bands [14]. When two graphene layers are rotated to a "magic angle" ($\approx 1.1^\circ$), the resulting flat bands near the Fermi level host strong electron-electron interactions, leading to superconductivity, correlated insulating states, and orbital magnetism [15, 129, 130, 131]. These results imply that valley- or orbital-polarized

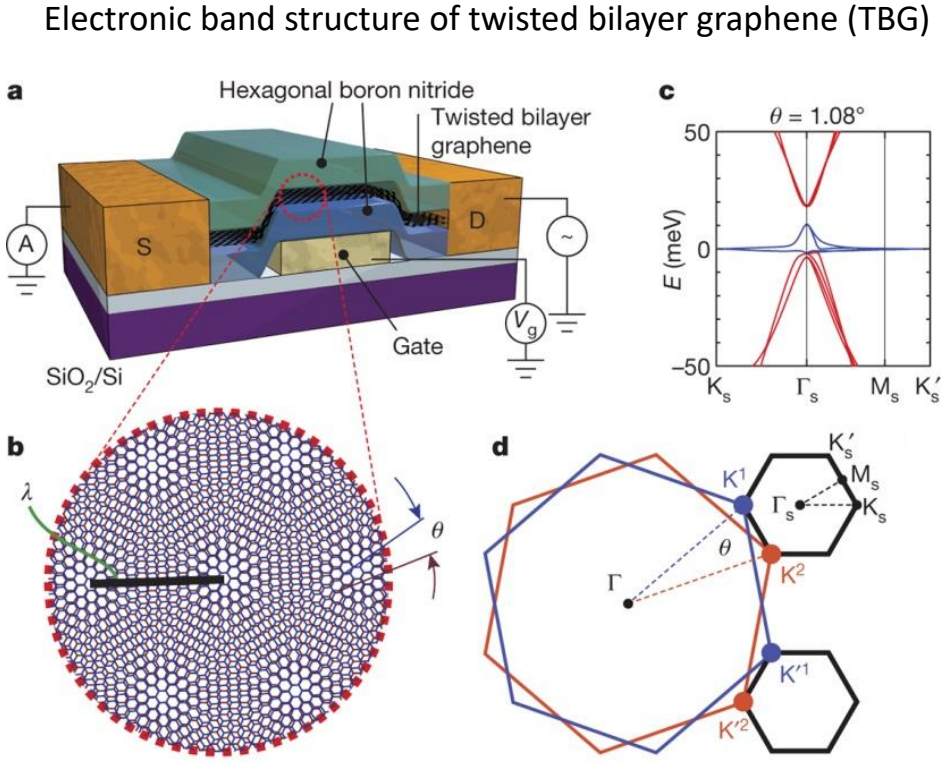

Figure 7.1: Moiré superlattice at the magic angle. *(a) STM topography of TBG at $\theta \approx 1.1°$, revealing the large-scale triangular moiré pattern. (b) The emergence of flat bands at the Fermi energy. Source: Ref ([129]).*

orders (spontaneous orbital magnetism) can suppress or compete with superconductivity, highlighting an interplay between orbital magnetism and superconductivity distinguishing TBG from conventional superconductors. Furthermore, recent theoretical work ([132]) also predicts that in-plane magnetic fields can fundamentally alter the band structure, transforming linear Dirac cones into parabolic dispersions at a critical field strength. These predictions identify an in-plane "orbital" effect that reshapes TBG's band topology.

This interplay between geometry, correlation, and magnetic response makes TBG a rich testbed for probing quantum phase transitions and designing novel electronic states. By resolving how magnetic fields engineer band topology and suppress superconductivity in twisted graphene systems, this project aims to establish design principles for next-generation quantum materials with atomic-level control over spin, topology, and correlation.

In this work, we investigate whether the insulator-to-metal transition observed in Bernal bilayers can manifest in TBG at reduced field strengths. We begin by constructing a continuum model for

TBG in the chiral limit (or the TKV model [133]), where the two dominant interlayer tunneling amplitudes are retained while the smaller ones responsible for particle–hole asymmetry are neglected. This approximation simplifies the moiré Hamiltonian and highlights the essential flat-band physics governed by interlayer interference. We then benchmark the resulting model against well-established theoretical results. We benchmark our band structure calculations against well-established theoretical results. Once validated, we introduce external fields to examine their impact on the system's electronic structure, searching for signatures of the transition. This study not only extends our understanding of field-induced phase transitions in graphene-based materials but also provides insights into engineering electronic states via moiré superlattices.

7.2 Continuum Model Hamiltonian

7.2.1 Geometry and moiré pattern

A general geometry for a twisted bilayer graphene (tBLG) can be constructed as follows: we start with a Bernal-stacked bilayer, rotate the second layer by an angle θ (counter-clockwise about the origin), and then translate it by a vector $\boldsymbol{\tau}$. The two layers can then be expressed as

$$\mathbf{R}^{(1)}_{n_1,n_2} = n_1\mathbf{a}_1 + n_2\mathbf{a}_2, \tag{7.1}$$

$$\mathbf{R}^{(2)}_{n_1,n_2} = R_\theta\left(n_1\mathbf{a}_1 + n_2\mathbf{a}_2 - \boldsymbol{\delta}\right) + \boldsymbol{\tau}, \tag{7.2}$$

where R_θ is the 2×2 rotation matrix describing a counter-clockwise rotation by θ:

$$R_\theta = \begin{bmatrix} \cos\theta & -\sin\theta \\ \sin\theta & \cos\theta \end{bmatrix}. \tag{7.3}$$

Here, each lattice vector points to a sublattice A carbon atom. From Eqs. (7.1) and (7.2), we can write the useful relation

$$\mathbf{R}^{(2)}_{n_1,n_2} = R_\theta\left(\mathbf{R}^{(1)}_{n_1,n_2} - \boldsymbol{\delta}\right) + \boldsymbol{\tau}. \tag{7.4}$$

7.2.2 Rotated Dirac Hamiltonian

From now on, we closely follow the work done in ref. [26] and explain the model we shall adopt for this material. We begin by obtaining the Dirac Hamiltonian for a rotated SLG. We start with

the SLG Dirac Hamiltonian and write it as

$$H_{SLG}^{\pm K}(\mathbf{q}) = \pm\hbar v_F|\mathbf{q}| \begin{bmatrix} 0 & e^{\mp i\theta_q} \\ e^{\pm i\theta_q} & 0 \end{bmatrix}, \tag{2.70}$$

For a rotated SLG[1], we may argue that, applying the same (passive) transformation to our coordinate system, we obtain the same expression. Then, we can go back to our primary coordinate system and write

$$H_{SLG}^{\pm K}(\mathbf{q},\theta) = \pm\hbar v_F|\mathbf{q}| \begin{bmatrix} 0 & e^{\mp i(\theta_q+\theta)} \\ e^{\pm i(\theta_q+\theta)} & 0 \end{bmatrix}, \tag{2.71}$$

where $\mathbf{q}$ is now measured from the rotated Dirac points, $\pm\mathbf{K}^{\theta}$.

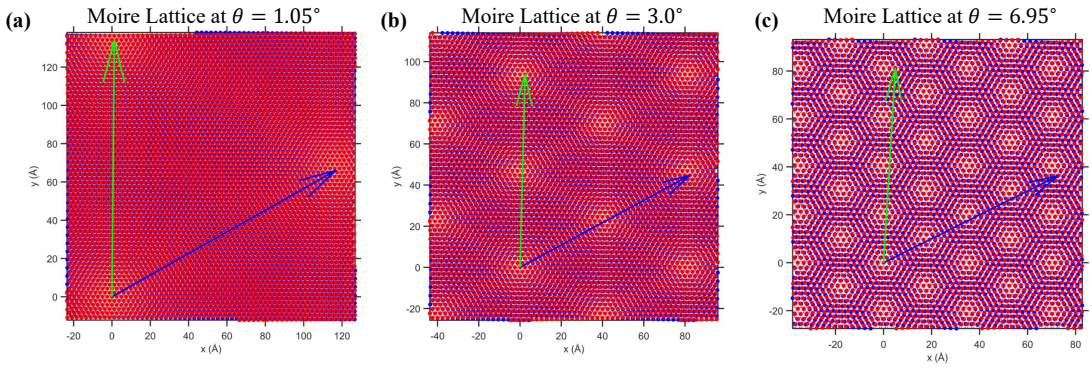

Figure 7.2: *tBLG geometry for $\theta = 1.05°, 3.0°$ & $6.95°$ (top view). Moire superlattice Vectors L_{M1} and L_{M2} are highlighted in green and blue respectively. The mark the basis for the (readily visible) large-scale hexagonal moire pattern.*

7.2.3 Interlayer hopping term

The interlayer hopping term can be defined by the matrix element,

$$T^{\alpha,\beta}_{\mathbf{k},\mathbf{k}'} = \langle\psi^{(1)}_{\mathbf{k},\alpha}|H_{\perp}|\psi^{(2)}_{\mathbf{k}',\beta}\rangle, \tag{7.5}$$

which describes a process where an electron with momentum $\mathbf{k}'$ in layer 2, sublattice β, hops to a momentum state $\mathbf{k}$ in layer 1, sublattice α. In the tight-binding approximation, we have

$$|\psi^{(1)}_{\mathbf{k},\alpha}\rangle = \frac{1}{\sqrt{N_1N_2}}\sum_{n_1,n_2} e^{i\mathbf{k}\cdot\left(\mathbf{R}^{(1)}_{n_1,n_2}+\boldsymbol{\delta}^{(1)}_{\alpha}\right)}|\mathbf{R}^{(1)}_{n_1,n_2}+\boldsymbol{\delta}^{(1)}_{\alpha},\alpha\rangle, \tag{7.6}$$

[1]We refer to a single graphene layer rotated by an arbitrary angle.

$$|\psi^{(2)}_{\mathbf{k}',\beta}\rangle = \frac{1}{\sqrt{N_1 N_2}} \sum_{n_1,n_2} e^{i\mathbf{k}'\cdot\left(\mathbf{R}^{(2)}_{n_1,n_2}+\boldsymbol{\delta}^{(2)}_{\beta}\right)} |\mathbf{R}^{(2)}_{n_1,n_2} + \boldsymbol{\delta}^{(2)}_{\beta}, \beta\rangle, \tag{7.7}$$

where

$$\boldsymbol{\delta}^{(1)}_{\alpha} = \boldsymbol{\delta}_{\alpha}, \quad \boldsymbol{\delta}^{(2)}_{\beta} = \boldsymbol{\delta}^{\theta}_{\beta}. \tag{7.8}$$

The following is the explicitly written interlayer hooping term and its matrix element of interest (which is, for now, completely general):

$$\begin{aligned} T^{\alpha,\beta}_{\mathbf{K}+\mathbf{q}_1,\mathbf{K}^\theta+\mathbf{q}_2} = \frac{1}{N_1 N_2} \sum_{n_1,n_2,n_1',n_2'} & e^{-i(\mathbf{K}+\mathbf{q}_1)\cdot\left(\mathbf{R}^{(1)}_{n_1,n_2}+\boldsymbol{\delta}^{(1)}_{\alpha}\right)} e^{i(\mathbf{K}^\theta+\mathbf{q}_2)\cdot\left(\mathbf{R}^{(2)}_{n_1',n_2'}+\boldsymbol{\delta}^{(2)}_{\beta}\right)} \\ & \times \langle \mathbf{R}^{(1)}_{n_1,n_2} + \boldsymbol{\delta}^{(1)}_{\alpha}, \alpha | H_\perp | \mathbf{R}^{(2)}_{n_1',n_2'} + \boldsymbol{\delta}^{(2)}_{\beta}, \beta \rangle. \end{aligned} \tag{7.9}$$

Within the continuum low-energy model, the above expression for the interlayer hopping can be simplified in a matrix notation where $T = \begin{pmatrix} T^{A,A} & T^{A,B} \\ T^{B,A} & T^{B,B} \end{pmatrix}$, we re-write the last expression as

$$T_{\mathbf{K}+\mathbf{q}_1,\mathbf{K}^\theta+\mathbf{q}_2^\theta} = T_{q_b}\delta_{\mathbf{q}_2^\theta,\mathbf{q}_1} + T_{q_{tr}}\delta_{\mathbf{q}_2^\theta,\mathbf{q}_1} + T_{q_u}\delta_{\mathbf{q}_2^\theta,\mathbf{q}_1}, \tag{7.10}$$

where

$$T_{q_b} = \frac{t_\perp(\mathbf{K})}{A_{u.c.}} T_1\,, \quad T_{q_{tr}} = \frac{t_\perp(\mathbf{K})}{A_{u.c.}} T_2\,, \quad T_{q_u} = \frac{t_\perp(\mathbf{K})}{A_{u.c.}} T_3, \tag{7.11}$$

$$T_1 = \begin{pmatrix} 1 & 1 \\ 1 & 1 \end{pmatrix}, \quad T_2 = e^{-i\phi}\begin{pmatrix} 1 & e^{i\phi} \\ e^{-i\phi} & 1 \end{pmatrix}, \quad T_3 = e^{i\phi}\begin{pmatrix} 1 & e^{-i\phi} \\ e^{i\phi} & 1 \end{pmatrix}, \quad \phi = \frac{2\pi}{3}, \tag{7.12}$$

and

$$\mathbf{q}_b = \mathbf{K} - \mathbf{K}^\theta\,, \quad \mathbf{q}_{tr} = (\mathbf{K}+\mathbf{b}_2) - (\mathbf{K}^\theta + \mathbf{b}_2^\theta)\,, \quad \mathbf{q}_{tl} = (\mathbf{K}-\mathbf{b}_1) - (\mathbf{K}^\theta - \mathbf{b}_1^\theta). \tag{7.13}$$

The interpretation of these results is more elegant when we move to the reference frame where layer 1 is rotated by $-\theta/2$ and layer 2 by $\theta/2$ (it suffices to rotate our previous coordinate system by $\theta/2$). Our demonstration was sufficiently general to allow us to do that, and we will stick to this reference frame from now on. The geometrical picture for this interlayer hopping is shown in fig. 2.10. The following relevant relations are also easily deduced in this reference frame:

$$\mathbf{q}_b = \frac{8\pi\sin(\theta/2)}{3\sqrt{3}d}(0,-1), \quad \mathbf{q}_{tr} = \frac{8\pi\sin(\theta/2)}{3\sqrt{3}d}(\sqrt{3}/2, 1/2), \quad \mathbf{q}_{tl} = \frac{8\pi\sin(\theta/2)}{3\sqrt{3}d}(-\sqrt{3}/2, 1/2), \tag{7.14}$$

[3] From now on, by convention, when we do not specify the rotation, we are always referring to anti-clockwise rotations by θ about the origin. Once again, translations do not affect anything at this point.

$$\mathbf{b}_1^m = \mathbf{q}_b - \mathbf{q}_{tl} = \frac{8\pi \sin(\theta/2)}{3d}(1/2, -\sqrt{3}/2), \quad \mathbf{b}_2^m = \mathbf{q}_{tr} - \mathbf{q}_b = \frac{8\pi \sin(\theta/2)}{3d}(1/2, \sqrt{3}/2), \tag{7.15}$$

$$\mathbf{a}_1^m = \frac{\sqrt{3}d}{2\sin(\theta/2)}(\sqrt{3}/2, -1/2), \quad \mathbf{a}_2^m = \frac{\sqrt{3}d}{2\sin(\theta/2)}(\sqrt{3}/2, 1/2), \tag{7.16}$$

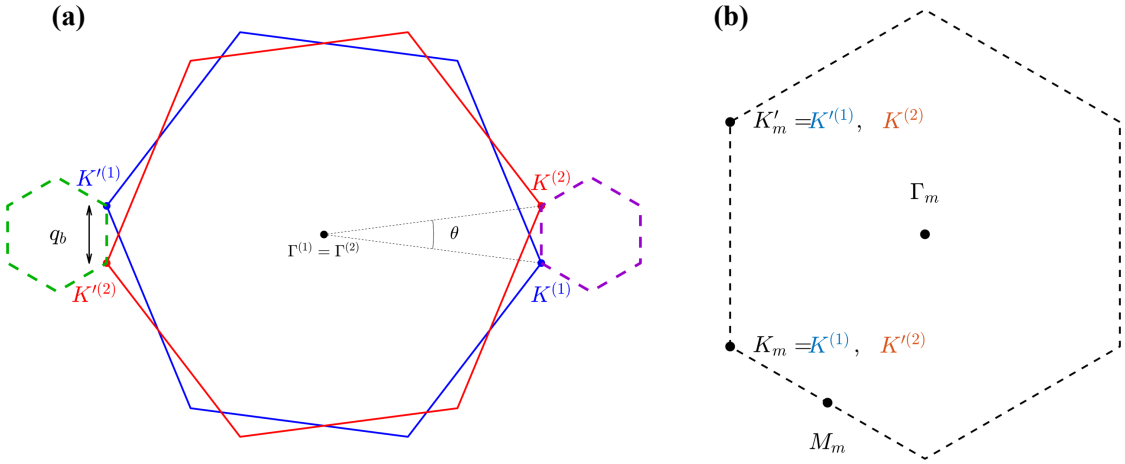

Figure 7.3: *K and K' bands on a tBLG. (a) Blue/red hexagons describe the BZs for layers 1/2. Dashed purple/green hexagons represent moire unit cells in reciprocal space for K/K' expansions. The vector q_b represents the shift due to twist and has the modulus of $2k_D \sin\theta$. (b) Moire BZ with relevant high-symmetry points plotted in it.*

7.2.4 Hamiltonian matrix construction

Let us briefly summarize the results and assumptions we have in our model for the tBLG. The total Hamiltonian for this material is splitted as

$$H = H_1 + H_2 + H_\perp. \tag{7.17}$$

In the tight-binding approximation, the wave functions read

$$|\psi_{\mathbf{k}}\rangle = \sum_{\alpha,i} c_\alpha^{(i)}(\mathbf{k})|\psi_{\mathbf{k},\alpha}^{(i)}\rangle, \tag{7.18}$$

where $c_\alpha^{(i)}(\mathbf{k})$ is a complex constant of unit modulus. In the continuum low-energy model and within a K expansion, we obtained the following non-null matrix elements for the interlayer hopping:

$$\langle\psi^{(1)}_{\mathbf{K}+\mathbf{q}_1,\alpha}|H_\perp|\psi^{(2)}_{\mathbf{K}^\theta+\mathbf{q}_2,\beta}\rangle = T^{\alpha,\beta}_{\mathbf{K}+\mathbf{q}_1,\mathbf{K}^\theta+\mathbf{q}_2} = T_{q_b}\delta_{\mathbf{q}_2-\mathbf{q}_1,\mathbf{q}_b} + T_{q_{tr}}\delta_{\mathbf{q}_2-\mathbf{q}_1,\mathbf{q}_{tr}} + T_{q_{tl}}\delta_{\mathbf{q}_2-\mathbf{q}_1,\mathbf{q}_{tl}}, \tag{7.19}$$

The remaining non-null matrix elements come from each single layer Dirac Hamiltonian,

$$\langle\psi^{(1)}_{\mathbf{K}+\mathbf{p}_1,\alpha}|H_1|\psi^{(1)}_{\mathbf{K}+\mathbf{p}_2,\beta}\rangle = H^{\alpha,\beta}_{\mathrm{SLG},K}(\mathbf{q}_1,-\theta/2)\delta_{\mathbf{p}_1,\mathbf{p}_2}, \tag{7.20}$$

$$\langle\psi^{(2)}_{\mathbf{K}^\theta+\mathbf{p}_1,\alpha}|H_2|\psi^{(2)}_{\mathbf{K}^\theta+\mathbf{p}_2,\beta}\rangle = H^{\alpha,\beta}_{\mathrm{SLG},K^\theta}(\mathbf{q}_2,\theta/2)\delta_{\mathbf{p}_1,\mathbf{p}_2}, \tag{7.21}$$

where $H^{\alpha,\beta}_{\mathrm{SLG},K}(\mathbf{q},\theta)$ is given by (2.71) (using the same matrix notation as we used for T) and $\mathbf{q}_i,\mathbf{p}_j$ are small enough to make the Dirac K-expansion valid.

In order to determine the electronic spectrum, we use the Schrödinger equation, which for our system reads

$$(H_1+H_2+H_\perp)|\psi_\mathbf{k}\rangle = E|\psi_\mathbf{k}\rangle. \tag{7.22}$$

Applying a bias $v^{(i)}_{k,\alpha}=(k,i,\alpha)$, as in SLG, does not yield a closed system. Starting from $\langle K+q,1|$, we couple (besides the diagonal term) to $|K^\theta+q+q_b,2\rangle$, $|K^\theta+q+q_{tr},2\rangle$, and $|K^\theta+q+q_{tl},2\rangle$ (first NN in reciprocal space). Each of these couples to the previous one and to two new states (second NN), and the process repeats.

Let us clarify the matrix construction by showing examples. If we start with the $\langle K+q,1|$ and consider just first NN, we obtain

$$H^K(q)\begin{pmatrix} c^{(1)}_A(K+q)\\ c^{(1)}_B(K+q)\\ c^{(2)}_A(K^\theta+q+q_b)\\ c^{(2)}_B(K^\theta+q+q_b)\\ c^{(2)}_A(K^\theta+q+q_{tr})\\ c^{(2)}_B(K^\theta+q+q_{tr})\\ c^{(2)}_A(K^\theta+q+q_{tl})\\ c^{(2)}_B(K^\theta+q+q_{tl})\end{pmatrix} = E^K(q)\begin{pmatrix} c^{(1)}_A(K+q)\\ c^{(1)}_B(K+q)\\ c^{(2)}_A(K^\theta+q+q_b)\\ c^{(2)}_B(K^\theta+q+q_b)\\ c^{(2)}_A(K^\theta+q+q_{tr})\\ c^{(2)}_B(K^\theta+q+q_{tr})\\ c^{(2)}_A(K^\theta+q+q_{tl})\\ c^{(2)}_B(K^\theta+q+q_{tl})\end{pmatrix} \tag{7.23}$$

where

$$H^K_{BLG}(q)=\begin{bmatrix} H^K_{SLG}(q,-\theta/2) & T_{q_b} & T_{q_{tr}} & T_{q_{tl}}\\ T^\dagger_{q_b} & H^K_{SLG}(q+q_b,\theta/2) & 0 & 0\\ T^\dagger_{q_{tr}} & 0 & H^K_{SLG}(q+q_{tr},\theta/2) & 0\\ T^\dagger_{q_{tl}} & 0 & 0 & H^K_{SLG}(q+q_{tl},\theta/2)\end{bmatrix} \tag{7.24}$$

Without further low-energy approximations, we thus see that the minimum matrix Hamiltonian

for the tBLG is 8×8. Instead of writting the whole system of equations, we can compress and interpret it by using the following convenient picture for the K-Hamiltonian matrix elements:

It is possible to demonstrate analytically (see Appendix E.1 for information) that this Hamiltonian has two zero energy states at $k = 0$, and a Dirac velocity gets renormalized. And it can be shown that

$$\frac{v^\star}{v} = \frac{1 - 3\alpha^2}{1 + 6\alpha^2}. \tag{7.25}$$

where

$$\alpha = \frac{w}{v_F \cdot |q_b|} = \frac{w}{v_F \cdot 2k_D \sin(\theta/2)}, \tag{7.26}$$

The denominator in equation (7.25) captures the contribution of the j's to the normalization of the wave function, while the numerator captures their contribution to the velocity matrix elements. For small α, equation (7.25) reduces to the expression $v^\star/v = 1 - 9\alpha^2$, first obtained by Santos *et al.* [134]. The velocity vanishes at the first magic angle because it is in the process of changing sign. The eigenstates at the Dirac point are a coherent combination of components in the two layers that have velocities of opposite sign.

7.2.5 The Chiral Hamiltonian

Continuum Hamiltonian of Twisted Bilayer Graphene can also be expressed as below

$$\begin{aligned} H &= H_1 + H_2 + H_\perp \\ &= \hbar v_F \sum_{k,\alpha,\beta} \left[\phi^\dagger_{1,k,\alpha}\, \tau^{-\theta/2}_{\alpha\beta}\big(\mathbf{k} + \tfrac{\mathbf{K}}{2}\big)\, \phi_{1,k,\beta} + \phi^\dagger_{2,k,\alpha}\, \tau^{+\theta/2}_{\alpha\beta}\big(\mathbf{k} - \tfrac{\mathbf{K}}{2}\big)\, \phi_{2,k,\beta} \right] \\ &\quad + t_\perp \sum_{k,\mathbf{G},\alpha,\beta} \left[\phi^\dagger_{1,k+\mathbf{G},\alpha}\, T_{\alpha\beta}(\mathbf{G})\, \phi_{2,k,\beta} + \text{H.c.} \right] \end{aligned} \tag{7.27}$$

and the T-matrices could be written as below:

$$T_1 = \begin{pmatrix} w_{AA} & w_{AB} \\ w_{AB} & w_{AA} \end{pmatrix}, \quad T_2 = \begin{pmatrix} w_{AA} & w_{AB}e^{-2\pi i/3} \\ w_{AB}e^{2\pi i/3} & w_{AA} \end{pmatrix}, \quad T_3 = T_2^\dagger. \tag{S38}$$

The general form would

$$T_{\alpha\beta} = w_{AA} + w_{AB}\, (\hat{\mathbf{z}} \times \hat{\mathbf{q}}_{\alpha\beta}) \cdot \boldsymbol{\sigma}, \tag{S39}$$

where $\hat{\mathbf{q}}_\alpha = \mathbf{q}_\alpha / k_\theta$ is the unit vector along the direction of $\mathbf{q}_\alpha$. It is convenient to rotate the basis to

transform the Hamiltonian as

$$H \;\rightarrow\; \begin{pmatrix} e^{i\frac{\pi}{4}\sigma_z} & 0 \\ 0 & e^{-i\frac{\pi}{4}\sigma_z} \end{pmatrix} H \begin{pmatrix} e^{-i\frac{\pi}{4}\sigma_z} & 0 \\ 0 & e^{i\frac{\pi}{4}\sigma_z} \end{pmatrix} = \begin{pmatrix} -iv_0\boldsymbol{\sigma}\cdot\nabla & T_\theta(\mathbf{G}) \\ T_\theta^\dagger(\mathbf{G}) & -iv_0\boldsymbol{\sigma}\cdot\nabla \end{pmatrix}, \tag{S40}$$

where

$$T_\theta(\mathbf{G}) = \sum_a T^\theta_{\alpha\beta}\, e^{-i\mathbf{q}_a\cdot\mathbf{G}}, \quad T^\theta_{\alpha\beta} = w_{AA} e^{i\frac{\theta}{2}\sigma_z} + w_{AB}\,(\hat{\mathbf{z}}\times\hat{\mathbf{q}}_{\alpha\beta})\cdot\boldsymbol{\sigma}. \tag{7.28}$$

This unitary rotation makes leads to $\tau^{\pm\theta/2}_{\alpha\beta} \rightarrow \tau_{\alpha\beta}$; and in the chiral limit $w_{AA} = 0$,

$$T^{\text{chiral}}_{\alpha\beta}(\mathbf{G}) = w_{AB}\,(\hat{z}\times\mathbf{q}_G)\cdot\boldsymbol{\sigma}. \tag{7.29}$$

$$\begin{aligned} H_{\text{chiral}} &= H_1 + H_2 + H_\perp \\ &= \hbar v_F \sum_{k,\alpha,\beta} \Big[\phi^\dagger_{1,k,\alpha}\,\tau_{\alpha\beta}\big(\mathbf{k}+\tfrac{\mathbf{K}}{2}\big)\,\phi_{1,k,\beta} + \phi^\dagger_{2,k,\alpha}\,\tau_{\alpha\beta}\big(\mathbf{k}-\tfrac{\mathbf{K}}{2}\big)\,\phi_{2,k,\beta}\Big] \\ &\quad + t_\perp \sum_{k,\mathbf{G},\alpha,\beta} \Big[\phi^\dagger_{1,k+\mathbf{G},\alpha}\,T^{\text{chiral}}_{\alpha\beta}(\mathbf{G})\,\phi_{2,k,\beta} + \text{H.c.}\Big] \end{aligned} \tag{7.30}$$

7.3 Algorithm Development and Band-Structure analysis at different twist angles

A detailed examination of Fig. 7.3 reveals the schematic representation of the Moiré Brillouin Zone (MBZ) for twisted bilayer graphene (TBG). There are two in-equivalent valleys as it can be seen from the ; which corresponds to the K and K' valleys of the MBZ. In Fig. 7.4(a) we focus on the right valley, the red and blue markers correspond to the inequivalent Dirac points originating from the two graphene layers, which are stacked and rotated relative to each other by the twist angle θ. The finite separation between these two Dirac points in reciprocal space directly encodes the twist and is quantitatively equal to the magnitude of the Moiré reciprocal lattice vector q_b, as defined in Eq. (7.14). This vector not only characterizes the periodicity of the Moiré superlattice in momentum space but also coincides with the direction along which the perpendicular interlayer tunneling process occurs, mediated by the coupling matrix T_1.

For reference, in the chosen coordinate convention of the figure, the vertical axis corresponds to the k_x direction, while the horizontal axis is aligned with k_y. The high-symmetry points of the MBZ and their relative positions are thus conveniently expressed in this (k_x, k_y) basis. Furthermore,

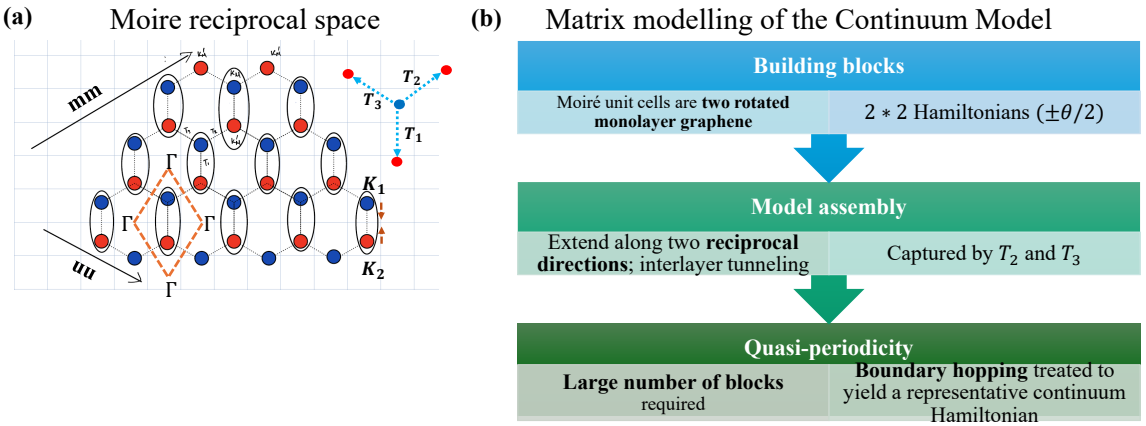

Figure 7.4: ***(a)*** *The oval shaped enclosures are consist of two Dirac points from the top and the bottom layers separated by twist. Each site is* 4×4 *matrix following the continuum model of TBG.* ***(b)*** *The matrix modeling procedure for twisted bilayer graphene (TBG). The construction begins with two rotated graphene monolayers forming the moiré unit cell, each described by a* 2×2 *Dirac Hamiltonian at angles* $\pm\theta/2$ *coupled by* T_1*. These blocks are extended along the two reciprocal lattice directions (mm & nn) and coupled through interlayer tunneling matrices* T_2 *and* T_3*. To capture the quasi-periodic nature of the moiré pattern, a large number of such blocks are included, with boundary hopping terms incorporated to yield an effective continuum Hamiltonian.*

the tunneling matrices that arise from the Fourier expansion of the interlayer hopping Hamiltonian, as described in Eq. (7.12), are illustrated in the inset located at the top right corner of the figure. These matrices, T_1, T_2, and T_3, capture the momentum-dependent coupling between the layers and play a central role in shaping the low-energy band structure of TBG.

To construct the continuum model for twisted bilayer graphene (TBG) starting from the underlying quasi-periodic Moiré lattice, we begin by identifying the fundamental repeating units that serve as the computational building blocks. These are represented by the oval-shaped regions highlighted in Fig. 7.4(a). Each block contains two monolayer graphene Hamiltonians, where the respective layers are rotated by $\pm\theta/2$ relative to a common reference frame. This symmetric rotation ensures a net relative twist angle of θ between the two layers, preserving the rotational symmetry of the bilayer configuration.

The assembly of the continuum model proceeds by periodically extending these basic blocks along two principal reciprocal-space directions, labeled here as the *mm*- and *nn*-directions. The intra-block physics is governed solely by the monolayer Dirac Hamiltonians (appropriately rotated), while inter-block couplings arise from interlayer tunneling processes. Specifically, the hopping matrix T_2 connects neighboring blocks along the *mm*-direction, and T_3 connects neighboring blocks along the *nn*-direction. These tunneling matrices encode the momentum-independent coupling between states in adjacent blocks, as dictated by the Moiré periodicity.

Because the Moiré superlattice is quasi-periodic rather than strictly periodic in the original graphene Brillouin zone, it is necessary to include a sufficiently large number of such blocks in the computational domain to capture the essential low-energy physics. In practice, we consider a total of L sites in the model, arranged to fully incorporate both types of couplings ($MMNN$) in the bulk of the structure. At the boundaries, however—specifically along the $LLNN$ and $MMLL$ edges—we only retain a single set of inter-block hoppings, in accordance with the geometric constraints of the truncated lattice, as illustrated schematically in Fig. 7.4(b). This construction yields a finite yet physically representative realization of the continuum Hamiltonian for TBG, enabling accurate calculation of its electronic structure.

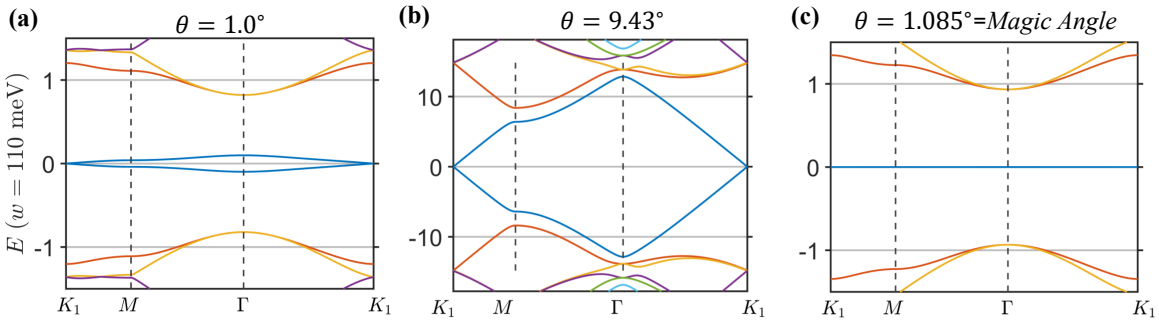

Figure 7.5: *Bandstrcuture of Chiral Twisted Bilayer Graphene at different twist angles.* ***(a-c)*** *The band dispersions at twist angles $\theta = 1.00°$, $\theta = 9.43°$ and $\theta = 1.085°$: the Magic angle; along the high-symmetry path $K_1 - M - \Gamma - K_1$. At K-points we have Dirac crossings except when we have flat bands.*

7.4 Band-topology with External Fields

The application of external fields offers a versatile handle for engineering band topology in two-dimensional materials. In monolayer and AB-stacked bilayer graphene, it is well established that perpendicular electric fields and magnetic fields can drive exotic transitions, often accompanied by gap openings and symmetry breaking. In twisted bilayer graphene (TBG), however, the interplay between Moiré band structure, twist angle, and external perturbations introduces qualitatively different responses. This section systematically examines the effect of purely in-plane magnetic fields, purely in-plane electric fields, and their combined (crossed-field) configuration, with the aim of identifying possible routes toward inducing an insulator–metal transition in small-angle TBG. Our analysis reveals that, unlike its untwisted counterparts, TBG does not exhibit the conventional gap-opening mechanisms under these conditions, and the resulting band reconstructions suggest fundamental limitations for realizing such a transition within this platform.

7.4.1 Effect of only in-plane magnetic field

We first investigate how an in-plane magnetic field modifies the band topology of small-angle TBG. The application of a sufficiently strong in-plane field transforms the low-energy band dispersion from linear Dirac-like cones into parabolic bands at a critical field strength (ϕ_M) (Fig. (7.6)), in agreement with the theoretical predictions of Kwan et al. [132]. The resulting two-band parabolic dispersion belongs to the class described by Montambaux et al. [135], in which the merging of Dirac points under perturbations does not result in the opening of a gap. Physically, the in-plane field effectively cancels the relative momentum shift induced by the twist angle, bringing the two Dirac cones into coincidence without triggering mass generation. This gapless parabolic state, while topologically distinct from the original Dirac bands, therefore cannot be leveraged to realize a conventional insulating phase.

7.4.2 Effect of only out-of-plane electric field

We next consider the application of an out-of-plane electric field. Previous results in this system, such as those reported by [134]et al., show that gap opening is not possible. In our work we see the similar effect, in TBG, our numerical simulations reveals no gap opening is observed, and we argue that the response is instead reminiscent of monolayer graphene. This similarity to the monolayer case further supports the view that, despite the Moiré-physics, the dominant low-energy excitations in TBG remain effectively massless under in-plane electric fields.

7.4.3 Effect of crossed field setup

We now examine the effect of a purely out-of-plane electric field on TBG. Earlier studies, such as those by Santos et al. [134], have reported that such a perturbation does not induce a gap in this system. Our numerical results are fully consistent with these findings: the application of an out-of-plane electric field leaves the low-energy spectrum gapless. The observed response closely mirrors that of monolayer graphene, where the field merely shifts the band energies without generating mass terms. This resemblance suggests that, despite the presence of Moiré-induced band reconstruction, the low-energy excitations in TBG remain effectively massless under out-of-plane electric fields.

7.4.4 Combined in-plane magnetic and electric fields

Finally, we examine the case of crossed in-plane magnetic and electric fields, motivated by our earlier work in which such configurations were proposed as potential routes to drive insulator-metal

transitions. In TBG, once the parabolic dispersion is achieved with the critical in-plane field we expected a similar behaviour alike the AB-stacked untwisted case, however, the combined perturbation again fails to induce a gap. The band structure remains predominantly linear in character, suggesting that the mechanisms responsible for the insulator–metal transition in AB-stacked bilayer graphene cannot be straightforwardly transplanted to the Moiré case. This leads us to conclude that small-angle TBG, at least within the range of experimentally feasible field strengths, is not an ideal platform for realizing such a transition. Instead, our findings indicate that systems hosting parabolic Moiré bands—such as twisted double bilayer graphene—may offer a more promising route toward field-driven topological and metal–insulator transitions, due to their greater propensity for gap formation under similar perturbations.

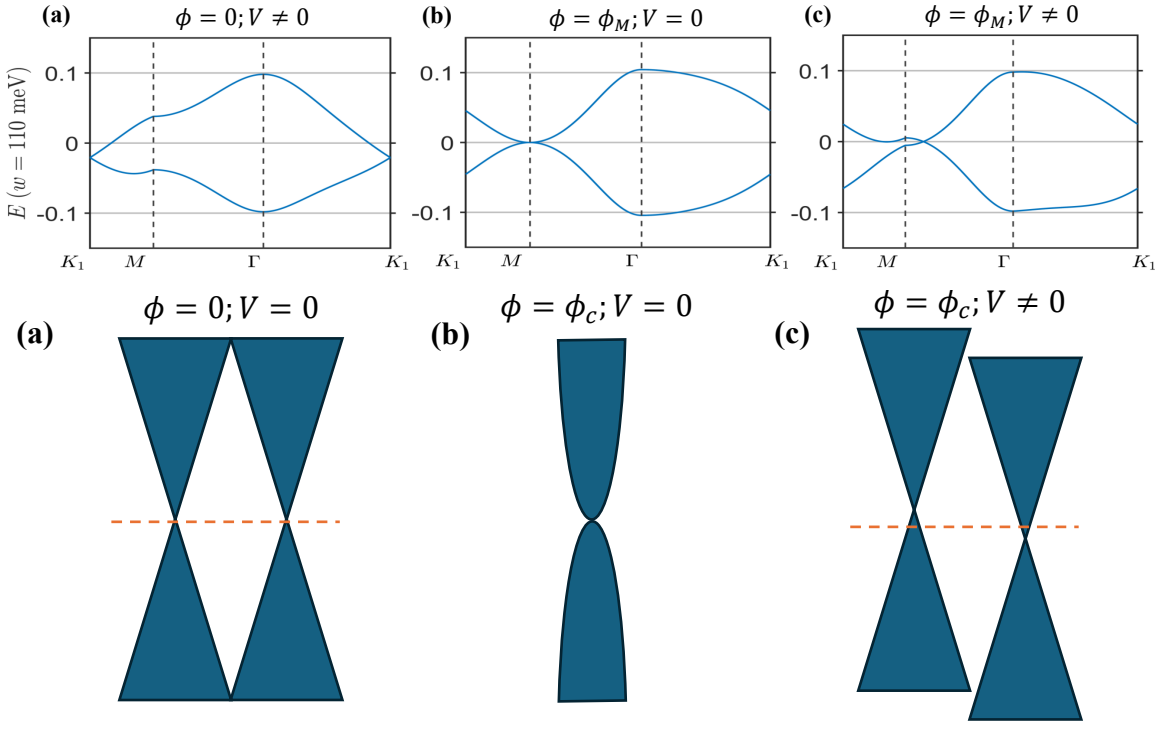

Figure 7.6: ***Top row:*** *Band structure of chiral twisted bilayer graphene under various crossed-field configurations.* ***(a)*** *With no in-plane magnetic field, applying a transverse electric field to the linear Dirac crossings produces no gap.* ***(b)*** *At the critical in-plane magnetic field ϕ_M, where the Dirac bands acquire a parabolic dispersion, a transverse electric field still fails to open a gap.* ***Bottom row:*** ***(a–c)*** *For a small twist angle, the linear-to-parabolic transition occurs as expected, yet the bands remain gapless across all field configurations.*

7.5 Interesting Directions and Promises

The absence of an insulator–metal transition in TBG under external fields, while initially unexpected, opens an equally intriguing path: probing the linear response of parabolic dispersion regimes near the critical field. Such a regime offers a fertile ground to explore emergent quantum phenomena, where small perturbations may strongly influence correlated states. Measurements of transport coefficients, compressibility, and magneto-electric responses in this limit could reveal subtle ordering tendencies or hidden criticality, even in the absence of a conventional gap opening.

Connection to Superconductivity Suppression: A particularly promising avenue lies in connecting the field-induced evolution of band structure to the suppression of superconductivity. In TBG, superconductivity is highly sensitive to the geometry of the electronic wavefunctions, and in-plane magnetic fields can modify this geometry through changes in the Berry curvature distribution. By systematically mapping superconducting critical currents as a function of both in-plane and out-of-plane magnetic fields, it becomes possible to disentangle orbital contributions from spin effects. This, in turn, may clarify whether pairing in TBG is mediated predominantly by quantum geometric mechanisms rather than conventional electron–phonon or spin-fluctuation routes.

Extending to Twisted Double-Bilayer Graphene: The framework developed here naturally extends to twisted double-bilayer graphene (TDBG) [107], a system with an enlarged Moiré Brillouin zone and intrinsically parabolic low-energy dispersion. Unlike TBG, TDBG is expected to exhibit insulator–metal transitions at comparatively modest field strengths, making it a more accessible platform for exploring orbital magnetism and field-tuned correlated phases. These properties position TDBG as a promising candidate for experimentally probing exotic magnetic responses and for testing theoretical predictions in a regime where Moiré physics and parabolic band topology coexist.

Outlook: Taken together, these findings suggest that while TBG may not be ideal for realizing an insulator–metal transition under external fields, it remains an exceptional platform for studying the interplay between flat-band topology, orbital magnetism, and superconductivity. Moving forward, targeted investigations in both TBG and TDBG could bridge the gap between microscopic band-structure modifications and macroscopic correlated phases, paving the way for a deeper understanding of quantum geometry–driven phenomena in Moiré materials. This chapter thus sets the stage for the broader conclusions and future perspectives that follow.

Chapter 8

CONCLUSION & FUTURE DIRECTIONS

8.1 Summary and Conclusion

The work presented in this dissertation has explored the rich interplay between symmetry, external fields, and electronic structure in two-dimensional materials, with an emphasis on systems where topology, correlation, and lattice geometry converge to produce unconventional phenomena. Motivated by the desire to understand and control quantum phases through symmetry engineering, we have examined a series of platforms—ranging from nonsymmorphic Dirac semimetals to Bernal-stacked and twisted bilayer graphene—each chosen for their unique capacity to host tunable band structures and exotic responses.

Beginning with nonsymmorphic Dirac semimetals, we identified how crystalline symmetries protect Dirac crossings and govern magneto-optical selection rules. By developing a current–current response formalism, we predicted quantized plateaus in Faraday rotation under magnetic fields, establishing a direct connection between symmetry constraints and measurable optical signatures. In Bernal-stacked bilayer graphene, we mapped the evolution of band dispersion under crossed electric and magnetic fields, revealing conditions for a metal–insulator transition and elucidating its imprint on orbital magnetic susceptibility. Extending this framework to include trigonal warping demonstrated that subtle band-structure distortions can substantially lower the field threshold for the transition, offering new levers for experimental realization.

In the case of small-angle twisted bilayer graphene, we built the continuum model from first principles, capturing the formation of the Moiré Brillouin zone, the renormalization of Fermi velocity, and the emergence of flat bands at the magic angles in the chiral limit. Our initial goal of probing the metal–insulator transition in this setting led instead to a surprising conclusion: within the regimes explored, twisted bilayer graphene does not support the anticipated transition. This finding, grounded

in both theoretical analysis and numerical benchmarks, underscores the importance of re-evaluating prevailing assumptions and motivates a search for alternative mechanisms in related systems.

Across these studies, a unifying theme emerges: symmetry, band geometry, and external perturbations act in concert to shape the quantum phases and optical responses of 2D materials. The theoretical frameworks, computational tools, and predictive results developed here form a coherent foundation for future explorations, both in the specific materials examined and in broader classes of engineered quantum systems.

This foundation naturally shapes the outlook of this work. Building on the insights from twisted bilayer graphene, introducing strain offers a promising route to break residual symmetries and tune the flat-band geometry, making it essential to compute the linear response and Drude weight to assess transport anisotropies. In parallel, the interplay of flat-band physics with altermagnetic order in intercalated Kagome materials presents a fertile ground for uncovering spin–momentum locked phases with strong quantum-geometric enhancement, guiding both spectroscopic and transport probes. Finally, the challenges of strongly correlated electron systems motivate the quantum simulation of the Fermi–Hubbard model, enabling controlled exploration of correlated phases beyond classical computational limits. Together, these directions extend the scope of this dissertation from understanding existing systems to actively engineering and emulating novel quantum matter.

8.2 Twisted Multilayer Systems and its Linear Response Under External Fields and Mechanical Strain

Two-dimensional materials have revolutionized condensed matter physics since the isolation of graphene in 2004 [1]. Graphene's hexagonal carbon lattice combines remarkable mechanical strength with exceptional thermal and electrical conductivity [136].

A paradigm shift arrived in 2018 with the discovery of correlated insulators and superconductivity in twisted bilayer graphene (TBG) near the "magic" twist angle of $\sim 1.1^\circ$ [14, 15].

Although twist angle remains the principal tuning knob, recent work has begun to explore the role of lattice strain in modifying moiré physics [137]. Strain can mimic in-plane magnetic fields, break crystal symmetries, and alter charge distributions, yet a quantitative link between strain, quantum geometry, and superconducting response is still missing. Furthermore, strain can mimic in-plane magnetic fields, break crystal symmetries, and alter charge distributions, yet a quantitative link between strain, quantum geometry, and superconducting response is still missing. Strain thus

expands the space of accessible moiré patterns (the emerging field of "twistronics") and can strongly affect quantum geometry, symmetry breaking, and ultimately superconducting response.

My proposal is to establish a unified theoretical framework to predict and control correlated superconductivity in TBG via strain engineering. Despite recent advances, I would like to answer the critical questions that remain open: (i) *Symmetry-Property Relationships:* How does strain-induced C_3 symmetry breaking suppress superconductivity through quantum geometric modifications? (ii) *Universal Control Principle:* Can strain be established as a fundamental tuning knob that transcends conventional material constraints? (iii) *Quantum Material Design:* What predictive principles govern strain-programmable quantum phases in twisted multilayer graphene and related moiré systems?

Looking forward, an important direction is to establish strain as a precise control knob for engineering the quantum geometry of moiré materials. In flat-band systems such as twisted bilayer graphene, superconductivity is shaped not only by band dispersion but also by the geometry of electronic wavefunctions, quantified by the quantum metric. By computing the superfluid stiffness and its strain dependence, a predictive framework can be developed that directly links lattice deformations to superconducting and topological responses. Such an approach would elevate the quantum metric from a theoretical construct to a practical design variable, enabling on-demand realization of novel phases—ranging from high-T_c superconductivity to strain-stabilized topological states—and guiding the transition of twistronics from empirical discovery to predictive quantum material design.

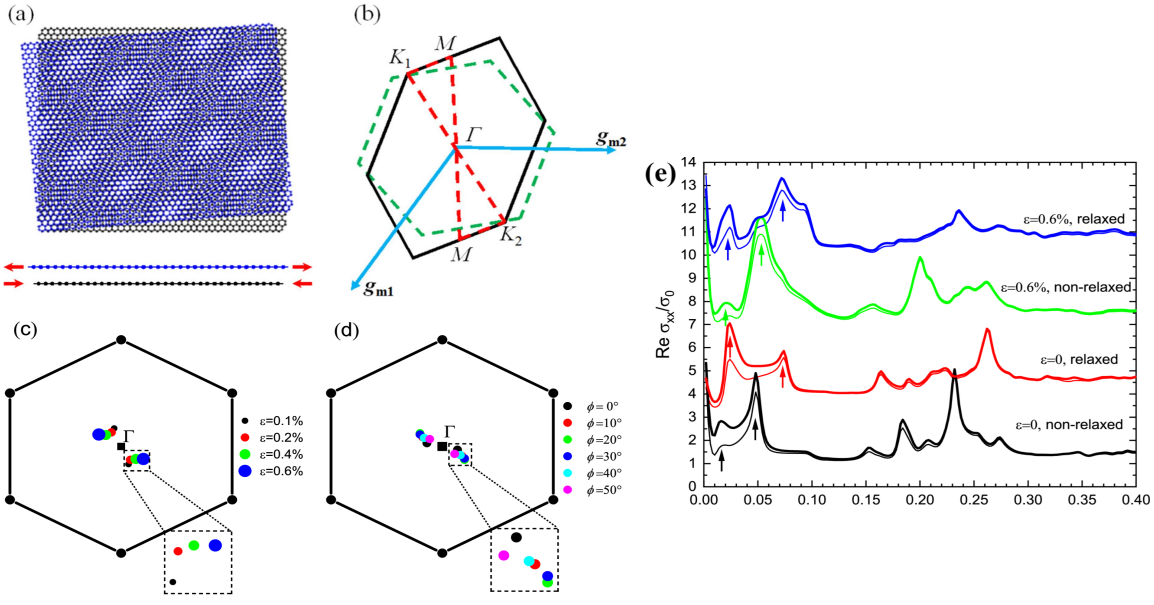

Figure 8.1 *Figure 2* ***Strain effects in TBG.*** *(a) Armchair uniaxial strain (red arrows). (b) Strained (solid) vs. unstrained (dashed) moiré Brillouin zones. (c) Dirac point shifts vs. strain magnitude ($\phi = 30°$). (d) Dirac trajectories vs. strain direction ($\varepsilon = 0.6\%$). (e) Optical conductivity peaks under four strain configurations (Dai et al. 2021).*

8.3 Quantum Simulation of Condensed Matter Systems: Outlook toward Predictive Design

A central long-term goal of this thesis is to bridge quantum materials science and quantum computation to enable predictive design of strongly correlated matter. The previous chapters focused on emergent orders in twisted bilayer graphene and intercalated kagome metals, systems where strong correlations and unconventional magnetism drive novel phases. A key outlook is to develop scalable simulation tools capable of capturing such correlated states directly on quantum hardware.

Quantum computation provides a fundamentally new route for this challenge. Classical methods such as exact diagonalization, DMRG, or quantum Monte Carlo are limited by exponential Hilbert space growth or sign problems. By contrast, quantum computers can naturally encode many-body Hilbert spaces, making them ideally suited for paradigmatic models of correlated electrons. The Fermi–Hubbard model,

$$\mathcal{H}_{\mathrm{FH}} = -t \sum_{\langle i,j\rangle,\sigma} (c^{\dagger}_{i\sigma} c_{j\sigma} + \mathrm{h.c.}) + U \sum_{i} n_{i\uparrow} n_{i\downarrow},$$

serves as a minimal yet challenging model: it hosts metal–insulator transitions, magnetism, and possibly pairing phenomena relevant to high-T_c cuprates.

As an initial step, I am implementing the Fermi–Hubbard model on current IBM quantum processors using two complementary algorithms: the Variational Quantum Eigensolver (VQE), and the Sample-based Quantum Diagonalization (SQD) approach. The VQE offers a flexible ansatz-based framework, while SQD provides an alternative route that may prove more scalable for extracting low-energy spectra. Benchmarking both against classical exact diagonalization for small chains and ladders establishes a foundation for systematic quantum simulation of correlated systems.

Looking forward, the ultimate aim is to extend these approaches to larger ladder geometries and eventually to two-dimensional lattices where classical approaches fail. Such progress would open the door to probing pairing correlators, superconducting tendencies, and exotic quantum phases in silico, thus connecting computational quantum simulation with real materials such as graphene moiré systems and kagome magnets. In this way, quantum computation can evolve from a benchmarking tool into a predictive platform for designing and understanding correlated quantum materials.

BIBLIOGRAPHY

[1] K. S. Novoselov, A. K. Geim, S. V. Morozov, D. Jiang, Y. Zhang, S. V. Dubonos, I. V. Grigorieva, and A. A. Firsov, Science **306**, 666 (2004).

[2] K. S. Novoselov, A. K. Geim, S. V. Morozov, D. Jiang, M. I. Katsnelson, I. V. Grigorieva, S. V. Dubonos, and A. A. Firsov, Nature **438**, 197 (2005).

[3] K. S. Novoselov and A. H. Castro Neto, Physica Scripta **2012**, 014006 (2012).

[4] A. K. Geim and A. H. MacDonald, Physics Today **60**, 35 (2007), https://pubs.aip.org/physicstoday/article-pdf/60/8/35/9878274/35_1_online.pdf .

[5] P. J. Kowalczyk, S. A. Brown, T. Maerkl, Q. Lu, C.-K. Chiu, Y. Liu, S. A. Yang, X. Wang, I. Zasada, F. Genuzio, T. O. MenteÅŸ, A. Locatelli, T.-C. Chiang, and G. Bian, ACS Nano **14**, 1888 (2020), pMID: 31971774, https://doi.org/10.1021/acsnano.9b08136 .

[6] C. L. Kane and E. J. Mele, Phys. Rev. Lett. **95**, 226801 (2005).

[7] S. M. Young and C. L. Kane, Phys. Rev. Lett. **115**, 126803 (2015).

[8] B. J. Wieder and C. L. Kane, Phys. Rev. B **94**, 155108 (2016).

[9] S. Guan, Y. Liu, Z.-M. Yu, S.-S. Wang, Y. Yao, and S. A. Yang, Phys. Rev. Mater. **1**, 054003 (2017).

[10] F. Reis, G. Li, L. Dudy, M. Bauernfeind, S. Glass, W. Hanke, R. Thomale, J. Schäfer, and R. Claessen, Science **357**, 287 (2017).

[11] A. K. Geim and I. V. Grigorieva, Nature **499**, 419 (2013).

[12] E. McCann and M. Koshino, Reports on Progress in Physics **76**, 056503 (2013).

[13] J. M. B. Lopes dos Santos, N. M. R. Peres, and A. H. Castro Neto, Phys. Rev. B **86**, 155449 (2012).

[14] R. Bistritzer and A. H. MacDonald, Proceedings of the National Academy of Sciences of the USA **108**, 12233 (2011).

[15] Y. Cao, V. Fatemi, S. Fang, K. Watanabe, T. Taniguchi, E. Kaxiras, and P. Jarillo-Herrero, Nature **556**, 43 (2018).

[16] I. Brihuega, P. Mallet, H. González-Herrero, G. Trambly de Laissardière, M. M. Ugeda, L. Magaud, J. M. Gómez-Rodríguez, F. Ynduráin, and J.-Y. Veuillen, Phys. Rev. Lett. **109**, 196802 (2012).

[17] M. Z. Hasan and C. L. Kane, Rev. Mod. Phys. **82**, 3045 (2010).

[18] S. M. Young, S. Zaheer, J. C. Y. Teo, C. L. Kane, E. J. Mele, and A. M. Rappe, Phys. Rev. Lett. **108**, 140405 (2012).

[19] B. Yan and C. Felser, Annual Review of Condensed Matter Physics **8**, 337 (2017), https://doi.org/10.1146/annurev-conmatphys-031016-025458 .

[20] N. Nagaosa, T. Morimoto, and Y. Tokura, Nature Reviews Materials **5**, 621 (2020).

[21] S. Cahangirov, M. Topsakal, E. Aktürk, H. Şahin, and S. Ciraci, Phys. Rev. Lett. **102**, 236804 (2009).

[22] P. Vogt, P. De Padova, C. Quaresima, J. Avila, E. Frantzeskakis, M. C. Asensio, A. Resta, B. Ealet, and G. Le Lay, Phys. Rev. Lett. **108**, 155501 (2012).

[23] S. Z. Butler, S. M. Hollen, L. Cao, Y. Cui, J. A. Gupta, H. R. Gutiérrez, T. F. Heinz, S. S. Hong, J. Huang, A. F. Ismach, E. Johnston-Halperin, M. Kuno, V. V. Plashnitsa, R. D. Robinson, R. S. Ruoff, S. Salahuddin, J. Shan, L. Shi, M. G. Spencer, M. Terrones, W. Windl, and J. E. Goldberger, ACS Nano **7**, 2898 (2013), pMID: 23464873, https://doi.org/10.1021/nn400280c .

[24] H. Liu, A. T. Neal, Z. Zhu, Z. Luo, X. Xu, D. Tománek, and P. D. Ye, ACS Nano **8**, 4033 (2014), pMID: 24655084, https://doi.org/10.1021/nn501226z .

[25] S. M. Young and C. L. Kane, Phys. Rev. Lett. **115**, 126803 (2015).

[26] S. Deng, L. Li, and Y. Zhang, ACS Applied Nano Materials **1**, 1932 (2018), https://doi.org/10.1021/acsanm.8b00363 .

[27] L. Xu, W.-Q. Huang, W. Hu, K. Yang, B.-X. Zhou, A. Pan, and G.-F. Huang, Chemistry of Materials **29**, 5504 (2017), https://doi.org/10.1021/acs.chemmater.7b00281 .

[28] X. Zhao, B. Qiu, W. Yue, G. Hu, J. Ren, and X. Yuan, The European Physical Journal B **92**, 44 (2019).

[29] J. Cui, Z. Zhang, D. Liu, D. Zhang, W. Hu, L. Zou, Y. Lu, C. Zhang, H. Lu, C. Tang, N. Jiang, I. P. Parkin, and D. Guo, Nano Letters **19**, 6569 (2019), pMID: 31381357, https://doi.org/10.1021/acs.nanolett.9b02821 .

[30] S. Guan, Y. Liu, Z.-M. Yu, S.-S. Wang, Y. Yao, and S. A. Yang, Phys. Rev. Materials **1**, 054003 (2017).

[31] K.-H. Jin, H. Huang, Z. Wang, and F. Liu, Nanoscale **11**, 7256 (2019).

[32] M. I. Katsnelson, Graphene: Carbon in Two Dimensions (Cambridge University Press, 2012).

[33] A. Kumar, G. Sachdeva, R. Pandey, and S. P. Karna, Applied Physics Letters **116**, 263102 (2020), https://doi.org/10.1063/5.0010794 .

[34] T. Jiang, D. Huang, J. Cheng, X. Fan, Z. Zhang, Y. Shan, Y. Yi, Y. Dai, L. Shi, K. Liu, C. Zeng, J. Zi, J. E. Sipe, Y.-R. Shen, W.-T. Liu, and S. Wu, Nature Photonics **12**, 430 (2018).

[35] L. Van Hove, Phys. Rev. **89**, 1189 (1953).

[36] E. H. Hwang and S. Das Sarma, Phys. Rev. B **77**, 195412 (2008).

[37] Y. Zhan, Two distinct methods to evaluate graphene relaxation time and mobility in boltzmann diffusive transport, considering ionized impurity scattering and thomas-fermi screening (2017), arXiv:1712.08965 [cond-mat.mes-hall] .

[38] A. Chakraborty, G. Bian, and G. Vignale, Phys. Rev. B **105**, 085101 (2022).

[39] K.-H. Jin, H. Huang, Z. Wang, and F. Liu, Nanoscale **11**, 7256 (2019).

[40] L. M. Schoop, A. Topp, J. Lippmann, F. Orlandi, L. Müchler, M. G. Vergniory, Y. Sun, A. W. Rost, V. Duppel, M. Krivenkov, S. Sheoran, P. Manuel, A. Varykhalov, B. Yan, R. K. Kremer, C. R. Ast, and B. V. Lotsch, Science Advances **4**, eaar2317 (2018), https://www.science.org/doi/pdf/10.1126/sciadv.aar2317 .

[41] C. He, Europhysics Letters **133**, 27003 (2021).

[42] X. Liu, C. Yue, S. V. Erohin, Y. Zhu, A. Joshy, J. Liu, A. M. Sanchez, D. Graf, P. B. Sorokin, Z. Mao, J. Hu, and J. Wei, Nano Letters **21**, 4887 (2021).

[43] Y. Hu, Q. Yan, P. Zhou, Z. Li, C. He, and L. Sun, physica status solidi (RRL) – Rapid Research Letters **16**, 2200188 (2022), https://onlinelibrary.wiley.com/doi/pdf/10.1002/pssr.202200188 .

[44] H. Wu, A. M. Hallas, X. Cai, J. Huang, J. S. Oh, V. Loganathan, A. Weiland, G. T. McCandless, J. Y. Chan, S.-K. Mo, D. Lu, M. Hashimoto, J. Denlinger, R. J. Birgeneau, A. H. Nevidomskyy, G. Li, E. Morosan, and M. Yi, npj Quantum Materials **7**, 31 (2022).

[45] I. Crassee, J. Levallois, A. L. Walter, M. Ostler, A. Bostwick, E. Rotenberg, T. Seyller, D. van der Marel, and A. B. Kuzmenko, Nature Physics **7**, 48 (2011).

[46] R. Nandkishore and L. Levitov, Phys. Rev. Lett. **107**, 097402 (2011).

[47] Y. Shoji and T. Mizumoto, Science and Technology of Advanced Materials **15**, 014602 (2014), pMID: 27877640, https://doi.org/10.1088/1468-6996/15/1/014602 .

[48] Y. Shoji, K. Miura, and T. Mizumoto, Journal of Optics **18**, 013001 (2015).

[49] D. X. Nguyen and D. T. Son, Electrodynamics of thin sheets of twisted material (2020).

[50] W.-K. Tse and A. H. MacDonald, Phys. Rev. Lett. **105**, 057401 (2010).

[51] W.-K. Tse and A. H. MacDonald, Phys. Rev. B **82**, 161104 (2010).

[52] W.-K. Tse and A. H. MacDonald, Phys. Rev. B **84**, 205327 (2011).

[53] M. Kargarian, M. Randeria, and N. Trivedi, Scientific Reports **5**, 12683 (2015).

[54] S. Ghosh, A. Sahoo, and S. Nandy, arXiv 10.48550/ARXIV.2209.11217 (2022).

[55] Y. Lin, C. Zhang, L. Guan, Z. Sun, and J. Tao, Nanomaterials **10**, 10.3390/nano10091642 (2020).

[56] W. Zhou, Z. Yang, A. Li, M. Long, and F. Ouyang, Phys. Rev. B **101**, 045113 (2020).

[57] K. Zhang, L. Wang, and X. Wu, Nanoscale **11**, 19536 (2019).

[58] T. Habe, Phys. Rev. B **95**, 115405 (2017).

[59] M. M. Otrokov, I. I. Klimovskikh, H. Bentmann, D. Estyunin, A. Zeugner, Z. S. Aliev, S. Gaß, A. U. B. Wolter, A. V. Koroleva, A. M. Shikin, M. Blanco-Rey, M. Hoffmann, I. P. Rusinov, A. Y. Vyazovskaya, S. V. Eremeev, Y. M. Koroteev, V. M. Kuznetsov, F. Freyse, J. Sánchez-Barriga, I. R. Amiraslanov, M. B. Babanly, N. T. Mamedov, N. A. Abdullayev, V. N. Zverev, A. Alfonsov, V. Kataev, B. Büchner, E. F. Schwier, S. Kumar, A. Kimura, L. Petaccia, G. Di Santo, R. C.

Vidal, S. Schatz, K. Kißner, M. Ünzelmann, C. H. Min, S. Moser, T. R. F. Peixoto, F. Reinert, A. Ernst, P. M. Echenique, A. Isaeva, and E. V. Chulkov, Nature **576**, 416 (2019).

[60] M. Liu, C. Lei, H. Kim, Y. Li, L. Frammolino, J. Yan, A. H. Macdonald, and C.-K. Shih, Proceedings of the National Academy of Sciences **119**, e2207681119 (2022), https://www.pnas.org/doi/pdf/10.1073/pnas.2207681119 .

[61] Q. Lu, K. Y. Chen, M. Snyder, J. Cook, D. T. Nguyen, P. V. S. Reddy, T.-R. Chang, S. A. Yang, and G. Bian, Phys. Rev. B **104**, L201105 (2021).

[62] R.-X. Zhang and C.-X. Liu, arXiv 10.48550/ARXIV.2207.00020 (2022).

[63] G. Giuliani and G. Vignale, Quantum Theory of the Electron Liquid (Cambridge University Press, 2005).

[64] A. Ferreira, J. Viana-Gomes, Y. V. Bludov, V. Pereira, N. M. R. Peres, and A. H. Castro Neto, Phys. Rev. B **84**, 235410 (2011).

[65] F. R. Pratama, M. S. Ukhtary, and R. Saito, Phys. Rev. B **101**, 045426 (2020).

[66] Y. Zhang, Y.-W. Tan, H. L. Stormer, and P. Kim, Nature **438**, 201 (2005).

[67] K. S. Novoselov, E. McCann, S. V. Morozov, V. I. Fal'ko, M. I. Katsnelson, U. Zeitler, D. Jiang, F. Schedin, and A. K. Geim, Nature Physics **2**, 177 (2006).

[68] K. I. Bolotin, F. Ghahari, M. D. Shulman, H. L. Stormer, and P. Kim, Nature **462**, 196 (2009).

[69] N. Xin, J. Lourembam, P. Kumaravadivel, A. E. Kazantsev, Z. Wu, C. Mullan, J. Barrier, A. A. Geim, I. V. Grigorieva, A. Mishchenko, A. Principi, V. I. Fal'ko, L. A. Ponomarenko, A. K. Geim, and A. I. Berdyugin, Nature **616**, 270 (2023).

[70] J. W. McClure, Phys. Rev. **104**, 666 (1956).

[71] G. Vignale, Phys. Rev. Lett. **67**, 358 (1991).

[72] A. Raoux, M. Morigi, J.-N. Fuchs, F. Piéchon, and G. Montambaux, Phys. Rev. Lett. **112**, 026402 (2014).

[73] J. V. Bustamante, N. J. Wu, C. Fermon, M. Pannetier-Lecoeur, T. Wakamura, K. Watanabe, T. Taniguchi, T. Pellegrin, A. Bernard, S. Daddinounou, V. Bouchiat, S. Guéron, M. Ferrier, G. Montambaux, and H. Bouchiat, Science **374**, 1399 (2021), https://www.science.org/doi/pdf/10.1126/science.abf9396 .

[74] M. Koshino, in Physics and Applications of Graphene, edited by S. Mikhailov (IntechOpen, Rijeka, 2011) Chap. 19.

[75] P. Dietl, F. Piéchon, and G. Montambaux, Phys. Rev. Lett. **100**, 236405 (2008).

[76] A. Principi, M. Polini, G. Vignale, and M. I. Katsnelson, Phys. Rev. Lett. **104**, 225503 (2010).

[77] Y. Cao, V. Fatemi, S. Fang, K. Watanabe, T. Taniguchi, E. Kaxiras, and P. Jarillo-Herrero, Nature **556**, 43 (2018).

[78] M. Koshino and T. Ando, Phys. Rev. B **76**, 085425 (2007).

[79] M. Kammermeier, P. Wenk, and U. Zülicke, Physical Review B **100**, 10.1103/physrevb.100.075421 (2019).

[80] W.-Y. He, Y. Su, M. Yang, and L. He, Phys. Rev. B **89**, 125418 (2014).

[81] B. Roy and K. Yang, Phys. Rev. B **88**, 241107 (2013).

[82] M. Van der Donck, F. M. Peeters, and B. Van Duppen, Phys. Rev. B **93**, 115423 (2016).

[83] J. M. Park, Y. Cao, L.-Q. Xia, S. Sun, K. Watanabe, T. Taniguchi, and P. Jarillo-Herrero, Nature Materials **21**, 877 (2022).

[84] J. R. Wallbank, D. Ghazaryan, A. Misra, Y. Cao, J. S. Tu, B. A. Piot, M. Potemski, S. Pezzini, S. Wiedmann, U. Zeitler, T. L. M. Lane, S. V. Morozov, M. T. Greenaway, L. Eaves, A. K. Geim, V. I. Fal'ko, K. S. Novoselov, and A. Mishchenko, Science **353**, 575 (2016), https://www.science.org/doi/pdf/10.1126/science.aaf4621 .

[85] E. V. Castro, K. S. Novoselov, S. V. Morozov, N. M. R. Peres, J. M. B. L. dos Santos, J. Nilsson, F. Guinea, A. K. Geim, and A. H. C. Neto, Phys. Rev. Lett. **99**, 216802 (2007).

[86] Y. Zhang, T.-T. Tang, C. Girit, Z. Hao, M. C. Martin, A. Zettl, M. F. Crommie, Y. R. Shen, and F. Wang, Nature **459**, 820 (2009).

[87] A. H. Castro Neto, F. Guinea, N. M. R. Peres, K. S. Novoselov, and A. K. Geim, Rev. Mod. Phys. **81**, 109 (2009).

[88] C. Park, J. Ryou, S. Hong, B. G. Sumpter, G. Kim, and M. Yoon, Phys. Rev. Lett. **115**, 015502 (2015).

[89] K. Yan, H. Peng, Y. Zhou, H. Li, and Z. Liu, Nano Letters **11**, 1106 (2011).

[90] J. Bezanson, A. Edelman, S. Karpinski, and V. B. Shah, Society for Industrial and Applied Mathematics **59**, 10.1137/141000671 (2017).

[91] S. Danisch and J. Krumbiegel, Journal of Open Source Software **6**, 3349 (2021).

[92] B. Wong, Nature Methods **8**, 441 (2011).

[93] M. Zarenia, A. Principi, and G. Vignale, Phys. Rev. B **102**, 214304 (2020).

[94] J. R. Cruise, A. Seidel, E. Henriksen, and G. Vignale, Observability of cyclotron resonance in the hydrodynamic regime of bilayer graphene (2024), arXiv:2402.02231 [cond-mat.mes-hall], arXiv:2402.02231 [cond-mat.mes-hall] .

[95] D. Y. H. Ho, I. Yudhistira, N. Chakraborty, and S. Adam, Phys. Rev. B **97**, 121404 (2018).

[96] M. Zarenia, I. Yudhistira, S. Adam, and G. Vignale, Phys. Rev. B **101**, 045421 (2020).

[97] N. W. Ashcroft and N. D. Mermin, Solid State Physics (Holt-Saunders, 1976).

[98] V. N. Kotov, B. Uchoa, V. M. Pereira, F. Guinea, and A. H. Castro Neto, Rev. Mod. Phys. **84**, 1067 (2012).

[99] H.-K. Tang, J. N. Leaw, J. N. B. Rodrigues, I. F. Herbut, P. Sengupta, F. F. Assaad, and S. Adam, Science **361**, 570 (2018), https://www.science.org/doi/pdf/10.1126/science.aao2934 .

[100] J.-H. Wong, B.-R. Wu, and M.-F. Lin, The Journal of Physical Chemistry C **116**, 8271 (2012), https://doi.org/10.1021/jp300840k .

[101] J. Simon and M. Greiner, Nature **483**, 282 (2012).

[102] M. Polini, F. Guinea, M. Lewenstein, H. C. Manoharan, and V. Pellegrini, Nature Nanotechnology **8**, 625 (2013).

[103] M. Gibertini, A. Singha, V. Pellegrini, M. Polini, G. Vignale, A. Pinczuk, L. N. Pfeiffer, and K. W. West, Phys. Rev. B **79**, 241406 (2009).

[104] S. Wang, D. Scarabelli, L. Du, Y. Y. Kuznetsova, L. N. Pfeiffer, K. W. West, G. C. Gardner, M. J. Manfra, V. Pellegrini, S. J. Wind, and A. Pinczuk, Nature Nanotechnology **13**, 29 (2018).

[105] D. Q. Wang, Z. Krix, O. A. Tkachenko, V. A. Tkachenko, C. Chen, I. Farrer, D. A. Ritchie, O. P. Sushkov, A. R. Hamilton, and O. Klochan, Tuning the bandstructure of electrons in a two-dimensional artificial electrostatic crystal in gaas quantum wells (2024), arXiv:2402.12769 [cond-mat.mes-hall] .

[106] R. Bistritzer and A. H. MacDonald, Proceedings of the National Academy of Sciences **108**, 12233 (2011), https://www.pnas.org/doi/pdf/10.1073/pnas.1108174108 .

[107] N. R. Chebrolu, B. L. Chittari, and J. Jung, Phys. Rev. B **99**, 235417 (2019).

[108] A. M. Seiler, N. Jacobsen, M. Statz, N. Fernandez, F. Falorsi, K. Watanabe, T. Taniguchi, Z. Dong, L. S. Levitov, and R. T. Weitz, Nature Communications **15**, 3133 (2024).

[109] J. C. Slonczewski and P. R. Weiss, Phys. Rev. **109**, 272 (1958).

[110] J. W. McClure, Phys. Rev. **119**, 606 (1960).

[111] A. Chakraborty, A. Rodin, S. Adam, and G. Vignale, Phys. Rev. B **111**, 125130 (2025).

[112] M. Mucha-Kruczyński, E. McCann, and V. I. Fal'ko, Semiconductor Science and Technology **25**, 033001 (2010).

[113] R. T. Weitz, M. T. Allen, B. E. Feldman, J. Martin, and A. Yacoby, Science **330**, 812 (2010), https://www.science.org/doi/pdf/10.1126/science.1194988 .

[114] A. S. Mayorov, D. C. Elias, M. Mucha-Kruczynski, R. V. Gorbachev, T. Tudorovskiy, A. Zhukov, S. V. Morozov, M. I. Katsnelson, V. I. Fal'ko, A. K. Geim, and K. S. Novoselov, Science **333**, 860 (2011), https://www.science.org/doi/pdf/10.1126/science.1208683 .

[115] B. Partoens and F. Peeters, Physical Review B—Condensed Matter and Materials Physics **74**, 075404 (2006).

[116] E. McCann and V. I. Fal'ko, Phys. Rev. Lett. **96**, 086805 (2006).

[117] A. M. Seiler, F. R. Geisenhof, F. Winterer, K. Watanabe, T. Taniguchi, T. Xu, F. Zhang, and R. T. Weitz, Nature **608**, 298 (2022).

[118] H. Zhou, L. Holleis, Y. Saito, L. Cohen, W. Huynh, C. L. Patterson, F. Yang, T. Taniguchi, K. Watanabe, and A. F. Young, Science **375**, 774 (2022).

[119] A. Varlet, M. Mucha-Kruczyński, D. Bischoff, P. Simonet, T. Taniguchi, K. Watanabe, V. Fal'ko, T. Ihn, and K. Ensslin, Synthetic Metals **210**, 19 (2015).

[120] A. A. Zibrov, P. Rao, C. Kometter, E. M. Spanton, J. Li, C. R. Dean, T. Taniguchi, K. Watanabe, M. Serbyn, and A. F. Young, Physical Review Letters **121**, 167601 (2018).

[121] F. Winterer, A. M. Seiler, A. Ghazaryan, F. R. Geisenhof, K. Watanabe, T. Taniguchi, M. Serbyn, and R. T. Weitz, Nano Letters **22**, 3317 (2022).

[122] L. Campos, A. F. Young, K. Surakitbovorn, K. Watanabe, T. Taniguchi, and P. Jarillo-Herrero, Nature communications **3**, 1239 (2012).

[123] H. Zhou, T. Xie, A. Ghazaryan, T. Holder, J. R. Ehrets, E. M. Spanton, T. Taniguchi, K. Watanabe, E. Berg, M. Serbyn, et al., Nature **598**, 429 (2021).

[124] H. Zhou, T. Xie, T. Taniguchi, K. Watanabe, and A. F. Young, Nature **598**, 434 (2021).

[125] Y. Shi, S. Che, K. Zhou, S. Ge, Z. Pi, T. Espiritu, T. Taniguchi, K. Watanabe, Y. Barlas, R. Lake, et al., Physical review letters **120**, 096802 (2018).

[126] H. Zhou, L. Holleis, Y. Saito, L. Cohen, W. Huynh, C. L. Patterson, F. Yang, T. Taniguchi, K. Watanabe, and A. F. Young, Science **375**, 774 (2022), https://www.science.org/doi/pdf/10.1126/science.abm8386 .

[127] J. Jung and A. H. MacDonald, Phys. Rev. B **89**, 035405 (2014).

[128] Y. Zhao, P. Cadden-Zimansky, Z. Jiang, and P. Kim, Phys. Rev. Lett. **104**, 066801 (2010).

[129] Y. Cao, V. Fatemi, A. Demir, S. Fang, S. L. Tomarken, J. Y. Luo, J. D. Sanchez-Yamagishi, K. Watanabe, T. Taniguchi, E. Kaxiras, R. C. Ashoori, and P. Jarillo-Herrero, Nature **556**, 80 (2018).

[130] A. L. Sharpe, E. J. Fox, A. W. Barnard, J. Finney, K. Watanabe, T. Taniguchi, M. A. Kastner, and D. Goldhaber-Gordon, Science **365**, 605 (2019).

[131] X. Lu, P. Stepanov, W. Yang, M. Xie, M. Ali Aamir, I. Das, C. Urgell, K. Watanabe, T. Taniguchi, G. Zhang, A. Bachtold, A. H. MacDonald, and D. K. Efetov, Nature **574**, 653 (2019).

[132] Y. H. Kwan, S. A. Parameswaran, and S. L. Sondhi, Physical Review B **101**, 205116 (2020).

[133] G. Tarnopolsky, A. J. Kruchkov, and A. Vishwanath, Phys. Rev. Lett. **122**, 106405 (2019).

[134] J. M. B. Lopes dos Santos, N. M. R. Peres, and A. H. Castro Neto, Phys. Rev. Lett. **99**, 256802 (2007).

[135] R. de Gail, J.-N. Fuchs, M. Goerbig, F. Piéchon, and G. Montambaux, Physica B: Condensed Matter **407**, 1948 (2012), proceedings of the International Workshop on Electronic Crystals (ECRYS-2011).

[136] R. Mas-Ballesté, C. Gómez-Navarro, J. Gómez-Herrero, and F. Zamora, Nanoscale **3**, 20 (2011).

[137] Z. Bi, N. F. Q. Yuan, and L. Fu, Phys. Rev. B **100**, 035448 (2019).

[138] R. M. A. Azzam, Ellipsometry and polarized light (North-Holland Pub. Co. ; Sole distributors for the U.S.A. and Canada, Elsevier North-Holland, Amsterdam ; New York : New York, 1977).

[139] N. Kheirabadi and A. Langari, Phys. Rev. B **106**, 245143 (2022).

Appendix A

MISCELLANEOUS ANALYSIS OF ABSORPTION SPECTRA OVER ANISOTROPY AND MIXING ANGLE

A.1 Behavior of $|M|_x^2$ and $|M|_y^2$

From Fig. A.1 we can see that the squared matrix element of J_y ($|M|_y^2$) goes exactly to zero at the saddle point ($k_x = 1/\sqrt{2}$ and $k_y = 0$ for $\alpha = \pi/4$), thus suppressing the effect of the singularity in the joint density of states. At the same time, the squared matrix element of J_x (($|M|_x^2$)) remains finite, and this is why the singularity of the joint density of states is fully reflected in the absorption spectrum (Fig. 3.3(d)) for polarization along x.

A.2 Dependence of saddle-point singularity on the anisotropy parameter ρ

In the y-direction of the magnetic field, if we want to consider both the isotropic and anisotropic valleys, then the absorption coefficient takes the form.

$$\eta_y = \Big(\rho\ \cos^2\beta\ \eta_y(x) + \rho^{-1}\sin^2\beta\ \eta_y(y)\Big) \tag{A.1}$$

where $\eta_y(x)$ and $\eta_y(y)$ are the values of η_y for x and y directions of polarization of the incident light.

To better understand the interplay between the saddle-point singularity and the anisotropy parameter, we have calculated the optical absorption coefficient for the magnetic field in the y-direction for $\rho = 0.1$, which means the Dirac cones are now strongly anisotropic.

The results are plotted in Fig. A.2(a) for three different polarizations of the incident light. From

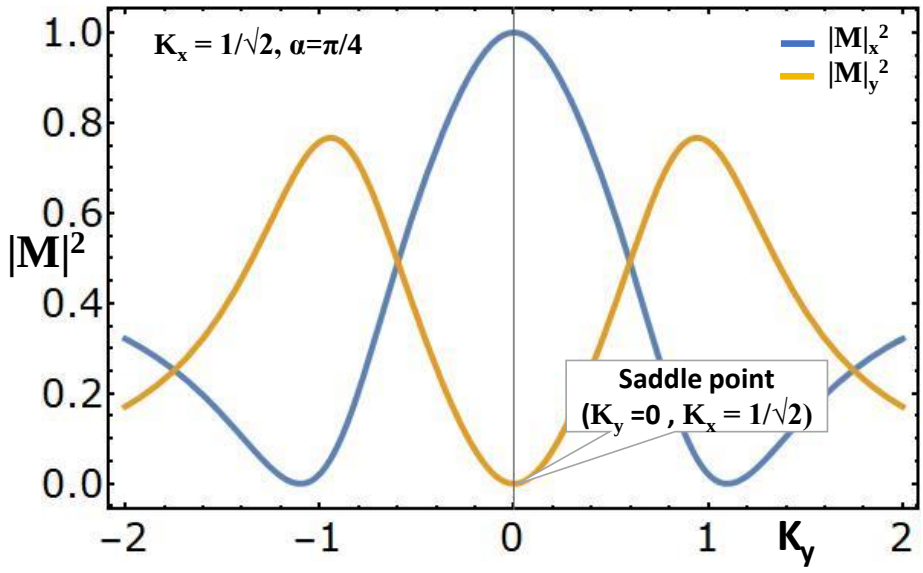

Figure A.1: *Plots of the squared matrix elements of J_x and J_y (blue and orange lines, respectively) vs k_y at constant $k_x = \cos\alpha = 1/\sqrt{2}$ for $\alpha = \pi/4$. Observe that $|M|_y^2$ (orange) goes to zero at the saddle point ($k_x = 1/\sqrt{2}, k_y = 0$), while ($|M|_x^2$) (blue) tends to* 1.

this figure, we can see that, while the saddle point singularity is still present when the incident light is polarized in the x direction (green curve), it becomes quantitatively small. It is hardly visible on the scale of the graph.

This shows that one can effectively play the band anisotropy and the saddle-point singularity against each other, thus adding another dimension to the polarization dependence of the absorption spectrum. The figure in panel (b) of Fig A.2 shows the total optical absorption coefficient $\eta_y(\bar{X}_i) + \eta_y(\bar{X}_a)$ for magnetic field along the y-direction. Notice that the absorbance can change by order of magnitude upon rotating the polarization angle.

A.3 Dependence of the absorption spectrum on mixing angle

The scenario is also robust with respect to variations of the mixing angle α: while the plots of Fig. 3.3 have been obtained for $\alpha = \pi/4$, we find the same qualitative behavior for other values of α. For the magnetic field along the y-direction, we have checked that the behavior of the absorption coefficient for $\alpha = \pi/3$ and $\alpha = \pi/5$ is qualitatively similar to what we found for $\alpha = \pi/4$ in the main text. Fig. (A.3) shows that, with increasing α, the peak in the absorption spectrum shifts to a higher frequency, tracking the position of the van Hove singularity $\omega_{critical} = 2B\sin\alpha$. Still, the qualitative behavior of the spectrum near the singularity, including its polarization dependence, remains unchanged.

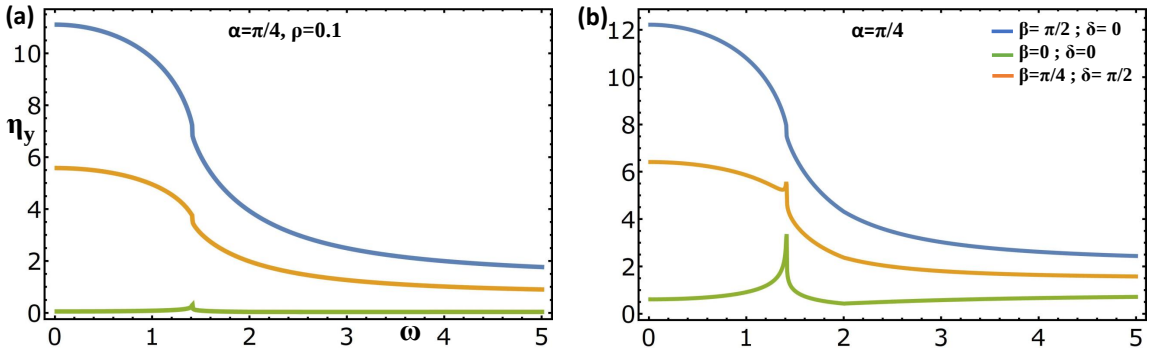

Figure A.2: *(a) Plot of the optical absorption coefficient vs ω for the anisotropic valley ($\rho = 0.1$). (b) This figure shows the total optical absorbance. By changing the polarization of the incoming light, we can tune the total absorption coefficient. Both figures are in units of $\eta_{graphene}$ for magnetic field in the y-direction, and $\alpha = \pi/4$.*

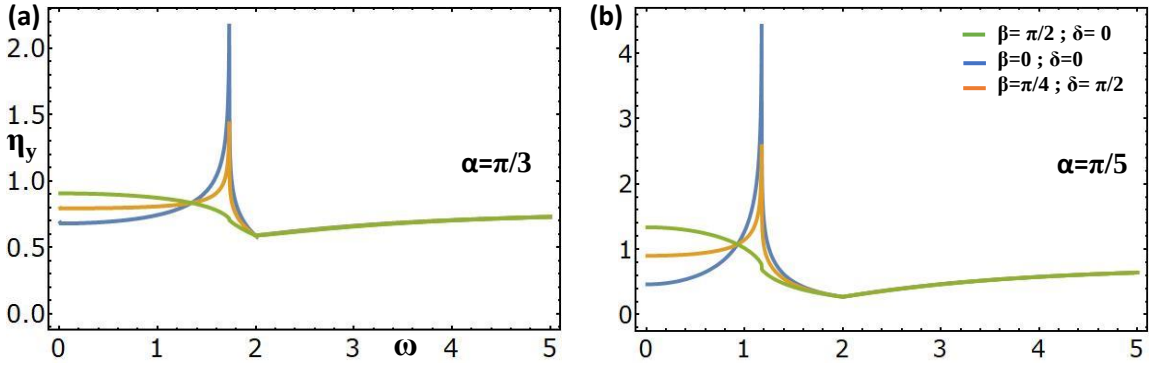

Figure A.3: *Optical absorption coefficient vs frequency for the magnetic field in the y-direction for two values of α different from the one considered in the text **(a)** $\alpha = \pi/5$ and **(b)** $\alpha = \pi/3$. Notice that the singular behavior of the absorption coefficient at the saddle point singularity is present at all α with the same polarization dependence discussed in the main text. $\rho = 1.0$.*

Appendix B

GENERALIZED ANALYSIS OF OPTICAL POLARIZATION ROTATIONS

B.1 Calculation of the polarization state for transmitted and reflected waves

An elliptically polarized state with the major semiaxis oriented along the x axis, with unit amplitude ($A = 1$) and zero absolute phase ($\delta = 0$) can be represented in the Cartesian basis ($x' - y'$ basis) (Fig. B.1) [138] as follows:

$$\mathbf{E} = \begin{pmatrix} E_{x'} \\ E_{y'} \end{pmatrix} = \begin{pmatrix} \cos\epsilon \\ i\sin\epsilon \end{pmatrix}, \quad -\pi/4 < \epsilon < \pi/4\,, \tag{B.1}$$

where ϵ is the ellipticity (for $\epsilon = 0$ the polarization is linear along the x axis, for $\epsilon = -\pi/4$ it is right-circular, for $\epsilon = \pi/4$ it is left-circular).

The general state of elliptic polarization has a major semi-axis (x') that forms an angle θ with the x axis. Thus the polarization state in the $x - y$ basis [1] is obtained by applying a rotation by an angle $-\theta$ to the state (B.1). This gives

$$\begin{pmatrix} E_x \\ E_y \end{pmatrix} = R(-\theta) \begin{pmatrix} E_{x'} \\ E_{y'} \end{pmatrix} = \begin{pmatrix} \cos\theta\cos\epsilon - i\sin\theta\sin\epsilon \\ \sin\theta\cos\epsilon + i\cos\theta\sin\epsilon \end{pmatrix}, \quad -\pi/4 < \epsilon < \pi/4\,,\ -\pi/2 < \theta < \pi/2\,. \tag{B.2}$$

[1] Keeping the absolute phase of the electric field vector as zero ($\delta = 0$)and of unit magnitude ($A = 1$). One can multiply with $Ae^{i\delta}$ to comprehend a more general scenario.

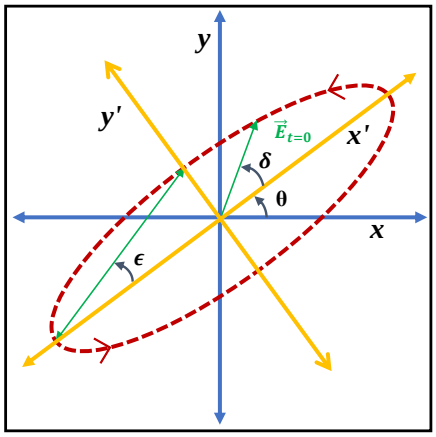

Figure B.1: *Schematic diagram for left-handed elliptical polarization. The major and minor axes are aligned along the x' and y' axes, respectively. The four parameters that define the ellipse of polarisation are (1) The angle θ between the major axis and a fixed axis of reference x. If the azimuthal angle θ is negative, it would be a right-handed polarization.(2) The ellipticity $e = b/a = \tan\epsilon$. The ellipticity has a range $-1 \leq e \leq 1$. If $e = -b/a = -\tan\epsilon$ instead, it is right-handed as well.(3) The total amplitude $A = \sqrt{a^2 + b^2}$ and (4) The absolute phase δ is defined as the angle between the electric field at $t = 0$ and the major axis.*

Transforming to the chiral basis as we did before in Eq. (4.40) this becomes

$$\begin{pmatrix} E_+ \\ E_- \end{pmatrix} = \frac{1}{\sqrt{2}} \begin{pmatrix} e^{i\theta}(\cos\epsilon - \sin\epsilon) \\ e^{-i\theta}(\cos\epsilon + \sin\epsilon) \end{pmatrix} = \begin{pmatrix} z \\ z^{-1} \end{pmatrix} \tag{B.3}$$

where the complex number z is given by

$$\begin{aligned} z &= e^{i\theta}\sqrt{\frac{\cos\epsilon - \sin\epsilon}{\cos\epsilon + \sin\epsilon}} \\ &= e^{i\theta}\sqrt{\frac{1 - \tan\epsilon}{1 + \tan\epsilon}}\,. \end{aligned} \tag{B.4}$$

Notice that $Arg(z) = \theta$ varies between $-\pi/2$ and $\pi/2$, while $|z| = \sqrt{\frac{1-\tan\epsilon}{1+\tan\epsilon}}$ ranges from 0 to ∞ as the ellipticity varies from $\pi/4$ to $-\pi/4$. Thus it is easy to extract the parameters θ and ϵ from any given state vector expressed in the chiral representation. Let us define a second measure of ellipticity γ in the following manner

$$e^{\gamma} = \sqrt{\frac{1 - \tan\epsilon}{1 + \tan\epsilon}}\,, \qquad \gamma = \frac{1}{2}\ln\frac{1 - \tan\epsilon}{1 + \tan\epsilon} \tag{B.5}$$

such that $\gamma = 0$ for linear polarization and $\gamma = \infty$ for circular polarization. Then we can write

$$z = e^{i(\theta - i\gamma)}\,. \tag{B.6}$$

In other words, γ can be interpreted as the imaginary part of the angle that defines the orientation of the major semiaxis with respect to the x-axis. Let us now consider the action of the transmission or reflection matrix on the incoming polarization state. Using the definition of z from Eq. (B.6) and acting with $\tilde{\mathbf{T}}$ (Eq. 4.40) on the state (B.3) we get the output

$$\tilde{\mathbf{T}} \cdot \begin{pmatrix} e^{i\theta}e^{\gamma} \\ e^{-i\theta}e^{-\gamma} \end{pmatrix} = \begin{pmatrix} (\bar{T} + iT_{xy})e^{i\theta}e^{\gamma} + \Delta T e^{-i\theta}e^{-\gamma} \\ (\bar{T} - iT_{xy})e^{-i\theta}e^{-\gamma} + \Delta T e^{i\theta}e^{\gamma} \end{pmatrix} \tag{B.7}$$

This can be cast in the form $\begin{pmatrix} z' \\ (z')^{-1} \end{pmatrix}$, where, following Eq. (B.6), we have

$$z' = e^{i\theta'}e^{\gamma'} = \sqrt{\frac{(\bar{T} + iT_{xy})e^{i\theta}e^{\gamma} + \Delta T e^{-i\theta}e^{-\gamma}}{(\bar{T} - iT_{xy})e^{-i\theta}e^{-\gamma} + \Delta T e^{i\theta}e^{\gamma}}}\,. \tag{B.8}$$

Finally, taking the complex logarithm and doing some simple transformations, we get

$$\gamma' + i\theta' = \gamma + i\theta + \frac{1}{2}\mathrm{L}n\frac{\bar{T} + iT_{xy} + \Delta T e^{-2i\theta}e^{-2\gamma}}{\bar{T} - iT_{xy} + \Delta T e^{2i\theta}e^{2\gamma}} \tag{B.9}$$

Using Eq. (B.9), we can find the complex angle, which has a real part, the Faraday angle, and an imaginary part, which is related to the ellipticity of the transmitted wave. Separating the real and the imaginary parts of the logarithm we find

$$\gamma' = \gamma + \frac{1}{2}\ln\left|\frac{\bar{T} + iT_{xy} + \Delta T e^{-2i\theta}e^{-2\gamma}}{\bar{T} - iT_{xy} + \Delta T e^{2i\theta}e^{2\gamma}}\right| \tag{B.10}$$

$$\theta' = \theta + \frac{1}{2}\mathrm{A}rg\left(\frac{\bar{T} + iT_{xy} + \Delta T e^{-2i\theta}e^{-2\gamma}}{\bar{T} - iT_{xy} + \Delta T e^{2i\theta}e^{2\gamma}}\right)\,. \tag{B.11}$$

The difference $\theta' - \theta$ is the Faraday rotation angle θ_F, and we can calculate the ellipticity ($=\tan\epsilon$) using the Eq. (B.5) and from the difference $\gamma' - \gamma$. A similar treatment can be applied to the reflection matrix operating on the incoming polarization to get the Kerr rotation of reflected light.

In the isotropic case, $T_{xx} = T_{yy} = \bar{T}$ and $\Delta T = 0$, the formula for the Faraday rotation angle reduces to

$$\theta' - \theta = \theta_F = \frac{1}{2}Arg\left[\frac{T_{xx} + iT_{xy}}{T_{xx} - iT_{xy}}\right] = \frac{1}{2}Arg\left[\frac{T_+}{T_-}\right]\,, \tag{B.12}$$

which agrees with Eq. (4.35) of the main text and is independent of the direction of polarization of the incident light. In the presence of anisotropy, however, the rotation angle does depend on the direction of polarization of the incident light (linear), and, in addition, the transmitted light is

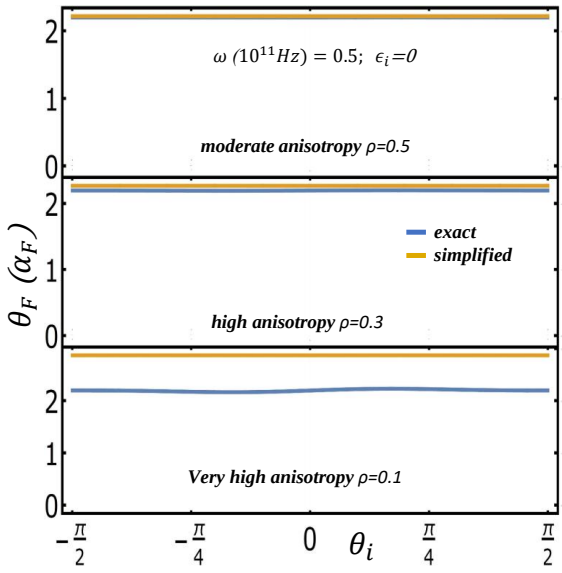

Figure B.2: *Faraday rotation as a function of the initial angle of linear polarization. The plots show the comparison between the exact and the simplified approach from our main text. Here the incident polarization is set to linear, making the ellipticity of the incident light zero ($\epsilon_i = 0$). For a low anisotropy factor, the Faraday angle has a minimal difference between the two approaches. Still, with increasing anisotropy, the Faraday rotation has a mismatch between peak values.*

elliptically polarized.

As a demonstration of the use of Eqs. (B.10,B.11) and Eq. (4.29), we calculate the state of polarization of the outgoing wave for an incident wave that is linearly polarized along the x-direction (i.e., $\theta = 0; \gamma = 0$). We find (see also Eq. B.2))

$$\begin{pmatrix} E'_x \\ E'_y \end{pmatrix} = \begin{pmatrix} \cos\theta' \cos\epsilon' - i \sin\theta' \sin\epsilon' \\ \sin\theta' \cos\epsilon' + i \cos\theta' \sin\epsilon' \end{pmatrix} = \begin{pmatrix} 0.999748 - 0.000184i \\ -0.020593 - 0.008917i \end{pmatrix} \tag{B.13}$$

where we have chosen $\rho = 0.1$, the bandgap $\Delta = 1$, and the frequency $\omega = 1.1\Delta$. From Eq. (B.13), we see that an initially linearly polarized wave after passing through the medium is transformed into an elliptically polarized wave, with ellipticity $e = \tan\epsilon' \approx 0.01$.

Now that we have established the exact formulation, let us benchmark the "simplified" definition of the Faraday rotation angle we used in our main text. For initial linear polarization ($\epsilon_i = 0$), we find that the dependence of the Faraday rotation angle on θ_i is indeed negligible for all values of the anisotropy parameter (Fig.B.2). In addition, the difference between the exact rotation angle and the approximate one of the main text is relatively small in a broad range of values of ρ, $0.1 < \rho < 1$. This remains true essentially for all frequencies.

Lastly, let us consider an elliptically polarized initial state and see what our exact formulas say.

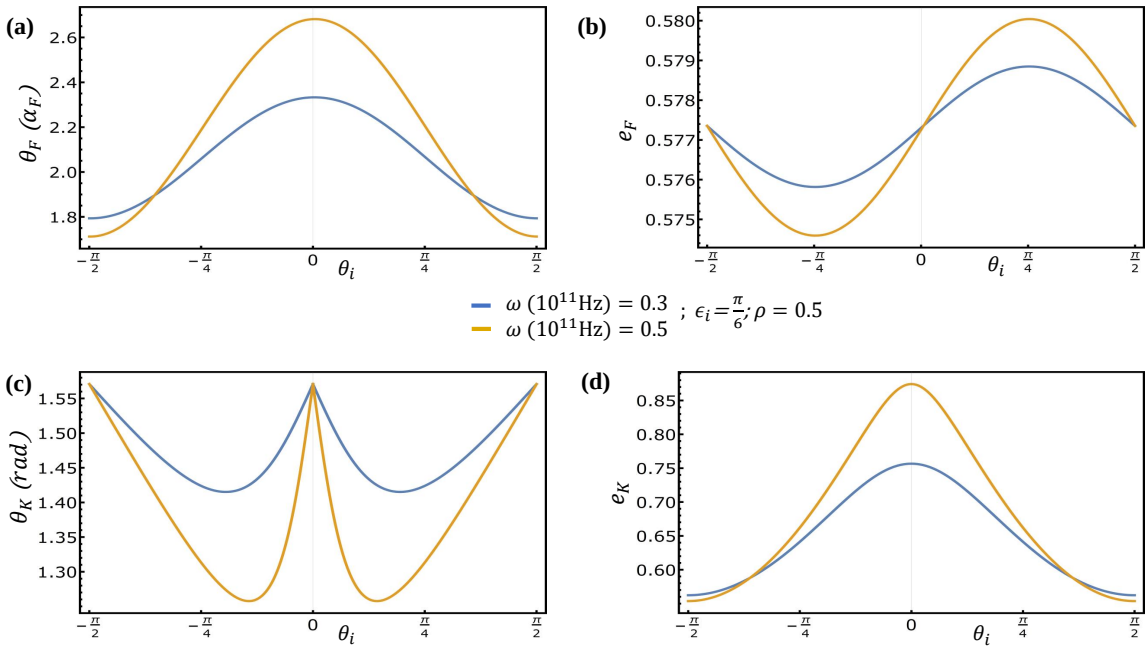

Figure B.3: *Faraday and Kerr rotation as a function of the incident polarization angle and the optical frequency of the incident beam. Panel (a) and (c) show the exact Kerr and Faraday rotation angles as functions of θ_i for $\omega = 0.3$ and $\omega = 0.5$, respectively. Panel (b) and (d) show the ellipticity $e(= \tan\epsilon)$ of the transmitted and reflected wave as the function of θ_i for $\omega = 0.3$ and $\omega = 0.5$, respectively.*

Fig. (B.3) shows that the Faraday rotation angle – and, more generally, the entire polarization state of the transmitted wave – significantly depends on the initial angle θ_i. Therefore, in this case (elliptically polarized incident light and strong anisotropy), the simplified approach we have used in the main text would not be accurate, and the exact formulas must be used instead.

Appendix C

EXTENSION TO FULL TIGHT-BINDING MODEL OF AB-BILAYER & CONNECTION BETWEEN LAYER POLARIZATION AND MAGNETIC RESPONSE

C.1 Full-Tight Binding model of AB-Bilayer Graphene

We present here the Bernal-stacked graphene bilayer with a parallel magnetic field and a transverse electric field described by a tight-binding Hamiltonian with nearest-neighbor intra- and interlayer hopping [139]

$$H_{\mathbf{k}} = \begin{pmatrix} V & \gamma_0 f(\mathbf{k}_\mathrm{t}) & \gamma_4 f(\mathbf{k}) & \gamma_3 f^*(\mathbf{k}) \\ \gamma_0 f^\dagger(\mathbf{k}_\mathrm{t}) & V & \gamma_1 & \gamma_4 f(\mathbf{k}) \\ \gamma_4 f^*(\mathbf{k}) & \gamma_1 & -V & \gamma_0 f(\mathbf{k}_\mathrm{b}) \\ \gamma_3 f(\mathbf{k}) & \gamma_4 f^*(\mathbf{k}) & \gamma_0 f^\dagger(\mathbf{k}_\mathrm{b}) & -V \end{pmatrix} \tag{C.1}$$

In addition to the nearest-neighbor intralayer hopping energy $\gamma_0 = -2.8$ eV and the vertical interlayer hopping $\gamma_1 = 0.3$ eV, we include the skew interlayer couplings $\gamma_3 = -0.1$ eV and $\gamma_4 = 0.12$ eV [12]. Using this model, we demonstrate that the insulator-to-metal (IM) transition predicted in the effective Hamiltonian discussed in the main text also occurs in the full tight-binding model.

In Fig. C.1, the central panel demonstrates that the IM transition occurs at the critical magnetic flux $\Phi_c = 0.011$, consistent with the results of the effective model. Notably, at $\Phi = \Phi_c$, the particle-hole symmetry is broken: the lower conduction band touches the Fermi level, whereas the upper valence band does not. Beyond the transition point, the pocket sizes of the valence and conduction bands become nearly identical.

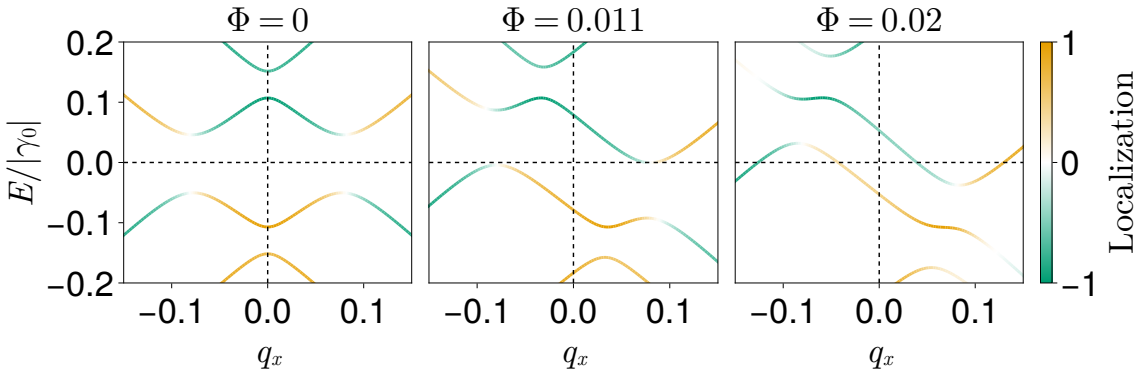

Figure C.1: *Full Tight-Binding Band edge.We plot here the full-tight binding model including the skew-coupling terms γ_3, γ_4. The three figures represent different in-plane magnetic fields and the corresponding localization of states for a displacement field of $V = \gamma_1$. The central figure reveals that the IM transition happens at the same magnetic field even in the complete picture. We also kept the study of the localization built into the figures to show that the localization of states still exists at the band edge.*

This behavior is supported by the fact that the skew interlayer coupling terms are proportional to the factor f_k, which is unaffected by the applied magnetic field. [1] Furthermore, f_k approaches zero near the Dirac points, resulting in a negligible contribution from these terms to the band structure.

In conclusion, the critical magnetic field for the IM transition remains numerically unchanged. Therefore, we continue to employ the simplified model described in the main text for further analysis without loss of generality.

C.2 Model and gap-closing transition

For the description of Bernal-stacked bilayer graphene in crossed magnetic and electric fields we employ the well-known 4×4 tight-binding model

$$H_{\mathbf{k}}(V, \Phi) = V\,(\tau_z \otimes \sigma_0) + \frac{\gamma_1}{2}\,(\tau_+ \otimes \sigma_- + \tau_- \otimes \sigma_+) \\ - \frac{\gamma_0}{2}\Big\{\tau_0 \otimes [\mathbf{f}\,(\mathbf{k}_\mathrm{t}) + \mathbf{f}\,(\mathbf{k}_\mathrm{b})] + \tau_z \otimes [\mathbf{f}\,(\mathbf{k}_\mathrm{t}) - \mathbf{f}\,(\mathbf{k}_\mathrm{b})]\Big\} \cdot \boldsymbol{\sigma}\,, \tag{C.2}$$

where the Pauli matrices $\boldsymbol{\sigma} = (\sigma_x, \sigma_y, \sigma_z)$, $\sigma_\pm = (\sigma_x \pm i\sigma_y)/2$ act on the degree of freedom of the sublattice, the Pauli matrices $\boldsymbol{\tau} = (\tau_x, \tau_y, \tau_z)$, $\tau_\pm = (\tau_x \pm i\tau_y)/2$ act on the layer degree of freedom and $\otimes$ is the external product in the combined sublattice/layer space. Here $\mathbf{f}(\mathbf{k}) = (\mathrm{Re}\, f(\mathbf{k}), \mathrm{Im}\, f(\mathbf{k}), 0)$. The in-plane magnetic field enters through the shifted wave vectors $\mathbf{k}_t$ and $\mathbf{k}_b$ defined for the *top* and

[1] For interlayer hopping, the displacement vector between the two atoms lies predominantly in the out-of-plane direction $\mathbf{r}_{2j} - \mathbf{r}_{1i} = d\mathbf{r} \to \hat{z}$. Since the vector potential of an in-plane magnetic field does not contribute in the out-of-plane direction, the line integral vanishes: $\phi_{ij} = \frac{\hbar}{e}\int_{r_{1i}}^{r_{2j}} \mathbf{A} \cdot d\mathbf{r} \to 0$. Thus, no effective phase shift arises for the interlayer coupling, leaving the hopping term f_k unchanged.

bottom-layer respectively. $\mathbf{k}_{\mathrm{t/b}}a = \mathbf{k}a \pm \pi\Phi(\sin\theta, -\cos\theta, 0)$, and V is the electric displacement field. We note for future use the first and second derivative of the Hamiltonian with respect to the in-plane magnetic field:

$$\begin{aligned} H'_{0,\mathbf{k}}(V,\Phi) = -\frac{\gamma_0}{2}\Big\{ & \tau_0 \otimes [\mathbf{f}'(\mathbf{k}_{\mathrm{t}}) + \mathbf{f}'(\mathbf{k}_{\mathrm{b}})] \\ & + \tau_z \otimes [\mathbf{f}'(\mathbf{k}_{\mathrm{t}}) - \mathbf{f}'(\mathbf{k}_{\mathrm{b}})] \Big\} \cdot \boldsymbol{\sigma}\,, \\ H''_{0,\mathbf{k}}(V,\Phi) = -\frac{\gamma_0}{2}\Big\{ & \tau_0 \otimes [\mathbf{f}''(\mathbf{k}_{\mathrm{t}}) + \mathbf{f}''(\mathbf{k}_{\mathrm{b}})] \\ & + \tau_z \otimes [\mathbf{f}''(\mathbf{k}_{\mathrm{t}}) - \mathbf{f}''(\mathbf{k}_{\mathrm{b}})] \Big\} \cdot \boldsymbol{\sigma}\,, \end{aligned} \tag{C.3}$$

where $\mathbf{f}'$ and $\mathbf{f}''$ represents the 1st and the 2nd derivative with respect to the in-plane magnetic field. At zero magnetic field, these expressions become much simpler

$$\begin{aligned} H'_{\mathbf{k}}(V, \Phi = 0) &\equiv \gamma_0 \tau_z \otimes [\mathbf{f}' \cdot \boldsymbol{\sigma}]\,, \\ H''_{\mathbf{k}}(V, \Phi = 0) &\equiv \gamma_0 \tau_0 \otimes [\mathbf{f}'' \cdot \boldsymbol{\sigma}]\ ; \end{aligned} \tag{C.4}$$

It is easy to verify that for any V and Φ, the Hamiltonian changes sign under the unitary transformation $U_1 = \tau_x \otimes \sigma_y$ i.e.,

$$U_1 H_{\mathbf{k}}(V,\Phi) U_1^{\dagger} = -H_{-\mathbf{k}}(V,\Phi)\,. \tag{C.5}$$

In addition, the unitary transformation $U_2 = \tau_0 \otimes \sigma_z$ reverses the sign of the Hamiltonian *and* the electric potential:

$$U_2 H_{\mathbf{k}}(V,\Phi) U_2^{\dagger} = -H_{\mathbf{k}}(-V,\Phi)\,. \tag{C.6}$$

Finally, $H_{\mathbf{k}}(V,\Phi)$ and $H_{-\mathbf{k}}(V,-\Phi)$ have the same spectrum: in fact, these two hermitian operators are the complex conjugate of each other. Knowing that $k \to -k$ changes the sign of the spectrum (Eq. (C.5)) we can safely conclude that $\Phi \to -\Phi$ (at fixed $\mathbf{k}$) also changes the sign of the spectrum. These symmetries imply that the gap is centered around zero energy and closes when a valence and a conduction band become degenerate at zero energy, leading to the insulator-to-metal (IM) transition. The existence of zero-energy states can be assessed by equating the determinant of Eq. (C.2) to zero:

$$\begin{aligned} |H_{\mathbf{k}}(V,\Phi)| = V^4 + & \left[\gamma_1^2 - \gamma_0^2 \left(|f(\mathbf{k}_{\mathrm{t}})|^2 + |f(\mathbf{k}_{\mathrm{b}})|^2\right)\right] V^2 \\ & + \gamma_0^4 |f(\mathbf{k}_{\mathrm{t}})|^2 |f(\mathbf{k}_{\mathrm{b}})|^2 = 0\,. \end{aligned} \tag{C.7}$$

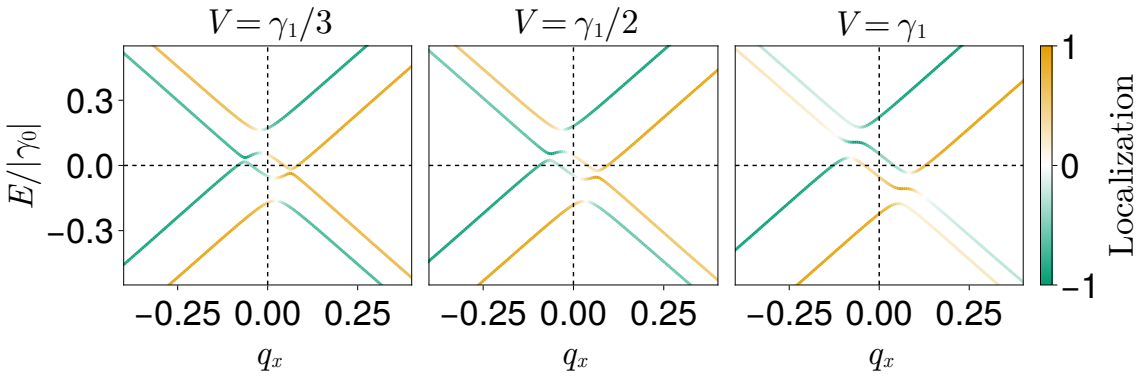

Figure C.2: *Band edge and Localization. The three figures represent different displacement fields and the corresponding localization of states for an in-plane magnetic field of* $\Phi = 0.02$ *(*$\Phi \geq \Phi_c$*). Our localization study reveals that for* $V \geq \gamma_1$*, the band minima (lower conduction band) consist of delocalized particles, which, along with the band edge contribution, are responsible for the paramagnetic response at* $\mu = 0$*. However, for* $V \leq \gamma_1/2$*, the deep states and localized states no longer coincide. Consequently, the paramagnetic response is significantly weakened.*

Solving Eq. (C.7) for V^2 yields two solutions

$$V_{\pm}^2 = \frac{1}{2}\left(\frac{C_+ + C_-}{2} \pm \sqrt{C_+ C_-}\right), \tag{C.8}$$

$$C_{\pm} = \gamma_0^2 \left[|f(\mathbf{k}_\mathrm{t})| \pm |f(\mathbf{k}_\mathrm{b})|\right]^2 - \gamma_1^2 . \tag{C.9}$$

The existence of real roots $V_\pm$ for a certain value of Φ at any point within the Brillouin zone indicates that there are zero-energy states and the gap is closed. As can be seen from Eq. (C.8), the necessary and sufficient condition for the existence of real $V_\pm$ is $C_+ > C_- \geq 0$. By determining the minimum value of Φ for which a region with $C_- > 0$ appears in the Brillouin zone, we determine the minimum magnetic field that can close the gap opened by the transverse electric field. We observe that the band closure takes place close in the vicinity of the K point, which allows us to expand C_- around it and equate C_- to zero, leading to

$$\frac{9}{4}\left[|\mathbf{k}_\mathrm{t}| - |\mathbf{k}_\mathrm{b}|\right]^2 = \frac{\gamma_1^2}{\gamma_0^2} . \tag{C.10}$$

The maximum value the quantity inside the brackets can take is $\pi\Phi/\Phi_0$, leading to $\Phi = |\gamma_1/3\pi\gamma_0|\Phi_0 \approx 0.011\Phi_0$ as the minimum value of Φ required to close the gap.

C.3 Localization of states and Magnetic response

Localization: To justify our results of the magnetic response we will take into account two factors; one is the localization of the states and the other is the displacement field. Let us first define what

we mean by localization of states:

$$L(k,\Phi,V) = \left[\left(|\psi_{1A}|^2 + |\psi_{1B}|^2\right) - \left(|\psi_{2A}|^2 + |\psi_{2B}|^2\right)\right] \tag{C.11}$$

here the ϕ's are the wavefunction of their respective layer and sublattices. For delocalized states, the localization function approaches zero. To understand band localization, we examined the region near the Dirac cones and found delocalized states near the band minima. Particles in these states, when crossing the chemical potential thresholds, become susceptible to magnetic fields.

Carefully looking at the Eq. (C.11); we can state that the Localization function is the expectation value of the operator τ_z.

$$L = \langle \tau_z \rangle \tag{C.12}$$

and the mean squared fluctuation of z is

$$(\Delta\tau_Z)^2 = \langle \tau_z^2 \rangle - \langle \tau_z \rangle^2 = 1 - L^2. \tag{C.13}$$

thus for the delocalized states ($L \approx 0$) the mean-squared fluctuations in τ_z is close to 1. Hence the fluctuation is highest for delocalized states, and any slight change in the localization factor will significantly affect the fluctuation.

Magnetic Moment: Next, we will examine the in-plane orbital moment and correlate it with the localization of states. This analysis will strengthen our argument that the change in localization, as we move around the band, is responsible for the observed changes in the system's magnetic response.

The equation that describes the in-plane magnetic moment is as follows

$$\mathbf{m} = \frac{e}{4\hbar}\left[\mathbf{r} \times \mathbf{v} - \mathbf{v} \times \mathbf{r}\right]; \tag{C.14}$$

here $\mathbf{v}$ refers to the velocity operator with respect to the applied field. If we consider the magnetic field is along the $y-$direction, then the moment can be written as

$$m_y = \frac{e}{2\hbar} z v_x \tag{C.15}$$

the xv_z term contributes the same as zv_x , but with a negative sign. Then, using

$$z = \tau_z : \quad v_x = \partial H/\partial k_x = \gamma_0 \tau_0 (\partial \mathbf{f}/\partial k_x).\boldsymbol{\sigma}, \tag{C.16}$$

this above equation is valid for zero field calculations only; otherwise, for non-zero field moment calculations, the Fermi velocities will be different in each layer. In the zero-field case, we have:

$$m_y = \gamma_0 \tau_z \left(\partial \mathbf{f}/\partial k_x \cdot \boldsymbol{\sigma}\right) = H'_{0,\mathbf{k}} \tag{C.17}$$

From this equation, we observe that the in-plane moment in the zero-field case is directly proportional to the final term of the susceptibility, namely the Fermi surface term (responsible for the paramagnetic response at charge neutrality). Additionally, the moment is proportional to the τ_z-operator, implying that a high fluctuation in the τ_z-operator will result in a high fluctuation in the in-plane magnetic moment.

Our observations indicate that the fluctuation in the τ_z-operator is highest for delocalized states. Therefore, we conclude that delocalized states induce the greatest fluctuation in the in-plane moment, leading to a stronger paramagnetic response. [2]

Having established that high fluctuations in the localization of states are responsible for the paramagnetic response in susceptibility, we now discuss the emerging scenarios and their corresponding explanations. The radius of these pockets is influenced by the displacement field, which, when increased, encompasses more delocalized states. In our discussion, we refer to these sufficiently dense states as deep states. When deep states coincide with delocalized states, a paramagnetic response emerges.

The deep states are located at the local extremas of the lower conduction (higher valence) band, which are approximately at $E \approx \frac{\gamma_1}{2}$ or $E \approx 0$. If these locations have delocalized states ($L \approx 0$), it results in high fluctuations in the magnetic moment, leading to a paramagnetic response. Assuming this to be true, let us analyze the magnetic response observed in Fig.3 of the main text and the band dispersion observed at Fig. C.2.

- For $V = \frac{\gamma_1}{3}$ at $E \approx 0$, there are delocalized states that are not deep enough for $\Phi < \Phi_c$. However, for $\Phi > \Phi_c$ at $E \approx \frac{\gamma_1}{2}$, the coincidence of delocalized states with the band edge is observed, but they are not deep enough, leading to a weak response.

- For $V = \frac{\gamma_1}{2}$ at $E \approx 0$, the delocalized states are not deep enough for $\Phi < \Phi_c$ resulting a response that is reaching towards the paramagnetism. For $\Phi > \Phi_c$, even though the states are deep enough, they are not sufficiently delocalized, resulting in a weak paramagnetic response.

[2] Classically the paramagnetic response is proportional to the mean squared fluctuation of the magnetic moment; $\chi = n\left(\Delta m_y\right)^2 / T$ (n is the electron density, T the temperature). This gives the correct quantum result for the electron gas in the $T \to 0$ limit.

- For $V \geq \gamma_1$, there are highly dense delocalized states at $E \approx 0$ for $\Phi > \Phi_c$. For $\Phi < \Phi_c$, the delocalized states are not deep enough.

The key point is that a significant paramagnetic response occurs when there is a deep enough band edge ($V \geq \gamma_1$) along with delocalized states ($L \approx 0$). If either of these criteria is not adequately met, the paramagnetic response will be weak or absent.

Appendix D

TWO-BAND CONTINUUM MODEL OF TRIGONAL WARPED AB-BILAYER GRAPHENE

D.1 Method to derive two-band effective Hamiltonian with the presence of external crossed field setup

A rigorous tight-binding Hamiltonian for AB-bilayer graphene has been derived and discussed in the previous section, which can be used to describe the dispersion for any k in the Brillouin Zone.

But if to get a bit more flavor of the effect of the trigonal warping in detail we could proceed with the two-band model of the AB-bilayer graphene and integrate out the high energy regime non-associated with the warping effect. The inter-layer coupling γ_1 forms a dimer from the pair between orbitals of $B_t \rightarrow A_b$ state, thus leading to formation of high-energy bands. Low-energy bands related to orbitals on the non-dimer sites $A_t \rightarrow B_b$. A simple model may be obtained by eliminating orbitals related to the dimer sites, resulting in an effective two-band Hamiltonian for the low-energy orbitals. The mathematics is motivated from the paper [108, 112, 116].

We rearrange H such that it is now written in basis $\mathrm{A_t}$, $\mathrm{B_b}$, $\mathrm{A_b}$, and $\mathrm{B_t}$. And then into 2×2 blocks, where the upper-left diagonal block represent the low-energy block H_{11} and the high-energy block is at the right bottom corner H_{22}.

$$H = \begin{bmatrix} H_{11} & H_{12} \\ H_{21} & H_{22} \end{bmatrix}, \tag{D.1}$$

Then, we take the 4×4 Green's function determined by H, use it to identify the effective low-energy bilayer Hamiltonian $\hat{H}_{11}$ as discussed in detail in Appendix D.1.

For an energy approximation $E << \gamma_1$ and keeping the direction of magnetic field fixed along the y-axis we can write the effective two-band model Hamiltonian for the sublattice components (ψ_{A_t}, ψ_{B_b}), under the assumption that the intralayer hopping γ_0 and interlayer coupling γ_1 dominate over all other energy scales:

$$\gamma_0, \gamma_1 \gg |E|,\, vk,\, |\gamma_3|,\, |\gamma_4|,\, |V|,\, |\Delta|$$

Retaining only terms linear in the small parameters $|\gamma_3|, |\gamma_4|, |V|, |\Delta|$ and quadratic in momentum p, the effective Hamiltonian becomes:

$$\hat{H}_{11} = H_{11} - H_{12} H_{22}^{-1} H_{21}. \tag{D.2}$$

However, before we proceed to do a discussion in low energy properties which are dominated by the band structure near the two valleys we need to expand the f_k-function near the valley K.

In the low-energy approximation the $f(k)$ reduces to

$$f(k) \approx -\tfrac{\sqrt{3}a}{2\hbar}(k_x - ik_y) + \tfrac{a^2}{8\hbar^2}\left(k_x + ik_y\right)^2 \tag{D.3}$$

$$= -\tfrac{\sqrt{3}a}{2\hbar}\pi^\dagger + + \tfrac{a^2}{8\hbar^2}\pi^2 \tag{D.4}$$

where we represent $\pi = k_x + ik_y$ and $\pi^\dagger = k_x - ik_y$. Also, we define $v = \frac{\sqrt{3}a}{2\hbar}\gamma_0$, $v_3 = \frac{\sqrt{3}a}{2\hbar}\gamma_3$ and $v_4 = \frac{\sqrt{3}a}{2\hbar}\gamma_4$. If we add a magnetic field in the y-direction then

$$f(k_+) = f(k + \phi) = -\frac{\sqrt{3}a}{2\hbar}(\pi^\dagger + \phi) \tag{D.5}$$

$$f(k_-) = f(k - \phi) = -\frac{\sqrt{3}a}{2\hbar}(\pi^\dagger - \phi) \tag{D.6}$$

here ϕ is real; if the magnetic field is in x-direction the ϕ would be imaginary. We proceed with keeping ϕ-real.

Which makes the two-model hamiltonian as

$$\hat{H}_1 = \begin{bmatrix} V & v_3\pi - \frac{v_3^2}{6\gamma_3}(\pi^\dagger)^2 \\ v_3\pi^\dagger - \frac{v_3^2}{6\gamma_3}(\pi)^2 & -V \end{bmatrix} \tag{D.7}$$

$$- \begin{bmatrix} \frac{Vv^2}{\gamma_1^2}(\pi^\dagger + \phi)(\pi + \phi) - \frac{vv_4}{\gamma_1}\left[\pi(\pi^\dagger + \phi) + H.C.\right] & \frac{v^2}{\gamma_1}\left[(\pi^\dagger)^2 - \phi^2\right] - \frac{2V\gamma_0\gamma_4}{\gamma_1^2}(\pi^\dagger\phi) \\ \frac{v^2}{\gamma_1}\left[\pi^2 - \phi^2\right] - \frac{2V\gamma_0\gamma_4}{\gamma_1^2}(\pi\phi) & -\frac{Vv^2}{\gamma_1^2}(\pi^\dagger - \phi)(\pi - \phi) - \frac{vv_4}{\gamma_1}\left[\pi(\pi^\dagger - \phi) + H.C.\right] \end{bmatrix}.$$

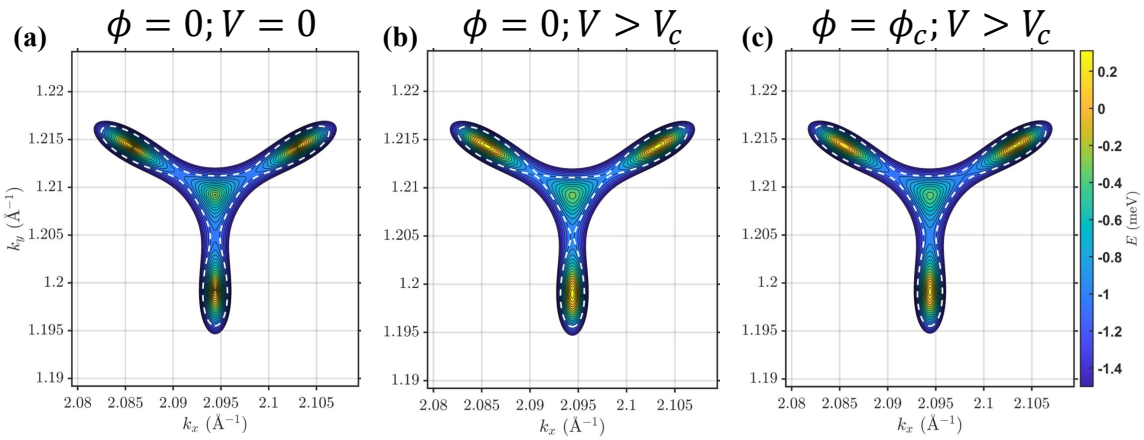

Figure D.1: *LT in trigonal-warped bilayer graphene under different external fields.* ***(a)*** *Zero-field case, showing the LT at approximately* -1 meV. ***(b)*** *For* $V > V_c$*, the system enters an insulating state, with the transition occurring at a slightly shifted energy of* -0.97 meV. ***(c)*** *In the metallic state (*$V = 0.7$ meV, $B = 25$ T*), the applied magnetic field breaks the rotational (*C_3*) symmetry of the iso-energy contours, leading to anisotropic transition energies along different crystallographic directions.*

This could be deconstructed into several parts

$$\hat{H}_1 = h_0 + h_w + h_a + h_V \tag{D.8}$$

Here

$$h_0 = -\frac{v^2}{\gamma_1^2}\begin{bmatrix} 0 & (\pi^\dagger)^2 - \phi^2 \\ (\pi)^2 - \phi^2 & 0 \end{bmatrix} \tag{D.9}$$

$$h_w = -v_3\begin{bmatrix} 0 & \pi - \frac{v_3}{6\gamma_3}(\pi^\dagger)^2 \\ \pi^\dagger - \frac{v_3}{6\gamma_3}(\pi)^2 & 0 \end{bmatrix} \tag{D.10}$$

$$h_a = \frac{vv_4}{\gamma_1}\begin{bmatrix} [\pi(\pi^\dagger + \phi) + H.C.] & \frac{2V}{\gamma_1}(\pi^\dagger\phi) \\ \frac{2V}{\gamma_1}(\pi\phi) & [\pi(\pi^\dagger - \phi) + H.C.] \end{bmatrix} \tag{D.11}$$

$$h_V = \begin{bmatrix} V & 0 \\ 0 & -V \end{bmatrix} - \frac{Vv^2}{\gamma_1^2}\begin{bmatrix} (\pi^\dagger + \phi)(\pi + \phi) & 0 \\ 0 & -(\pi^\dagger - \phi)(\pi - \phi) \end{bmatrix} \tag{D.12}$$

To analyze the influence of h_w at low energies, if we can consider the no-field case first (Fig. D.1(a))

and only h_0 and the first term in h_w as it is also derived in Ref. [12]. The resulting energy $E = \pm\varepsilon_1$ is given by

$$\varepsilon_1^2 = (v_3 k)^2 - \xi \frac{v_3 k^3}{m} \cos(3\phi) + \left(\frac{k^2}{2m}\right)^2, \tag{D.13}$$

confining into very low energy regime we have $vk/\gamma_1 \ll 1$ and $v_3/v \ll 1$, $\mathbf{k} = (k_x, k_y)$. As without any external fields h_w is linear in momentum, its influence and the resulting triangular distortion of the iso-energetic contours become increasingly pronounced at lower energies and momenta. This distortion grows until a Lifshitz transition occurs at the characteristic energy

$$\varepsilon_L = \frac{\gamma_1}{4}\left(\frac{v_3}{v}\right)^2 \approx 1 \text{ meV}, \tag{D.14}$$

as also indicated in Fig. D.1(a). The white dashed line in the figure marks the 1 meV iso-energetic contour associated with this transition. For energies $|E| < \varepsilon_L$, the iso-energetic lines split into four distinct pockets: a central pocket and three "leg" pockets. The leg pockets are centred at momentum

$$k \approx \frac{\gamma_1 v_3}{v^2}$$

and angle ϕ_0, as illustrated in Fig. D.1.

When an external field is applied, the situation becomes more intricate due to the presence of terms that are first order in the magnetic field parameter ϕ. Nevertheless, for only displacement field; the contour plots in Fig. D.1(b) show that the transition energy shifts slightly from the zero-field value of 1 meV to approximately 0.97 meV with $V = 0.7$ meV. According to the $V\phi$-phase diagram in Fig. 6.2, this corresponds to a gapped and hence the insulating state, however, still maintaining the symmetric in-terms of the iso-energy contours and also insulating state.

To examine the LT in the metallic regime, we consider the case shown in Fig. D.1(c), with $V = 0.7$ meV and $B = 25$ T. Here, the iso-energetic contours become asymmetric, reflecting the breaking of the C_3 symmetry by the applied magnetic field. This symmetry breaking not only distorts the contours but also makes the LT anisotropic, with the critical energy varying along different crystallographic directions.

Appendix E

RENORMALIZATION OF FERMI VELOCITY WITH MOIRE PHYSICS IN TWISTED BILAYER GRAPHENE

E.1 Method to derive the renormalized fermi-velocity from the effective 8-band Hamiltonian

In the equation for h_j the dependence on θ is negligible for small rotation angles. One can easily replace (2.1) with

$$h_j = vk_\theta \begin{pmatrix} 0 & e^{i\theta a_j} \\ e^{-i\theta a_j} & 0 \end{pmatrix} \tag{E.1}$$

lightening the notation. One should recall that $|q_j| = k_\theta \ \forall \ j$ and θ_{q_j} can assume the three rotation angles listed above. The Hamiltonian (2.18), where $k_j = k + q_j$, can be written as the sum of

$$H_k = H_0 + H'_k \tag{E.2}$$

The first term is fixed by the condition $k = 0$, while the second represents the k-dependence. k in fact can be considered as a fluctuation of the wave vector close to the Dirac point. Solving the Hamiltonian at leading order in the excitation, H'_k can be replaced with

$$H'_k = v \begin{pmatrix} \sigma^* k & 0 & 0 & 0 \\ 0 & \sigma^* k & 0 & 0 \\ 0 & 0 & \sigma^* k & 0 \\ 0 & 0 & 0 & \sigma^* k \end{pmatrix}$$

To find the elements of the matrix (2.20), one should start proving the assumption that H_0 has null energy eigenvalues

$$\begin{cases} h_0\psi_0 + T_j\psi_j = 0 \\ T_j^\dagger\psi_0 + h_j\psi_j = 0 \end{cases} \longrightarrow \begin{cases} h_0\psi_0 + T_j\psi_j = 0 \\ \psi_j = -h_j^{-1}T_j^\dagger\psi_0 \end{cases} \tag{E.3}$$

From direct calculation one finds that

$$T_j h_j^{-1} T_j^\dagger$$

so multiplying on the left the second equation of (2.21) by T_j

$$T_j\psi_j = 0 \quad \longrightarrow \quad h_0\psi_0 = 0 \tag{E.4}$$

Finally, the modulo of Ψ is just

$$|\Psi|^2 = 1 + 6\alpha^2$$

where $\alpha = \frac{w}{v|q_j|}$.

One can compute now (2.24)

$$\begin{aligned} \frac{\langle\Psi^{(i)}|H_k^{(1)}|\Psi^{(j)}\rangle}{\langle\Psi^{(i)}|\Psi^{(j)}\rangle} &= \frac{1}{6\alpha^2+1}\left(\psi_0^{(i)\dagger}h_k\psi_0^{(j)} + \psi_0^{(i)\dagger}T_j h_j^{-1\dagger}h_k h_j^{-1}T_j^\dagger\psi_0^{(j)}\right) = \\ &= \frac{v}{6\alpha^2+1}\psi_0^{(i)\dagger}\left(\sigma^*\mathbf{k} - \sum_j T_j h_j^{-1\dagger}\sigma^*\mathbf{k}h_j^{-1}T_j^\dagger\right)\psi_0^{(j)} \end{aligned} \tag{E.5}$$

From equation (2.25), where $\epsilon_\theta = vk_\theta$, (2.26) becomes

$$\frac{\langle\Psi^{(i)}|H_k^{(1)}|\Psi^{(j)}\rangle}{\langle\Psi^{(i)}|\Psi^{(j)}\rangle} = \frac{v}{6\alpha^2+1}\psi_0^{(i)\dagger}\left(\sigma^*\mathbf{k} - \frac{1}{(vk_\theta)^2}\sum_j T_j\sigma^*\mathbf{k}T_j^\dagger\right)\psi_0^{(j)}$$

following the definition of h_j and the inter-layer tunneling matrices T_j the last term of the sum is just

$$\sum_j T_j\sigma^*\mathbf{k}T_j^\dagger = 3w^2\sigma^*\mathbf{k}$$

Finally the result for (2.26) is

$$\frac{\langle\Psi^{(i)}|H_k^{(1)}|\Psi^{(j)}\rangle}{\langle\Psi^{(i)}|\Psi^{(j)}\rangle} = v\left(\frac{1-3\alpha^2}{1+6\alpha^2}\right)\psi_0^{(i)\dagger}\sigma^*\mathbf{k}\psi_0^{(j)} = v^*\psi_0^{(i)\dagger}\sigma^*\mathbf{k}\psi_0^{(j)} \tag{E.6}$$

The Dirac velocity of this Hamiltonian is

$$v^* = v\frac{1-3\alpha^2}{1+6\alpha^2} \tag{E.7}$$

Equation (2.27) shows that the result obtained, has the same form of the continuum model Hamiltonian of a single layer of graphene $\epsilon_k^* = v^* k$.

The renormalized Fermi velocity v^* (Eq. E.9) exhibits distinct behavior compared to monolayer graphene. The reduction factor $\frac{1-3\alpha^2}{1+6\alpha^2} < 1$ implies v^* is always suppressed relative to the monolayer case. Here α encodes the twist angle θ via $\sin(\theta)$ in its denominator. Solving $v^* = 0$ in Eq. E.9 yields the first *magic angle* $\theta = 1.05°$, with additional magic angles emerging at smaller θ in numerical simulations.

This solution follows from

$$\alpha = \frac{w}{v_F \cdot 2k_D \sin(\theta/2)}, \tag{E.8}$$

where larger α^2 corresponds to smaller θ. Setting $\alpha^2 = \frac{1}{3}$ and substituting $t = 2.8\text{eV}$, $w = 0.11\text{eV}$, and expressions for v_F and k_D (magnitude of K/K') yields $\theta = 1.05°$. Figure shows subsequent magic angles with non-monotonic velocity trends. Its inset compares analytical (dashed) and numerical (solid) results, revealing only $\theta = 1.05°$ as a clear minimum where v^*/v vanishes monotonically—a feature absent at smaller angles.

$$v^* = v \cdot \frac{1-3\alpha^2}{1+6\alpha^2} \tag{E.9}$$

As it was mentioned before, ψ_0 is one of the two zero energy states, $\psi_0^{(1)}$ and $\psi_0^{(2)}$ of the isolated layer. Here the indices 1 and 2 are used to label the two degrees of freedom of the individual layer, namely A/B or electron/holes bands.

The two zero energy eigenstates of H_0, follow from (2.22) and the second equation of (2.21). From this result the elements of the Hamiltonian, up to leading order in $\mathbf{k}$, are

$$\frac{\langle\Psi^{(i)}|H_k|\Psi^{(j)}\rangle}{\langle\Psi^{(i)}|\Psi^{(j)}\rangle} = \frac{\langle\Psi^{(i)}|H_0|\Psi^{(j)}\rangle}{\langle\Psi^{(i)}|\Psi^{(j)}\rangle} + \frac{\langle\Psi^{(i)}|H_k^{(1)}|\Psi^{(j)}\rangle}{\langle\Psi^{(i)}|\Psi^{(j)}\rangle} \tag{E.10}$$

where Ψ are the eigenvalues of the unperturbed Hamiltonian H_0. From now on the upper indices (i) and (j) label the sub-lattice A and B.

The first term of equation (2.23) is null of course, so one is left with

$$\frac{\langle\Psi^{(i)}|H_k|\Psi^{(j)}\rangle}{\langle\Psi^{(i)}|\Psi^{(j)}\rangle} = \frac{\langle\Psi^{(i)}|H_k^{(1)}|\Psi^{(j)}\rangle}{\langle\Psi^{(i)}|\Psi^{(j)}\rangle} \tag{E.11}$$

The modulo of Ψ is

$$|\Psi|^2 = |\psi_0|^2 + |\psi_j|^2$$

in fact it can be set $|\psi_0|^2 = 1$, while ψ_j is such that

$$|\psi_j|^2 = \psi_j^\dagger\psi_j = \psi_0^\dagger T_j h_j^{-1\dagger} h_j^{-1} T_j^\dagger \psi_0$$

Using the fact that

$$h_j^{-1} = -\frac{1}{vk_\theta}\begin{pmatrix} 0 & e^{i\theta a_j} \\ e^{-i\theta a_j} & 0 \end{pmatrix} = -\frac{1}{\epsilon_\theta^2} h_j \tag{E.12}$$

it follows

$$h_j^{-1\dagger} h_j^{-1} = \frac{1}{v^2|q_j|^2}$$

leaving just

$$|\psi_j|^2 = \frac{1}{v^2|q_j|^2}\psi_0^\dagger T_j T_j^\dagger \psi_0$$

The product of the T_j terms, where the sum over j is superimposed, can be computed explicitly giving

$$\sum_j T_j T_j^\dagger = 6w^2\mathbf{1}$$

VITA

I, Amarnath Chakraborty, was born in Jhargram, a small town in West Bengal, India. I earned my Bachelor of Science degree in Physics from Midnapore College, Vidyasagar University, in 2016, followed by a Master of Science degree in Physics from the University of Hyderabad in 2018. After completing my M.Sc., I worked as an R&D assistant at the Jawaharlal Nehru Centre for Advanced Scientific Research (JNCASR) until 2019, while applying for doctoral positions in the United States. In 2019, I joined the University of Missouri–Columbia (UMC) to pursue doctoral studies in Theoretical Condensed Matter Physics under the mentorship of Prof. Giovanni Vignale.

My doctoral research focuses on understanding emergent quantum phenomena in two-dimensional materials, ranging from monolayer systems such as nonsymmorphic Dirac semimetals to multilayer systems including bilayer graphene. I have also explored twisted structures such as twisted bilayer and trilayer graphene. My work integrates analytical modeling with numerical simulations to investigate band topology and the evolution of band geometry under external fields. I have studied magneto-optical properties such as Hall conductivity, Faraday rotation, and also magnetic response parameters like susceptibility. These studies have resulted in peer-reviewed publications and collaborations with both theoretical and experimental groups. In addition, I taught several undergraduate laboratory courses to strengthen my teaching experience.

I have several completed publications and additional manuscripts in preparation for submission. **Doctoral Research, University of Missouri–Columbia (2019–2025)** Modeling and simulation of two-dimensional quantum materials for quantum technologies:

- **Twisted Bilayer Graphene under Crossed Fields (2024–Present)** Analyzed Berry curvature and orbital response near Dirac-to-parabolic transitions.
- **Trigonal Warping in Bilayer Graphene (2024–Present)** Demonstrated low-field metal–insulator transitions via skew-hopping effects, enabling routes to gate-tunable quantum devices.
- **Variational Quantum Eigensolver Internship (Summer 2025)** Developing error-mitigated

VQE and Sample-Based Quantum Diagonalization for the Fermi–Hubbard model on IBM heavy-hex hardware, benchmarking correlated phase metrics.

Key Publications

- Insulator-Metal Transition & Magnetic Crossover in Bilayer Graphene.
  Phys. Rev. B 111, 125130 (2025)
- Giant Faraday Rotation in Nonsymmorphic Dirac Semimetals.
  Phys. Rev. B 107, 245120 (2023)
- Photon Absorption in 2D Nonsymmorphic Dirac Semimetals.
  Phys. Rev. B 105, 085101 (2021)
- Observation of 2D Weyl Fermions in Bismuthene.
  Nat. Commun. 15, 6001 (2024)

Beyond research, I actively participated in science outreach through the Physics and Astronomy Graduate Student Association (PAGSA) and volunteered at local schools to promote STEM education. I completed an internship at the Quantum Innovation Center (QIC), a collaborative effort between UMC and IBM, where I modeled theoretical condensed matter systems using quantum circuits and mapped physical properties such as correlation functions in superconducting qubit devices.

I received multiple travel fellowships to attend international conferences and presented my work at APS March Meetings. I also contributed to collaborative projects involving large-scale simulations and device modeling in two-dimensional systems. At UMC, I engaged with the campus community, serving as president of the Cultural Association of India (CAI), a student-led organization representing the Indian student community.

I am expected to receive the Doctor of Philosophy degree in Physics from the University of Missouri–Columbia in August 2025.